Single-Walled Carbon Nanotube – Polymer Hybrids as Hole Transporting Layers for Organic Solar Cells



Joseph Sharkey

Pembroke College, University of Oxford

Thesis submitted in fulfilment of the requirements for the degree of Doctor of Philosophy at the University of Oxford

Trinity, 2018

Single-Walled Carbon Nanotubes – Polymer Hybrids as Hole Transporting Layers for Organic Solar Cells

Joseph Sharkey, Pembroke College, University of Oxford

Thesis submitted in fulfilment of the requirements for the degree of Doctor of Philosophy at the University of Oxford, Trinity Term, 2018

Abstract

In this thesis, new types of single-walled carbon nanotube (SWNT)-Polymer/single molecule nanostructures were prepared and successfully used as hole transporting layers in both conventional and inverted organic solar cells thereby pushing the carbon nanotube based organic solar cell efficiency close to 10%. The first part of the thesis focuses on investigating the binding of nanotubes to Spiro-OMeTAD. A novel dual-shell nanostructure was prepared by first wrapping SWNTs with a monolayer of semiconducting polymer (F8BT/P3HT) that forms Type-I / Type-II heterojunctions with the nanotube, and subsequently binding a large number of small molecules (Spiro-OMeTAD) onto the [Polymer-NT] nanohybrids. This strong interaction leads to a significant improvement in PL emission intensity which we associate with the debundling of the nanotube. In the second part of the thesis, the properties of a new polymer wrapped single walled carbon nanotubes (C8-SWNTs) were investigated and shown to successfully remove metallic impurities from different carbon nanotube starting materials. In addition, highly selective wrapping (~99.3%) of only one SWNT species (6,5) can be made possible by optimising the chain length of the polymer. PLE studies show that there is a ~71 fold reduction in the intensity of other SWNT species compared to the SWNT starting material. Finally, the third part of the thesis focusses on the fabrication of high efficiency organic solar cells (~9.4%) using highly semi-conducting Polymer-SWNT nanohybrids as hole transporting layers. A simple polymer exchange technique was used to produce ~99.5% pure semiconducting P3HT-SWNT nanohybrids. We used these nanoybrids as Hole Transporting Material (HTM) in the fabrication of the devices and were able to achieve high efficiencies with improved stability.

TO MY PARENTS AND WIFE

For their undying love, endless support

and constant encouragement.

Acknowledgements

I would like to sincerely thank my supervisor professor Robin Nicholas for all his invaluable advice, guidance, kindness and constant support throughout my DPhil.

I would also like to thank all the past and present DPhil students of Nicholas Group who helped me with my measurements, instrumentation issues and useful advice. In particular, I would like to thank Sam Stranks and Beate Dirks for the countless discussions, lab trainings and interpretation of some results presented here in this thesis.
I also want to thank Nathaniel, Guilio and Markus for making this journey much more fun and enjoyable.

This would not have been possible without the support of Clarendon Scholarship and I will forever be grateful for your generous support.

Last, but my no means least, my deepest thanks to my beloved parents, Angayarkanni and John Peter, who are the pillars of my life. Their constant encouragement and immense support made me who I am today. Finally, I would like to thank my wonderful wife, Keerthi Priya, who has sacrificed so much so that I can pursue my DPhil. These three are the most important people in my world and I dedicate this thesis to them.

Table of Contents

Chapters

1.Introduction....1

1.1Structure of the main chapters: 1

2.Single Walled Carbon Nanotubes 3

2.1 Origin of Carbon nanotubes....3

2.2 Carbon Nanotubes Structure 3

2.3 Density of States 7

2.4 Optical Transitions.... 10

2.5 Kataura Plot.... 13

2.6 Raman Features.... 14

2.7 Current SWNT Production Methods.... 16

2.7.1 CoMoCAT SWNTs 16

2.7.2 HiPCO SWNTs....18

2.8 Selective Growth.... 19

3.Theory of Solar Cells 24

3.1 Introduction.... 24

3.2 Overview of Organic Semiconductors.... 25

3.3 Basic Principle of OSCs.... 26

3.3.1 Light absorption and Exciton generation....26

3.3.2 Exciton dissociation and diffusion....28

3.3.3 Charge Carrier Transport....30

3.3.4 Charge extraction at electrodes....31

3.3.5 Summary....31

3.4 Solar Cell Architecture.... 32

3.4.1 Single layer solar cells 32

3.4.2 Bilayer solar cells....33

3.4.3 Bulk heterojunction Solar cells....34

3.4.4 Tandem solar cells 36

3.5 Characterization of OSCs.... 38

3.5.1 J-V characteristics....38

3.6 Origin and Recent Advancements of SWNT based OSCs 42

3.7 Summary 44
4.Materials and Methods 49
4.1 Materials 49
4.1.1 Single-wall carbon nanotubes 49
4.1.2 Polymers 51
4.1.3 Small Molecules 54
4.2 Experimental Methods 55
4.2.1 Preparation of SDBS-SWNT aqueous dispersions 55
4.2.2 Preparation of Polymer-SWNT nanohybrids 55
4.2.3 Solar Cell Fabrication 56
4.3 Characterization Methods 57
4.3.1 Absorption Spectroscopy 57
4.3.2 Photoluminescence Excitation (PLE) Spectroscopy 59
4.3.3 Atomic Force Microscopy (AFM) 61
4.3.4 Raman Spectroscopy and Scanning Electron Microscopy (SEM) 62
4.3.5 Solar cell characterization 63
5.Engineering New Ordered Nanostructures by Binding Single Molecules to Single-Walled Carbon Nanotubes 65
5.1 Introduction and Background 65
5.2 Sample Preparation 67
5.3 Absorption Spectroscopy 68
5.4 Photoluminescence Excitation Spectroscopy 71
5.5 Strain Calculation 74
5.6 Atomic Force Microscopy 76
5.7 Scanning Electron Microscopy Images 77
5.8 Applications 78
5.9 Summary 79
6.Preparation of Mono-Chiral SWNTs Using a Simple Solution Processing Technique. 83
6.1 Introduction and Background 83
6.2 Sample Preparation 85
6.3 Absorption Spectroscopy 87
6.3.1 Selectivity Vs Chain Length 89

6.3.2 Selectivity Vs Starting SWNT Materials 91
6.4.1 Selectivity Vs Chain Length 97
6.5 Raman Spectroscopy 100
6.6 Atomic Force Microscopy(AFM) 101
6.7 Scanning Electron Spectroscopy Images 102
6.8 Summary 103
7.Highly Pure Polymer-SWNT Nanohybrid Networks for Highly Efficient and Stable Organic Solar Cells. 107
7.1 Introduction and Background 107
7.2 Sample Preparation 108
7.3 Absorption Spectroscopy 110
7.4 Photoluminescence Excitation Spectroscopy 112
7.5 Raman Spectroscopy 114
7.6 Solar cell Fabrication 115
7.7 Solar cell Characterization 116
7.8 Stability of SWNT/Polymer based OSCs 118
7.9 Summary 120
8.Conclusion and Future Work: 123

Publications

J. Joseph Sharkey, Samuel D. Stranks, Jian Huang, Jack A. Alexander-Webber, and Robin J. Nicholas. Engineering Nanostructures by Binding Single Molecules to Single-Walled Carbon Nanotubes. ACS Nano, 2014, 8 (12), pp 12748–12754

J. Joseph Sharkey, Po-I Wang, Der-Jang Liaw and Robin J. Nicholas. Preparation of Mono-Chiral SWNTs using a simple solution processing technique. *Manuscript in preparation.*

J. Joseph Sharkey, Henry J. Snaith and Robin J. Nicholas. Highly pure Polymer-SWNT nanohybrid networks for highly efficient and stable Polymer solar cells. *Manuscript in preparation.*

Chapter 1

Introduction

Carbon is one of the most common elements on our planet. Its ability to combine with other atomic elements makes it one of the basic building blocks of the natural world and a key component of life itself. Carbon is found in all living plant and animal species, in many minerals and in the atmospheric gases. It is hard to imagine that any world as diverse and complex could exist in its absence. In this thesis, we will discuss more about their unique properties and their application in organic solar cells.

1.1 Structure of the main chapters:

The first part of the thesis focuses on investigating the binding of nanotubes to Spiro-OMeTAD, which is an amorphous conjugated small, organic material initially used as a hole transporting material in solid state dye-sensitized solar cells but more recently in perovskite-based solar cells, which have achieved power conversion efficiencies exceeding 20%. We fabricated a novel dual-shell nanostructure prepared by first wrapping SWNTs with a monolayer of semiconducting polymer (F8BT/P3HT) that forms Type-I / Type-II heterojunctions with the nanotube, and subsequently binding a large number of small molecules (Spiro-OMeTAD) onto the [Polymer-NT] nanohybrids. We use absorption and photoluminescence excitation (PLE) measurements to show that the small molecules induce a mechanical strain on the nanotubes. Further, atomic force (AFM) and scanning electron (SEM) microscopy were used to show that Spiro-OMeTAD binds strongly to Polymer-NT nanohybrids by forming very thick coatings and leading to additional debundling of the tubes.

The second part of the thesis focusses on study of our synthesised polymer (C8) which wraps around individual, smaller diameter, SWNTs. Moreover, the wrapping of the polymer seems to be chirality dependant. We were able to selectively wrap (6,5) tubes using a simple solution processing method and thereby producing SWNTs with identical electronic properties. We used absorption spectroscopy to estimate the purity of the SWNT. PLE studies show that there is a ~71 fold reduction in the intensity of other SWNT species compared to the SWNT starting material. We were also able to be successfully eliminating metallic tubes from both COMOCAT and HIPCO SWNT which was confirmed by the results from Raman spectroscopy.

Finally, the third part of the thesis focusses on the fabrication of high efficiency organic solar cells using highly semi-conducting Polymer-SWNT nanohybrids as hole transporting layers. We used a polymer exchange technique for the production of highly pure P3HT-SWNT nanohybrids which are ~ 99.5% semiconducting. We use absorption and PLE measurements to show the polymer exchange process and how we were able to remove almost all the metallic impurities from the nanohybrids. We used these nanoybrids as HTM in the fabrication of the devices and were able to achieve high efficiencies (~9.4%) and long-term stable devices with improved reproducibility.

Chapter 2

Single Walled Carbon Nanotubes

2.1 Origin of Carbon nanotubes

The very first evidence of the tubular nature of some nano-scale carbon allotropes is believed to have been published by Radushkevich and Lukyanovich in 1951 [1]. However, in 1991, when Iijima discovered carbon nanotubes (CNTs), a new branch of knowledge emerged – Nanoscience. Just two years later, in 1993, Ijima and Ichihashi published two Nature reports regarding Single Walled Carbon Nanotubes [2, 3]. The growth of CNTs however may date back over 400 years, as TEM image of steel in Damascus blades, known for their exceptional mechanical properties and sharp cutting edge, revealed MWNTs incorporated into the structures [4]. Billions of dollars were spent to unveil all the secrets of this ever-amazing material. As a matter of fact, recently, a fourth state of matter was discovered to be water trapped inside a carbon nanotube, which does not act as solid, liquid or gas.

2.2 Carbon Nanotubes Structure

As graphene is the basis of the microscopic structure of carbon nanotubes, they are often labelled in terms of the graphene lattice vectors. A SWNT is made by rolling up a single ribbon of graphene [5]. The direction it is rolled in relative to the lattice vectors (a_1 and a_2) and the width of the ribbon (circumference of the SWNT) are determined by the circumferential vector, C, which connects two crystallographically equivalent sites on the

graphene lattice which when rolled onto each other will join to make the tube, as described in figure 1.1. The structure of all SWNTs in this way may be completely specified simply by a pair of integers (n,m) which are contained in the circumferential vector,

$$C = na_1 + ma_2 \quad \textbf{[2.1]}$$

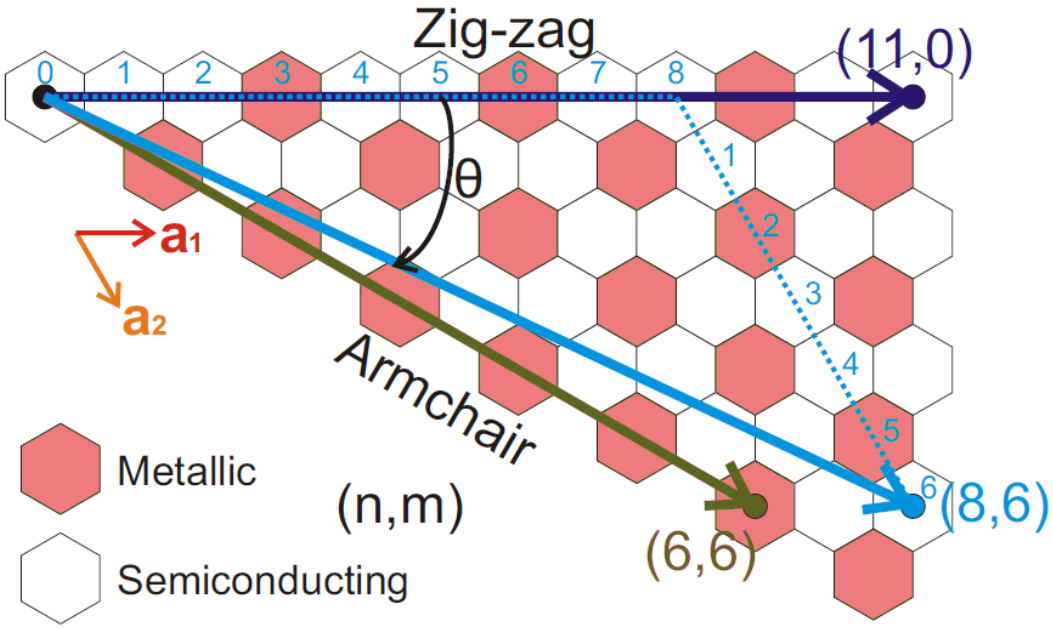

Figure 1.1: Chirality assignment and (n,m) notation of SWNTs. The chiral vector follows the circumference of the tube which for an (n,m) chirality tube is found by $C = na_1 + ma_2$ (blue dots). The axis along the tube direction is perpendicular to C. One third of CNT chiralities are metallic (red) with the condition n - m = 3l, with l integer.

The diameter d of the tube can be estimated trivially by the chiral vector as

$$d = |C|/\pi = \frac{\sqrt{3}a_0}{\pi}\sqrt{n^2 + nm + m^2} \quad \textbf{[2.2]}$$

There is also an associated chiral angle, θ, between C and a_1 (the zig-zag" direction), calculated using

$$\cos\theta = \frac{C \cdot a_1}{|C| \cdot |a_1|} = \frac{2n+m}{2\sqrt{n^2+nm+m^2}} \quad \textbf{[2.3]}$$

where $0 \leq \theta \leq 30^o$ due to the six-fold symmetry of the lattice. Two special cases arise from this notation: (n, 0) ($\theta = 0^o$), known as zig-zag tubes, exhibiting a zig-zag pattern along the circumference, and (n, n) ($\theta = 30^o$), known as armchair tubes which look like armchairs along the circumference (Fig. 1.12). These special cases are achiral, all other ($n,m \neq n \neq 0$) SWNTs are chiral (Fig. 1.13). The structure of a tube also determines the unit cell and the number of atoms within it. For this, we can define the smallest lattice vector $T = t_1a_1+t_2a_2$ which is perpendicular to C and defines the translational period $|T| = t$ given by

$$t_1 = \frac{2m+n}{N_R}, t_2 = -\frac{2n+m}{N_R}, \ |T| = t = 3a_0\frac{\sqrt{n^2+nm+m^2}}{N_R} \quad \textbf{[2.4]}$$

where N_R is the greatest common divisor of (2m+n) and (2n+m). Therefore, the unit cell of a SWNT is a cylinder of diameter d with a height t, where the number of carbon atoms per unit cell N_C, can be defined in terms of n and m where

The number of hexagons per unit cell is $Q = N_C/2$

$$N_C = \frac{4(n^2+nm+m^2)}{N_R} \quad \textbf{[2.5]}$$

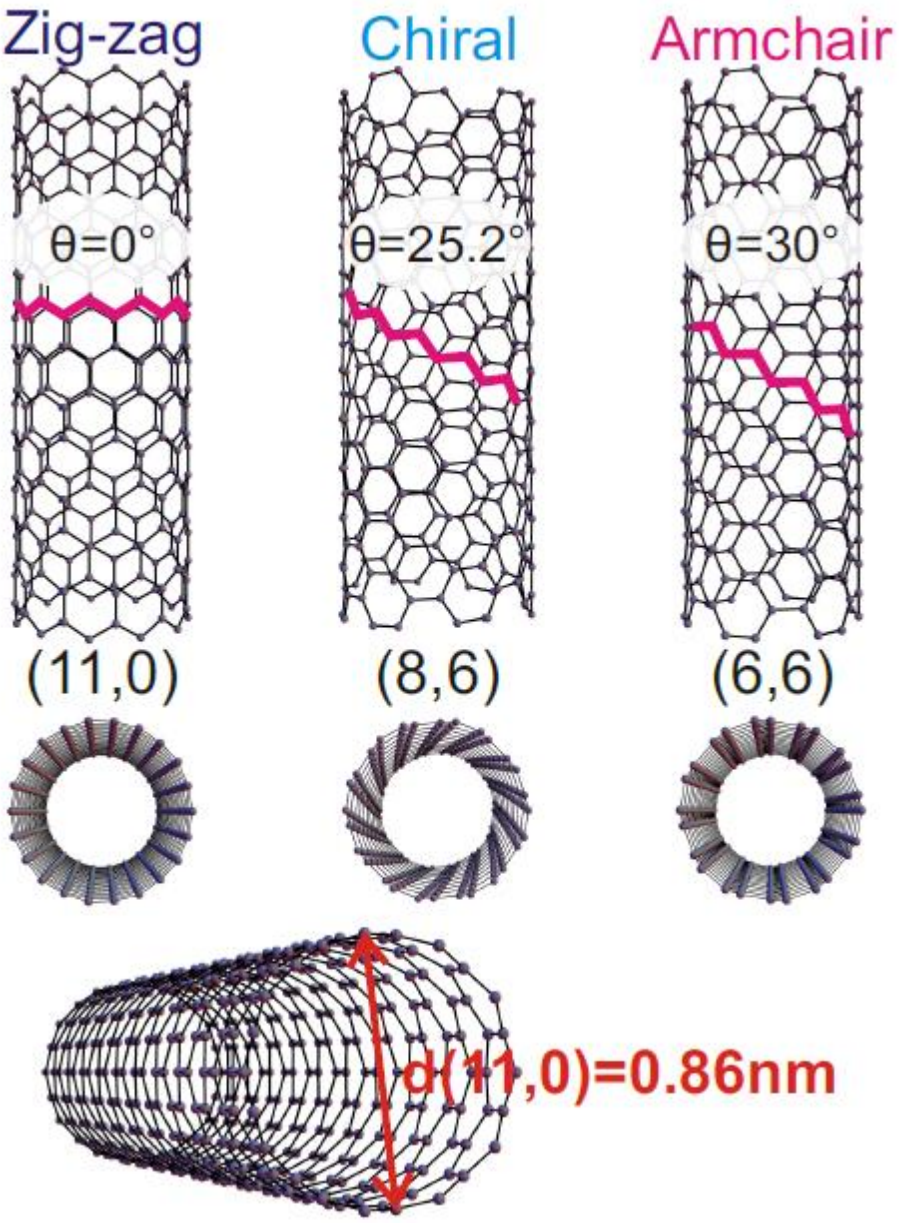

Figure 1.2: Top: The honeycomb structure of graphene folded with three different chiralities, representative of zig-zag, chiral, or armchair type CNTs. For clarity, the direction of the folding is shown by following a consecutive line of A-B-A-B atoms (magenta). Bottom: The calculated diameter of an (11,0) chirality CNT.

2.3 Density of States

The density of states (DOS) is the number of sites available ΔN for electrons to occupy in a given energy interval ΔE. The shape of DOS strongly depends on the dimension of the system in question. For a single one-dimensional system like carbon nanotubes, the general DOS was derived by Mintmire and White [6] and is given by,

$$n(E) = \frac{2}{Q|k_\parallel|}\sum_j d\,k_\parallel \delta(k_\parallel - k_l)\left|\frac{\partial E^{\pm}(k_\perp,k_\parallel)}{\partial k_\parallel}\right|^{-1} \quad \textbf{[2.6]}$$

Where k_j are the roots of E – E(k_j) =0 and $Q|k_\parallel| = 4\pi^2 d/\sqrt{3}a_0^2$. To calculate (E) at a vector **k** near the Fermi level and hence near the K point **K**, it is useful to expand the graphene energy bands in Eq. $E_{2D}^{\pm}(k_x,k_y) = \pm\gamma_0\sqrt{1+4cos\frac{\sqrt{3}k_x a_0}{2}cos\frac{k_y a_0}{2}+4cos^2\frac{k_y a_0}{2}}$, to first order, to give the linear dispersion relation:

$$E^{\pm}(\boldsymbol{k}) \approx \pm\frac{\sqrt{3}}{2}a_0\gamma_0|\boldsymbol{k}-\boldsymbol{K}| \quad \textbf{[2.7]}$$

The distance to the point **k** is given by $|\boldsymbol{k}-\boldsymbol{K}| = \sqrt{\Delta k_\parallel^2 + \Delta k_\perp^2}$. The quantity $\Delta k_\parallel$ is the component parallel to $\boldsymbol{k}_\parallel$ and takes continuous values. By contrast, the quantity $\Delta k_\perp$takes quantized values along the $\boldsymbol{k}_\perp$ direction given by the projection of $(\boldsymbol{k}-\boldsymbol{K})$ onto $\boldsymbol{k}_\perp$:

$$\Delta k_\perp = \left|(\boldsymbol{k}-\boldsymbol{K})\cdot\frac{\boldsymbol{k}_\perp}{|k_\perp|}\right| = \frac{2}{3d}|3i-q| \quad \textbf{[2.8]}$$

where q is defined in equation $(n-m) = 3p + q, q = \begin{cases} 0 & metallic\ tubes \\ \pm 1 & semiconducting\ tubes \end{cases}$ and i takes integer values. The derivative term is given by

$$\left|\frac{\partial E^{\pm}(k_{\perp},k_{\parallel})}{\partial k_{\parallel}}\right|^{-1} = \left|\frac{\sqrt{3}}{2}a_0\gamma_0\frac{\partial\sqrt{\Delta k_{\parallel}^2+\Delta k_{\perp}^2}}{\partial k_{\parallel}}\right|^{-1} = \left(\frac{2}{\sqrt{3}a_0\gamma_0}\right)\frac{|E^{\pm}|}{\sqrt{(E^{\pm})^2 - E_i^2}} \qquad \textbf{[2.9]}$$

with

$$E_i\frac{\sqrt{3}}{2}a_0\gamma_0\Delta k_{\perp} = |3i-q|\frac{a_0\gamma_0}{\sqrt{3}d} \qquad \textbf{[2.10]}$$

Finally, inserting these expressions into Eq. 2.6 and integrating gives density of states as:

$$n(E) = \frac{4a_0}{\pi^2 d\gamma_0}\sum_{i=-\infty}^{\infty} g(E,E_i), \quad g(E,E_i) = \begin{cases} \frac{|E|}{\sqrt{E^2-E_i^2}} & |E| > |E_i| \\ 0 & |E| > |E_i| \end{cases} \qquad \textbf{[2.11]}$$

The singularities in the DOS at energies E_i are known as the **van Hove singularities** [7].

These values are given by $E_i = ia_0\gamma_0/\sqrt{3}d$ where i = 0, 3, 6, . . . for metallic tubes and i = 1, 2, 4, 5, 7, 8 . . . for semiconducting tubes and, in this Mintmire and White approximation [6], depend only on the tube diameter d. Metallic nanotubes therefore have no bandgap but semiconducting tubes have a finite bandgap equal to:

$$E_{11}^S = 2E_{i=1} = 2a_0\gamma_0/\sqrt{3}d \qquad \textbf{[2.12]}$$

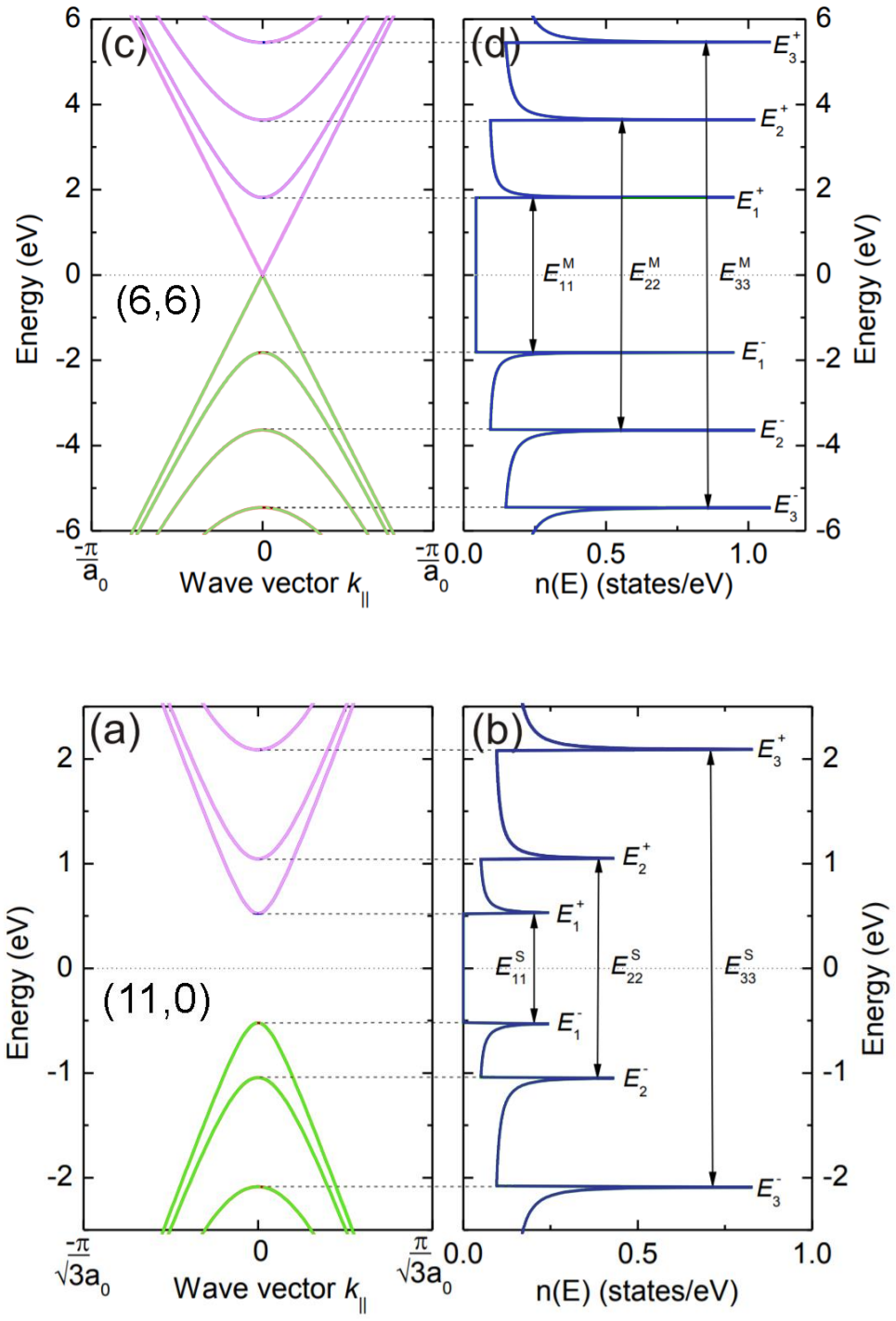

Figure 1.3: Density of states for a (6, 6) nanotube (above) and a (11, 0) nanotube (below) derived from the zone-folding approximation. The density of states are shown next to the linearly approximated bandstructure according to the tight-binding model of graphene. Band energies and interband transitions are indicated. [8]

In figure 1.3, the density of states for the two cases of a metallic (6, 6) and a semiconducting (11, 0) are shown next to the linearly approximated band structure derived from the tight-binding approximation of graphene. The relevant energy levels for the metallic nanotube E_i^m and the semiconducting nanotube E_i^S as well as the intraband transitions E_{ii} are labeled.

2.4 Optical Transitions

Any transition must obey conservation of energy and momentum. Conservation of linear momentum ($\Delta k = 0$) means that only vertical transitions are allowed on plots such as Fig. 1.4 (a) [9]. The selection rules for conservation of angular momentum depend on the orientation of the electric field E of the light. When a nanotube aligned along T absorbs or emits a photon with angular momentum of ±1, the selection rules are:

$$\Delta i = 0 \qquad \text{for } \mathbf{E} \parallel \mathbf{T} \qquad \textbf{[2.13]}$$

$$\Delta i = \pm 1 \qquad \text{for } \mathbf{E} \perp \mathbf{T} \qquad \textbf{[2.14]}$$

where i is the same integer quantum number used in Eq. 2.10 [9]. Therefore, the transitions E_{11}, E_{22}, E_{33} and higher orders are allowed for light polarised along the nanotube axis and transitions such as E_{21} are allowed for light polarised perpendicular to the tube axis; a selection of these transitions are shown in Fig. 1.4 (a). The perpendicular transitions are on average 5 times weaker than those corresponding to parallel excitations due to screening induced by the depolarisation (antenna) effect [7, 10].

By Fermi's Golden Rule, the intensities of the absorption transitions E_{ij} depend on the matrix element given by the overlap between the wavefunctions of the initial valence band state (at energy E_i^-) and the final conduction band state (at energy E_j^+) under the

action of a perturbed Hamiltonian [13]. In an E_{ij} absorption transition, an electron is promoted from the valence band E_i^- to the conduction band E_j^+, leaving a hole in the E_i^- band. If the excitation involves states higher than $E_1^{\pm}$, rapid relaxation of the electron and hole occurs by phonon emission to the E_1^+ and E_1^- levels, respectively [14, 15]. The electron and hole subsequently recombine and a photon of energy E_{11} is emitted, i.e. photoluminescence. This chain of processes is often exploited experimentally to excite the nanotube E_{22} transitions and monitor the E_{11} emission using a technique called photoluminescence excitation (PLE) spectroscopy, which was utilised in this thesis. Due to the large DOS at the van Hove singularities, carbon nanotubes have strong, narrow absorption and photoluminescence features. Recent experimental work has shown that the absorption cross-section of the E_{11} transition is $\sim 1.7\times10^{-17}$ cm^2 per carbon atom for (6,5) nanotubes [16]. The sets of transitions (E_{11}, E_{22}) provide a unique fingerprint of each (n, m) nanotube and PLE spectroscopy provides a powerful optical characterization tool.

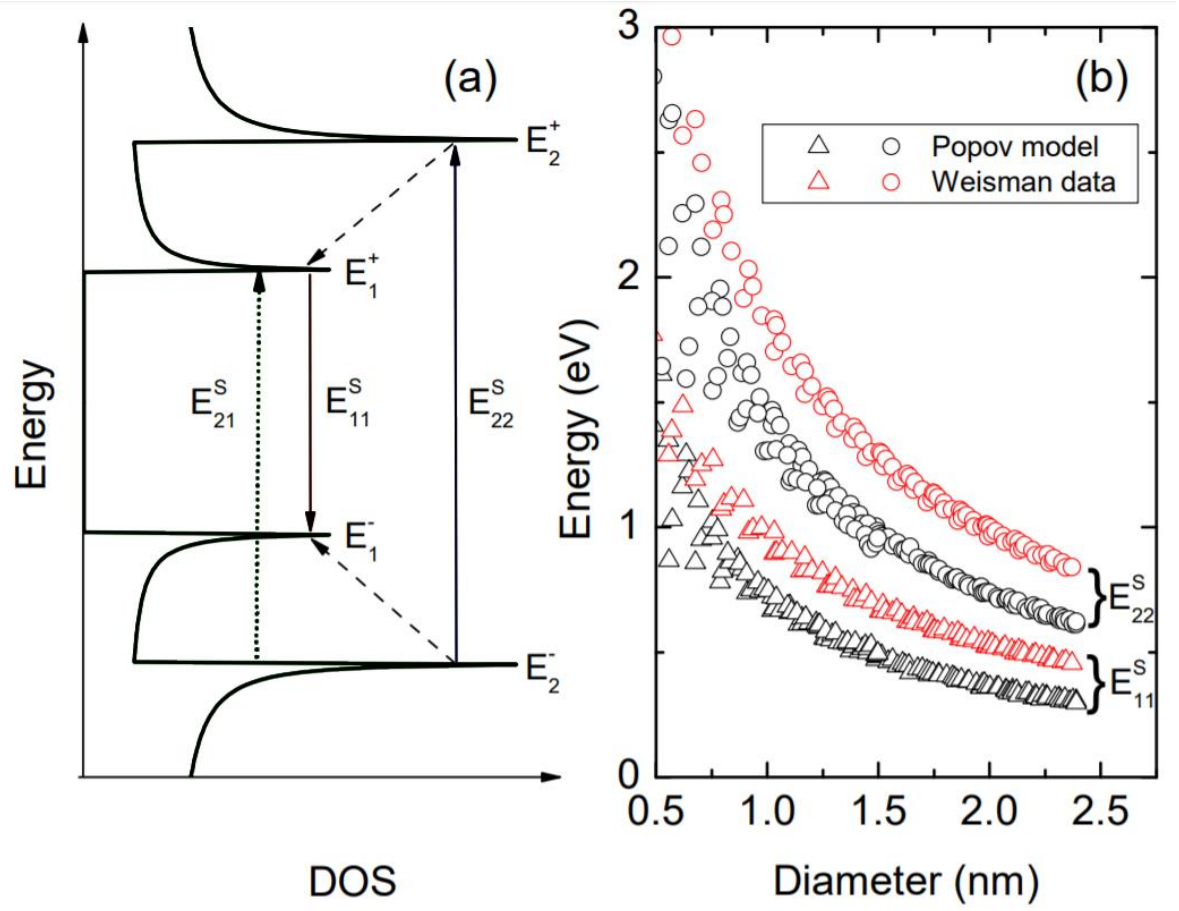

Figure 1.4: (a) Density of states for a semiconducting nanotube showing some of the optical transitions. Absorption of light corresponding to E_{22} promotes an electron from the valence E band to the conduction E_2^+ band and leaves a hole in E_2^-. Rapid relaxation of the electron and hole occurs to the E_1^+ and E_1^- bands, respectively, (dashed black lines) and the electron subsequently recombines with the hole, emitting a photon of energy E_{11}. (b) Kataura plot using the extended TB model developed by Popov et al. [11] (black symbols), along with the empirical data obtained by Weisman and Bachilo [12] (red symbols).

2.5 Kataura Plot

The simple TB theory predicts that the nanotube transitions E_{ii} are inversely proportional to the tube diameter d (Eq. 2.12) and a plot of the two quantities was first presented by Kataura et al. in 1999 [17]. However, the differences between these values and the experimentally derived values are large, particularly for small chiral angles. To improve the approximation, an extended TB model was developed by Popov et al. [11], which included the effects of trigonal warping and rehybridisation arising from curvature. A 'Kataura plot' using the values from Popov et al. is shown in Fig. 1.4 (b) and it provides a very good model for the unperturbed band edge states. An empirical model was proposed by Bachilo et al. [18] in 2002 from photoluminescence data and was subsequently refined by Weisman and Bachilo in 2003 [12]. The results are also presented in Fig. 1.4 (b) and these data allow easy identification of nanotubes in a distribution using optical experiments. The plot shows clear discrepancies between the Popov model and the empirical values. The latter values are systematically blue-shifted with respect to the former and this deviation is known as the 'blue-shift problem'. Furthermore, both the simple (Eq. 2.10) and the Popov extended TB models predict the energy ratio $E_{22}/E_{11} = 2$ in the large-diameter limit in which trigonal warping and curvature effects are negligible. However, the ratio of the empirical Weisman values converge to $E_{22}/E_{11} \sim 1.75$ for large diameters; this discrepancy is called the 'ratio problem' [18]. These anomalies were able to be reconciled by including the effects of excitons and many-body interactions in nanotubes.

2.6 Raman Features

Raman scattering is an inelastic photon scattering process involving the absorption or emission of phonons [7]. In a non-resonant scattering process, the incident photon excites an electron from the valence band to a virtual state close to a real state in the conduction band. In an elastic Rayleigh scattering process, the electron decays to the ground state with emission of a photon at the incident photon energy. A Raman scattering process is inelastic and the final and initial states differ, with an accompanying absorption (anti-Stokes scattering) or emission (Stokes scattering) of one or more phonons. The process requires conservation of energy and momentum and the resulting scattered photon will have a higher or lower energy relative to the incident photon (i.e. a Raman shift). Therefore, the scattering spectrum will consist of peaks spaced at multiples of $\pm\sim\omega$ about the excitation peak, where ω is the angular frequency of the emitted or absorbed phonon. The transition intensities are significantly enhanced if the scattered or incident photons match an allowed optical transition and this is referred to as a resonant Raman process. In conjunction with absorption and photoluminescence features, the resulting Raman features allow nanotube optical spectra to be fully characterized and related to tube structure. Raman spectra of SWNT material at an excitation wavelength of 633nm can be seen in Fig 1.5. The spectra is divided into 4 main zones: the low frequency region from 140-500cm^{-1}, the intermediate zone from 500-1000cm^{-1}, the high frequency zone from 1000-2000cm^{-1} and second order scattering zone from 2000-3000cm^{-1}. The first 3 zones are the characteristics of SWNTs. The radial breathing mode (RBM) is especially unique to carbon nanotubes and involves all carbon atoms moving in phase in the radial direction, creating a breathing-like vibration of the entire tube. It has the property that the RBM mode frequency

is inversely proportional to the tube diameter [7] and is found at small Raman shifts (100–500 cm^{-1}). Metallic tubes for which |n-m|=3q, where q is an integer, are separated in diameter to a greater extent compared to semiconducting tubes. Hence, probing the region between 457 and 633nm where the first interband transitions of the metallic nanotubes are dominant should produce only those discrete mode frequencies. The G-Band in SWNTs is composed of two strong peaks (G^+ and G^-) at ~1600 cm^{-1} related to the circumferential (TO) and axial (LO) atomic vibrations and the splitting of the two peaks depends on the tube-wall curvature and hence tube diameter. The D-Band (~1350 cm^{-1}) arises from a second-order process related either to the presence of defects in the tube walls or to amorphous-carbon material in the sample. It originates from symmetry breaking on the hexagonal sp^2-bonding lattices for graphite and nanotubes. Finally, the G' Band is at a frequency of twice the D-Band and arises from a two-phonon process [19].

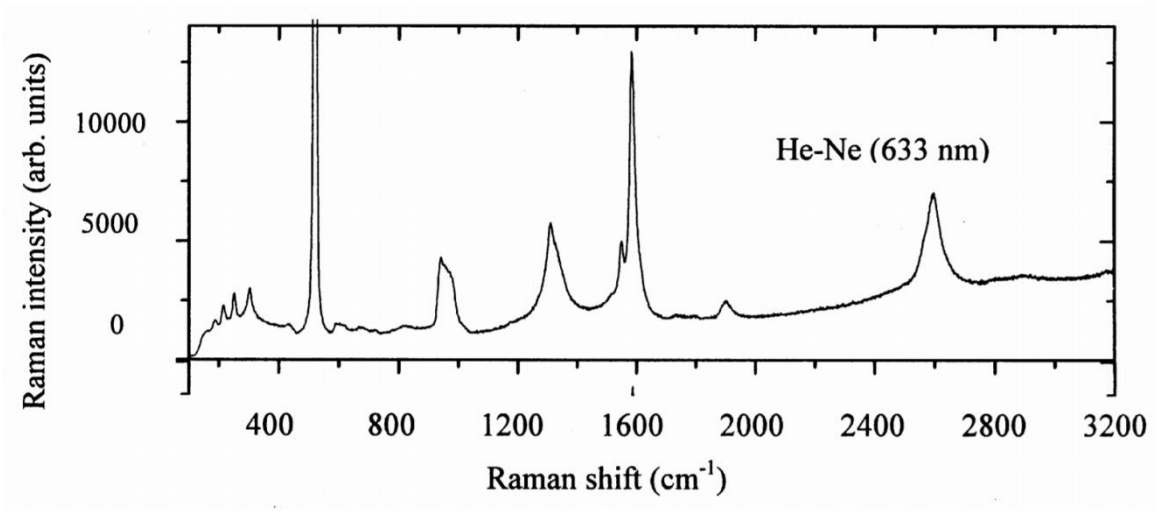

Fig 1.5: Raman spectra of SWNT material at an excitation wavelength of 633nm. [Reproduced from [39]. Copyright Bull. Mater Sci (2007)]

2.7 Current SWNT Production Methods

This section introduces several of the most widely used samples of SWNTs and the production methods involved. It introduces the latest techniques designed to significantly reduce the width of the chiral distribution of the as-grown nanotubes in order to achieve a more homogenous material, with the bottom-up approach to controlling the chirality of a nanotube sample.

2.7.1 CoMoCAT SWNTs

CoMoCAT is a SWNT sample originating from the decomposition of carbon monoxide in the presence of the bi-metallic cobalt and molybdenum catalyst, first reported by Resasco *et al* in 2000 [20]. When used individually, the two transition metals are ineffective: cobalt is not selective as the sole catalyst in the production of SWNTs and molybdenum is inactive in the temperature range used (600-800°C). When combined with a low Co:Mo ratio however, with a controlled CO concentration and temperature, they were able to produce high quality nanotube powders with high SWNT selectivity over multi-walled structures. The cobalt oxide is reduced to the metallic form and the molybdenum becomes a carbide, prompting the growth of SWNTs [21]. Having shown the ability to grow SWCNTs preferentially via this method of controlled vapour deposition (CVD), the group went further to show that within the SWNTs being produced, there was a high selectivity for specific chiralities such as the (6,5) and (7,6) SWNTs. The bi-metallic catalyst exists as highly dispersed MoO3 covered in a cobalt molybdate layer, which is disrupted by Mo carbide formation upon exposure to CO at 750°C and 5 atm, producing

small Co metallic clusters. The CO disproportionates onto these metallic clusters to grow the SWNT product via the Boudouard reaction [22]:

$$CO + CO \Rightarrow CO_2 + C(SWNTs) \qquad \textbf{[2.15]}$$

By operating at a relatively low temperature, the size of the metallic Co clusters is kept small and the resultant SWNT diameter range is narrowed. The diameter of CoMoCAT SWNT ranges between 0.7-1.1nm. These nanotubes are longer than 1 micrometre with (7,5) species being the most dominating chirality. The entire distribution of the CoMoCAT NTs can be seen in fig 1.5. [32]

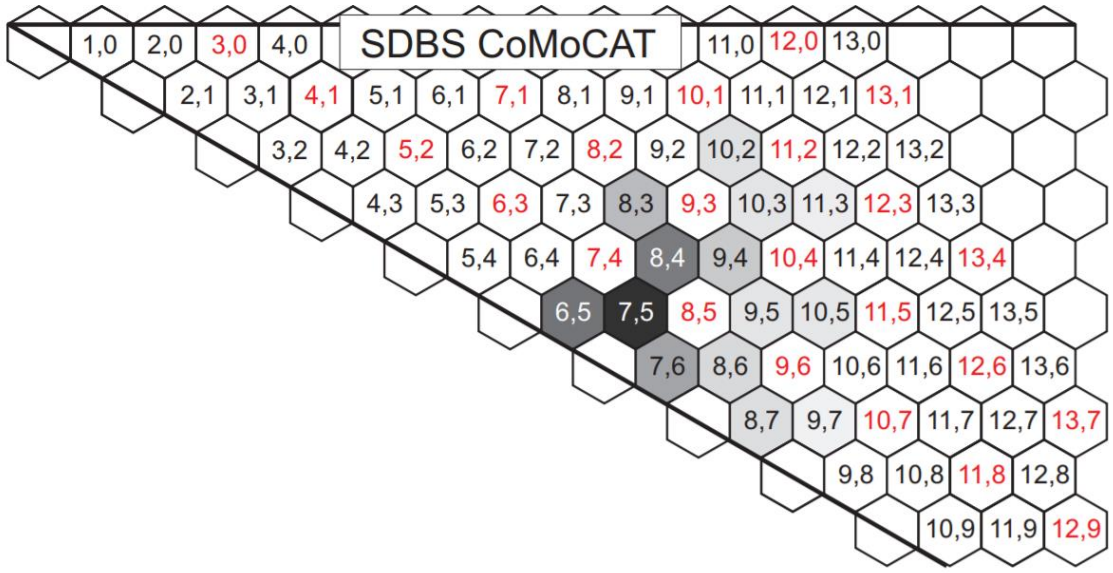

Fig 1.6: The hexagons correspond to the relevant (*n*,*m*) metallic (red indices) and semiconducting (black indices) CoMoCAT NT species, with the darker fill shading representing higher PL intensity. (Reproduced with permission from [32]. Copyright 2007 Nature Nanotechnology).

2.7.2 HiPCO SWNTs

Another commercially produced material is HiPCO SWNTs. Like the CoMoCAT manufacture, it is a CVD method that uses a catalyst to seed SWNT growth from a carbon feedstock, first reported by the Smalley Group at Rice University in 1999 [23]. The feedstock used is again CO, however the catalyst is gaseous iron pentacarbonyl $Fe(CO)_5$. At high temperature and high CO pressure, the $Fe(CO)_5$ thermally decomposes to form small metallic iron clusters of Fe(CO)n (n = 1; 2; 3; 4) that provide the catalytic sites for the Boudouard reaction to occur [24]. The product from HiPCO is different to CoMoCAT in terms of the electronic structure with a wider diameter ranging from 0.7nm – 1.4nm. HiPCO NTs consist of more metallic tubes (>30%) compared to CoMoCAT tubes (<20%). The entire distribution of HiPCO NTs can be seen in fig 1.6. [32]

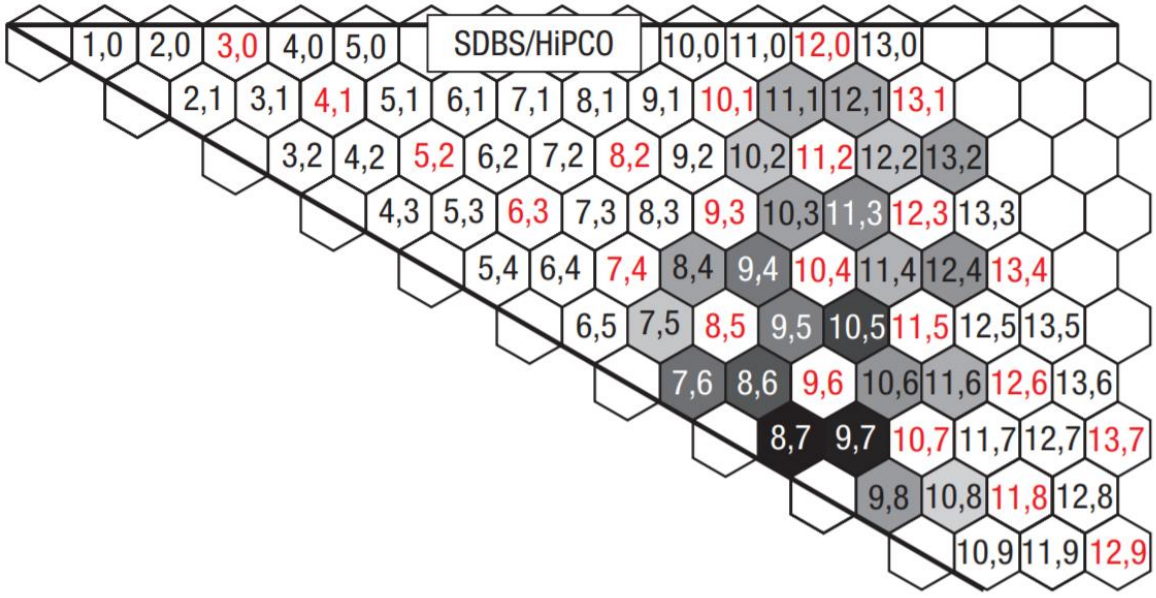

Fig 1.7: The hexagons correspond to the relevant (*n*,*m*) metallic (red indices) and semiconducting (black indices) HiPCO NT species, with the darker fill shading representing higher PL intensity. (Reproduced with permission from [32]. Copyright 2007 Nature Nanotechnology).

2.8 Selective Growth

The diameter of SWNTs depends strongly on the size of the catalyst used. Hence, preparation of uniform catalyst size is the main factor for controlling the diameter of the nanotube. Previously, lots of effort was put to control the catalyst size. For example, Dai and Pfefferle got uniform diameter SWNTs using polyamidoamine dendrimer [33] or MCM-41 [34] as catalyst carriers, respectively. Hyon *et al.* reported one way to control the diameter of the SWNTs by Langmuir-Blodgett film [35]. Kobayashi *et al* reported the average size of the catalyst and the corresponding diameters of SWNTs of 1.7 and 1nm, respectively (Ratio 1:7). [36] Zhang *et al* reported that diameter ratio between the catalyst and bamboo-shaped SWNTs were 1.25 [37]. Although the CoMoCAT selective growth mechanism has been successful in the mass production of a narrowed chiral distribution, Jorio *et al* showed that at least 25 chiralities were observed in the Raman spectra with a quasi-continuous laser excitation [25]. Other methods have also observed substantial deviation from the idealised 1:2 metallic-SWNT:semiconducting-SWNT ratio (m-SWNT:sc-SWNT), such as Li *et al* who showed PECVD could grow ~90 % sc-SWCNTs using a ferritin catalytic substrate and showed that laser ablation could produce ~70 % m-SWCNT samples [26]. Yang *et al* showed an enhancement of single chiral growth with a sample consisting of 92 % (12,6) m-SWNTs, by using CVD of ethanol and careful preparation of an alloy of W_6Co_7 nanoclusters to catalyse the growth. The group also showed the possibility of selective growth of the (16,0) and the (14,4) SWNTs [27]. However, these controlled growths still do not produce samples with containing only a single chiral angle. One reason that this ideal growth may be unobtainable can be seen in the diameter difference between the (10,10) m-SWNT and the (11,9) sc-SWNT. The latter

SWCNT is wider by only 0.23nm, making catalyst size control for CVD growth extremely difficult.

In 2006, Smalley *et al* demonstrated continued growth of carbon nanotubes using a HiPCO sample [28]. By cutting up the tubes using high-temperature, defect inducing fluorination and acid washing using H_2SO_4/H_2O_2 to chemically cut and oxidize the SWCNTs ends, the team were able to reattach the iron catalyst to the SWNT ends and continue the growth of a 200 nm long tube up to 6-7 μm. This work was continued by Yao *et al* in 2009 but without the use of a catalytic metallic particle [29]. By growing ultralong SWNTs (> 50 μm) on a quartz substrate, the nanotubes were segmented using electron beam lithography and subjected to a CH_4/C_2H_4 carbon feedstock. They demonstrated the continued growth of the segmented SWNTs from the open end and showed that the new sections had the same chirality as the parent seed, with a 40 % cloning efficiency. The formation of supramolecular complex between DNA and carbon nanotubes has drawn much attention in the past years as these nanohybrids take advantage of their unique properties of the CNTs and the remarkable recognition capabilities of DNA. DNA-CNT nanohybrids are stable entities in aqueous solutions due to the strong non-covalent interaction between DNA and CNTs. Compared to polymers, DNA offers advantage of length and sequence, high dispersion efficiency (4mg/ml) and well developed chemistries for further functionalization of DNA-CNT nanohybrids through covalent or non-covalent functionalization [38]. Another approach uses single-stranded DNA where the DNA wraps helically around the NTs by π-π stacking between the nucleobases of the DNA and the π electrons of the SWNT side walls. In 2012, Liu *et al* took a step towards scalability of continued growth by using selective DNA-wrapping to obtain 90 % single chiral SWCNTs dispersions [30, 31]. They demonstrated that by using vapour phase epitaxy with ethanol or

methane as the feedstock, they could increase the selectivity of (7,6), (6,5) and (7,7) chiralities. Even though the selectivity of SWNT from all these methods are quite good, to our knowledge, no one has achieved nearly pure monochiral SWNTs.

Reference

[1]. L. Radushkevich & Z. Lukyanovich, Zurn. Fisic. Chim., 26 88 (1952).

[2]. S.A. Empedocles and M.G. Bawendi, Science 278, 2114 (1997).

[3]. C. Georgi, N. Hartmann, T. Gokus, A.A. Green, M.C. Hersam, and A. Hartschuh, Chem. Phys. Chem. 9, 1460 (2008).

[4]. P. Finnie and J. Lefebvre, ACS Nano 6, 1702 (2012).

[5]. J.-C. Charlier & S. Roche, Reviews of Modern Physics, 79 (2) 677 (2007).

[6]. J. W. Mintmire & C. T. White, Phys. Rev. Lett., 81 2506 (1998).

[7]. S. Reich, C. Thomsen, & J. Maultzsch, Carbon Nanotubes – Basic Concepts and Physical Properties, Wiley-VCH, first edn. (2004).

[8]. K. B. Wolfstirn, J. Phys. Chem. Solids, 16 279 (1960).

[9]. I. Bozovic, N. Bozovic, & M. Damnjanovic, Phys. Rev. B, 62 6971 (2000).

[10]. H. Ajiki & T. Ando, Physica B, 201 349 (1994).

[11]. V. N. Popov, New J. Phys., 6 17 (2004).

[12]. R. B. Weisman & S. M. Bachilo, Nano Lett., 3 1235 (2003).

[13]. J. Jiang, R. Saito, A. Gruneis, G. Dresselhaus, & M. S. Dresselhaus, Carbon, 42 3169 (2004).

[14]. J. S. Lauret, C. Voisin, G. Cassabois, C. Delalande, P. Roussignol et al., Phys. Rev. Lett., 90 057404 (2003).

[15]. C. Manzoni, A. Gambetta, E. Menna, M. Meneghetti, G. Lanzani et al., Phys. Rev. Lett., 94 207401 (2005).

[16]. F. Schoppler, C. Mann, T. C. Hain, F. M. Neubauer, G. Privitera et al., J. Phys. Chem. C, 115 14682 (2011).

[17]. H. Kataura, Y. Kumazawa, Y. Maniwa, I. Umezu, S. Suzuki et al., Synth. Met., 103 2555 (1999).

[18]. S. M. Bachilo, M. S. Strano, C. Kittrell, R. H. Hauge, R. E. Smalley et al., Science, 298 2361 (2002).

[19]. A. Jorio, G. Dresselhaus, & M. S. Dresselhaus (editors), Carbon Nanotubes, vol. 111 of Topics Appl. Physics, Springer (2008).

[20]. Kitiyanan B, Alvarez W, Harwell J, Resasco D Chem Phys Lett. 317(3) 497-503 (2000).

[21]. Alvarez W, Kitiyanan B, Borgna A, Resasco D. Carbon. 39 (4) 547-558 (2001).

[22]. Zhang Q. Carbon nanotubes and their applications. CRC Press (2012).

[23]. Nikolaev P, Bronikowski MJ, Bradley RK, Rohmund F, Colbert DT, Smith K, et al. Gas-phase catalytic growth of single-walled carbon nanotubes from carbon monoxide. Chem Phys Lett. 313(1) 91–97 (1999).

[24]. Bronikowski MJ, Willis PA, Colbert DT, Smith K, Smalley RE. Gas-phase production of carbon single-walled nanotubes from carbon monoxide via the HiPco process: A parametric study. J Vac Sci Technol, A. 19(4) 1800-1805 (2001).

[25]. Jorio A, Santos A, Ribeiro H, Fantini C, Souza M, Vieira J, et al. Quantifying carbon-nanotube species with resonance Raman scattering. Phys Rev B: Condens Matter.72 (7) (2005).

[26]. Li Y, Mann D, Rolandi M, Kim W, Ural A, Hung S, *et al.* Nano Lett. 4(2) 317-321 (2004).

[27]. Yang F, Wang X, Zhang D, Yang J, Luo D, Xu Z, *et al.* Nature. 510(7506) 522-524 (2014).

[28]. Smalley RE, Li Y, Moore VC, Price BK, Colorado R, Schmidt HK, *et al.* J Am Chem Soc. 128(49) 15824-15829 (2006).

[29]. Yao Y, Feng C, Zhang J, Liu Z. Nano Lett. 9(4) 1673-1677 (2009).

[30]. Tu X, Manohar S, Jagota A, Zheng M. Nature. 460(7252) 250-253 (2009).

[31]. Liu J, Wang C, Tu X, Liu B, Chen L, Zheng M, *et al.* Nat Commun. 3 1199 (2012).

[32]. Adrian Nish, Jeong-Yuan Hwang1, James Doig & Robin J. Nicholas. Nature Nanotechnology 2, 640 - 646 (2007).

[33]. H.J Dai *et al.* J. Phys. Chem. B 106(48), 12361-12365 (2002).

[34]. L.Pfefferle *et al.* J. Phys. Chem. B 180(2) 503-307 (2004).

[35]. T. Hyeon *et al.* J. Phys. Chem. B 108(24), 8091-8095 (2004).

[36]. Y. Kobayashi *et al.* Thin Films, 464-465 (2004).

[37]. X.X. Zhang *et al.* Chem Phys Lett, 333(6) (2001).

[38]. Zheng *et al.* Nature Materials 2, 338-342 (2003).

[39]. Harsh et al. Bull Mater. Sci 3, 30, 295-299 (2007).

Chapter 3

Theory of Solar Cells

This chapter gives a short introduction into the fundamental concepts and processes in organic solar cell devices and is largely based on 'Organic Solar cells – Materials and Device Physics' by Wallace C. H. Choy, 2012, Springer [1] and 'Device physics of organic solar cells' by Wolfgang Tress, Saechsische Landesbibliothek- Staats- und Universitaetsbibliothek Dresden, 2011 [2]. A focus has been put on aspects relevant to this thesis.

3.1 Introduction

Photovoltaic devices provide direct conversion of light to electricity. The photovoltaic effect was first discovered in 1839 by a French physicist, Alexandre Edmond Becquerel [3]. In 1873, William Adams and Richard Day showed photoconductivity in a solid state device made of a thin layer of selenium placed between two platinum contacts [4]. However, only at the start of the 20th century, electronic properties of organic materials were first studied. In the 1950s, Akamathu H *et al*. discovered that perylene-bromine compound showed fairly good conductivity (~$1\text{-}10^{-3}$ $ohm^{-1}cm^{-1}$) [5]. This study attracted much attention towards organic semiconductors. In 1986, Tang et al. fabricated a thin film, two-layer PV cell where the charge generation efficiency is relatively independent of the bias voltage [51]. Next year, Tang *et al*. showed that a bright luminescence was obtained from an OLED device when two thin organic materials were sandwiched between the electrodes [52]. Since then, OLED's have been used for commercial applications right from small screen cell phones to large screen televisions. In addition to OLEDs, organic

semiconductors are successfully used in Organic Solar Cells (OSCs). In contrast to OLEDs, organic solar cells use organic semiconductors to absorb light and convert them to electricity. Even though inorganic solar cells are the cheapest source of electricity in many countries, organic solar cells can be a good alternative source of energy due to their simple and relatively cheap fabrication process. Roll to roll processing and low temperature deposition techniques are generally used to lower the cost of OSCs. In addition, most inorganic devices require highly pure materials whereas organic cells can be fabricated on plastic films, glass and flexible substrates. OSCs are flexible and light weight; hence can be used in portable applications [7, 8]. In this chapter, we will look into their basic operating principle, architecture, JV characteristics and their recent advancements.

3.2 Overview of Organic Semiconductors

Organic semiconductors are generally carbon based materials with semiconducting properties. In contrast to conventional inorganic semiconductors (silicon or GaAs), which has a covalent structure, organic semiconductors are loosely bound by weak van der Waal's forces. In organic semiconductors, the Highest Occupied Molecular Orbits (HOMO) and the Lowest Unoccupied Molecular Orbits (LUMO) are similar to the Valence Band (VB) and Conduction Band (CB), respectively. All organic semiconducting materials, whether they are small molecules, polymers or any complex biological molecules, depend on π-conjugated systems for conduction. Carbon atoms are sp^2 hybridized and the sp^2 bonds form 3 strong σ-bonds with neighbouring atoms [6]. The remaining p-orbitals of the carbon atoms create a cloud of delocalised electrons by forming weak π-bonds. Based on the electron wavefunction overlap of the neighbouring atom, the π-bond system can have various bonding configurations. When an electron is excited from the HOMO to the LUMO

of the organic semiconductor, the organic molecule itself gets excited into a higher energy state. Charge transport in organic materials occurs though intramolecular carrier movement and intermolecular charge transfer. In organic materials, transport is limited by the weak van der Waals intermolecular coupling, thereby drastically reducing the mobility of the material. Due to weak coupling, charge carriers are strongly localized. Intermolecular transport happens via a hopping process as a charge carrier overcomes an energy barrier to move from one molecule to the next. This hopping process leads to low mobilities in the organic semiconductors ~10^{-3} $cm^2V^{-1}s^{-1}$ compared to inorganic semiconductors (~10^{+3} $cm^2V^{-1}s^{-1}$ for crystalline Si) which could be a serious disadvantage when used in OSCs. To overcome this drawback, various device structures were put forth which will be discussed later in this chapter.

3.3 Basic Principle of OSCs

3.3.1 Light absorption and Exciton generation

A photon incident on an organic semiconductor, possessing energy higher than the band gap of the semiconductor, excites the electron to the lowest unoccupied molecular orbital from the highest occupied molecular orbital. This is comparable to the excitation of electrons from the valence band to conduction band in inorganic semiconductors. Organic semiconductors tend to have larger absorption coefficients than inorganic semiconductors due to the excitonic nature of both semiconductors. Absorption in organic semiconductors results in the formation of strongly bound excitons, which are electrostatically bound electron-hole pairs. These excitons are tightly bound (binding energy ~0.1 - 1 eV) due to the low dielectric constant of organic semiconductors (ε=~3-5), allowing for the Coulombic interactions between the electron and hole to be large.

Absorption in inorganic semiconductors also results in the formation of excitons (Wannier excitons), but their binding energy is significantly lower (~10 meV). This is due to the high dielectric constant of inorganic semiconductors (ε=~11), which reduces the electric field strength between the electron-hole pair. Thus, at room temperature, thermal fluctuations, having energy of ~26 meV, are sufficient to separate the excitons, forming free electrons and holes.

Since the formation of excitons is more energetically favorable than the formation of free electrons and holes due to the Coloumbic interaction between the electron-hole pair, the absorption transition probability increases when stable excitons are formed. When the absorption transition probability is high, the absorption coefficient is larger. Thus, at room temperature, organic semiconductors, which have stable excitons, have larger absorption coefficients than inorganic semiconductors, which have only free electrons and holes.

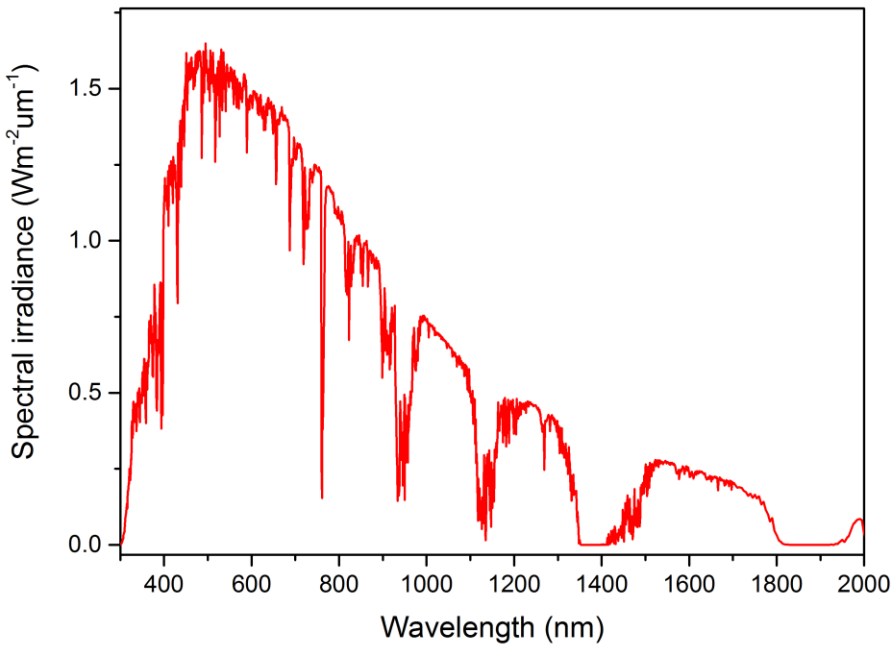

Figure 3.1: AM 1.5G reference solar spectrum.

Fig 3.1 shows the AM 1.5G reference solar spectrum. As mentioned before, the absorption co-efficient of organic materials used in the active layer of OSCs are generally high (~10^5 cm^{-1}), hence a thickness of just few hundred nanometers is more than enough to absorb enough light and show solar cell characteristics. To further increase the absorption, different light trapping techniques like gratings, folded cells and lens concentrations were suggested. The polymers used in the OSCs can absorb only ~30% of the solar energy. By fine tuning (lowering) the band gap of the polymer, it can absorb a large number of photons which will in turn increase the current density of the OSCs. However, it is to be noted that lowering the bandgap to a certain extent will also lower the V_{oc}.

3.3.2 Exciton dissociation and diffusion

To generate current, the tightly bound excitons must be dissociated. Whether the exciton dissociates to generate free charges or remain bound depends on the exciton binding energy relative to the thermal energy (about 25meV at room temperature), and the binding energy intern depends on the inverse of the material's dielectric constant. In contrast to inorganic semiconductors, the binding energy of the exciton in an organic semiconductor is more than one order magnitude higher than the thermal energy. Hence, a driving force is required to split these tightly bound electron-hole pairs. To achieve this, donor and acceptor materials are typically chosen to have electron affinities that differ by 0.1-0.3eV. For example, two different organic materials (X and Y) with the band alignment as shown in fig 3.2 are placed next to each other. Let us say an exciton is generated by the material X, it migrates towards the interface between materials X and Y. The electron is hence transferred from the exciton to $LUMO_Y$ whereas the hole remains in $HOMO_X$. This process of charge transfer is the reason why the material X is named as an electron donor

and Y as an electron acceptor. Since the charge transfer process typically occurs at an ultrafast timescale (30-45fs) [10], the dissociation of the electron-hole pair is very efficient at the donor-acceptor interface. After exciton dissociation, the electron and hole still form coulombically attracted electron-hole pairs called charge-transfer (CT) exciton. This CT exciton has to be separated by an internal field to generate a photocurrent.

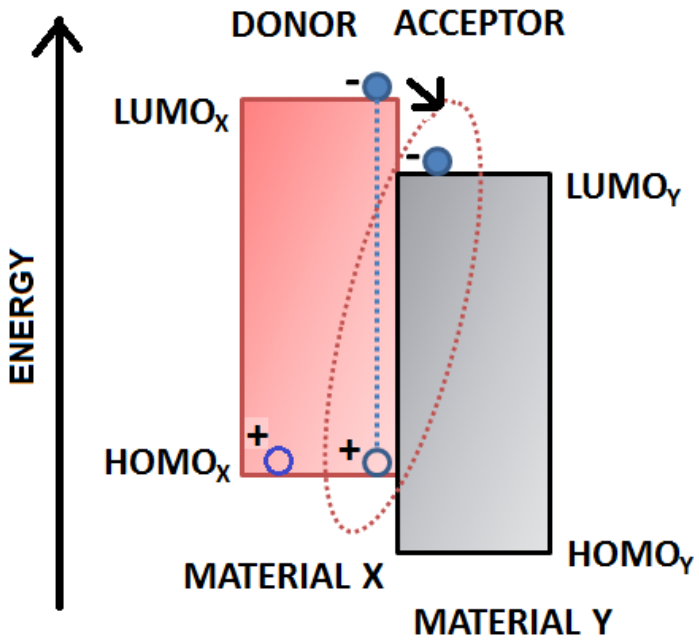

Figure 3.2: Band alignments of donor and acceptor materials for a heterojunction.

In most conjugated polymers, the coulombically bound electron-hole pairs have a lifetime less than 1ns, hence the diffusion length is limited to around 20nm. Diffusion length is basically the distance that excitons can diffuse before they recombine. If the domain size of the donor and acceptor materials are smaller than the diffusion length, excitons can easily arrive at the interface [11,12]. However, if the domain size of the donor and acceptor materials is very small, there is a high chance of recombination [13]. Therefore, exciton diffusion length plays a key role in efficient charge collection.

3.3.3 Charge Carrier Transport

To provide current to an external circuit, the free electrons and holes should reach their respective electrodes within their lifetimes. Drift and diffusion currents are the two significant driving forces to carry electrons and holes to the cathode and anode, respectively. The drift current corresponds to the motion of charge carriers along the potential gradient in the solar cell. Generally, a low work function cathode and high work function anode is used in a solar cell. If an external bias is applied, the drift current starts to change. The holes drift along the direction of the electric field while electrons move in the opposite direction and both electrons and holes are collected in their respective electrodes. The other driving force for carrier transport is the diffusion current, which is basically diffusion of charge carriers along the carrier concentration gradient in a solar cell. It is basically carriers moving from the region of higher concentration, which is common near the heterojunction, to the region of lower concentration, where they eventually become minority carriers. This process continues until the carriers are uniformly distributed. In contrast to drift current, diffusion current takes place when there is no internal electric field.

One of the serious limitations for charge carrier transport is the mobility inside the active layer. Organic materials generally have low carrier mobilities ($\sim 10^{-3} cm^2/Vs$). Hence, the thickness of the active layer should be quite low in order to allow the charge carriers to reach the respective electrodes within their lifetimes. Thus, choosing the right active layer compositions, where there is a proper balance in their electron and hole mobilities, is the key for efficient charge transport in the solar cell.

3.3.4 Charge extraction at electrodes

To efficiently extract charges from the active layer to the electrode, the energy barrier at the active layer/electrode interface should be reduced. If the energy barrier is not minimised, this will lead to a so called S-shaped JV characteristics [14, 15]. This can be achieved by matching the work function of the anode to the donor HOMO and the work function of cathode to the acceptor LUMO. If the HOMO and LUMO of the donor and acceptor are not closer to the work function of the anode and cathode, charge extraction is done by the metal-insulator-metal model [16]. Different types of electrodes are used to match the work function of anode to the donor HOMO. Typically, the anode will be a transparent conducting layer. ITO is the most commonly used anode material as it matches with the HOMO of different donor polymers. Highly conductive PEDOT:PSS, FTO and ZnO:Al can also be used as the anode contact [17, 18, 19]. Whereas, a low work function material like Al (4.3eV) is widely used to match the LUMO of PCBM (Phenyl C_{71} butyric acid methyl ester). Apart from changing the electrode materials, different interlayers are used between the active layer and the electrode for efficient charge collection.

3.3.5 Summary

The overall principle of organic solar cells can be summarised in 4 steps as follows: (1) Photon absorption and subsequent exciton generation; (2) Exciton diffusion into a donor/acceptor interface (3) Dissociation of exciton happens at the Donor/Acceptor interface. Then, the electron and hole still form coulombically attracted electron-hole pairs called charge-transfer (CT) exciton; (4) Carrier transport to the active layer/electrode interface and carrier extraction at the electrodes. They are illustrated in the figure 3.3

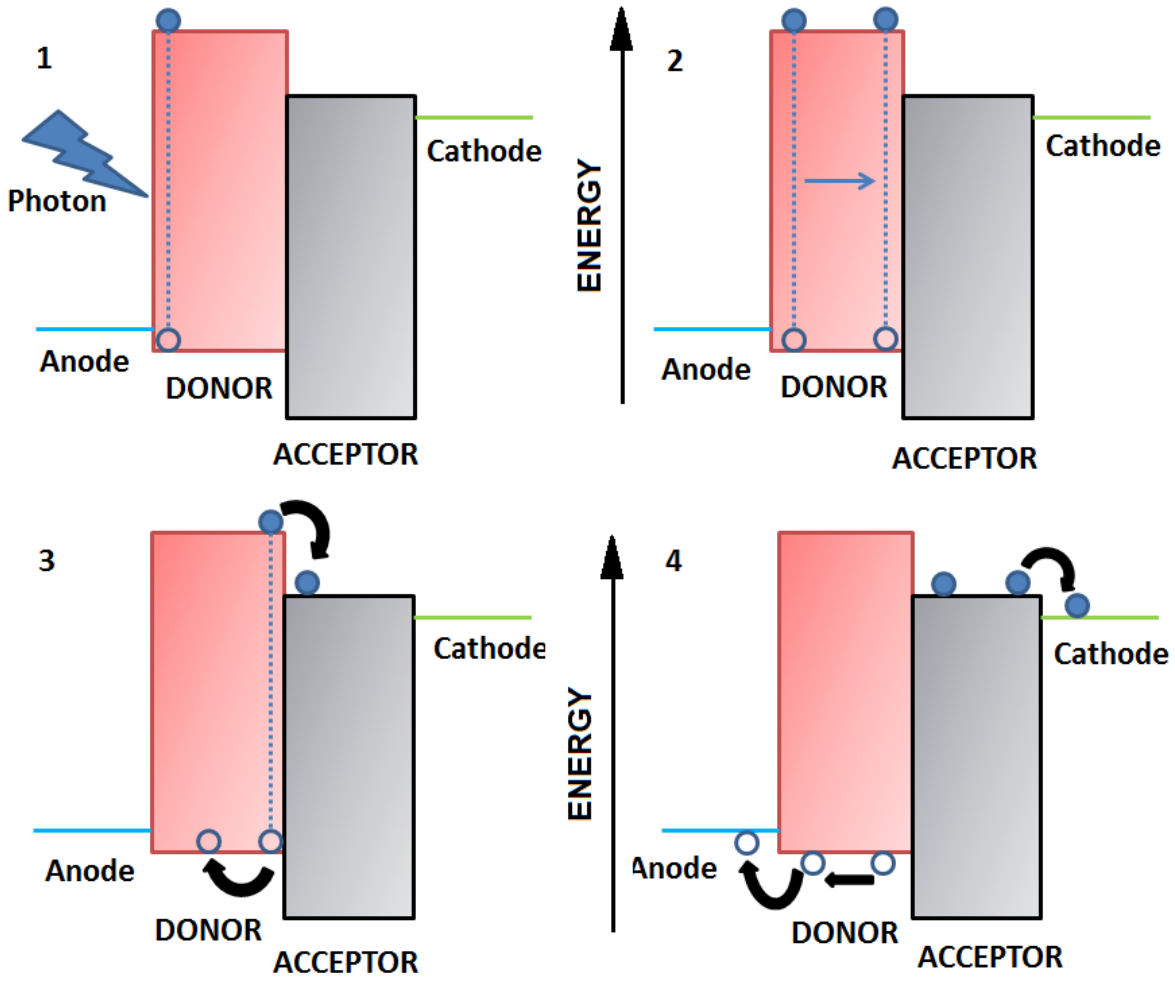

Figure 3.3: Schematic diagram of the Principle of solar cells (1) Photon absorption and exciton generation; (2) Exciton diffusion (3) Exciton dissociation (4) Charge carrier transport to the active layer/electrode interface and carrier extraction at the electrodes.

3.4 Solar Cell Architecture

3.4.1 Single layer solar cells

As seen in figure 3.4, a single layer organic solar cell consists of a photoactive organic semiconducting material sandwiched between two electrodes of different work function. They are often referred to as Schottky type devices or Schottky diodes, as the rectification occurs at only one interface (organic layer/electrode) and the other electrode

forms an ohmic contact with the photoactive material. This type of solar cells gives extremely low efficiencies mainly due to the fact that the electric field, created by the difference in work functions of the electrode material, is too low to separate the photogenerated exciton and the separated charges pass through the same medium causing recombination losses [20].

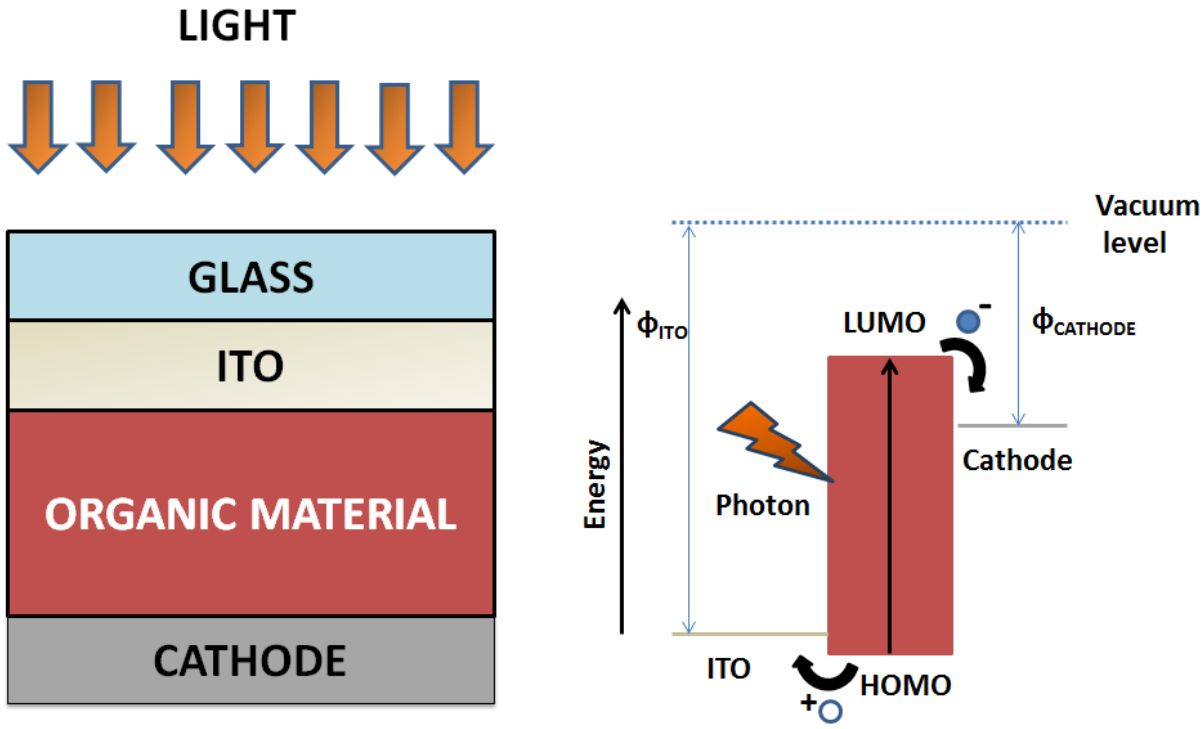

Figure 3.4: Schematic diagram of single layer solar cell and its energy level diagram.

3.4.2 Bilayer solar cells

Bilayer solar cells improve the functionality of the single layer cells by including an acceptor layer between the two electrodes. Tang *et al* [21] demonstrated the formations of heterojunctions, for the first time, by this method and published in 1986. As seen in Fig 3.5, typical bilayer devices consists of an anode, hole collection layer, donor, acceptor, electron collection layer and a cathode. The two layers in between the electron and hole collection

layer have differences in electron affinity and ionisation energy. Hence, electrostatic forces are generated at the interface between the donor and acceptor layer where excitons dissociate. One major disadvantage of bilayer devices is that the organic materials have very short exciton diffusion lengths. As consequence, if the organic layers are too thick, the excitons that are produced away from the donor-acceptor interface may recombine and significantly lower the performance of the devices.

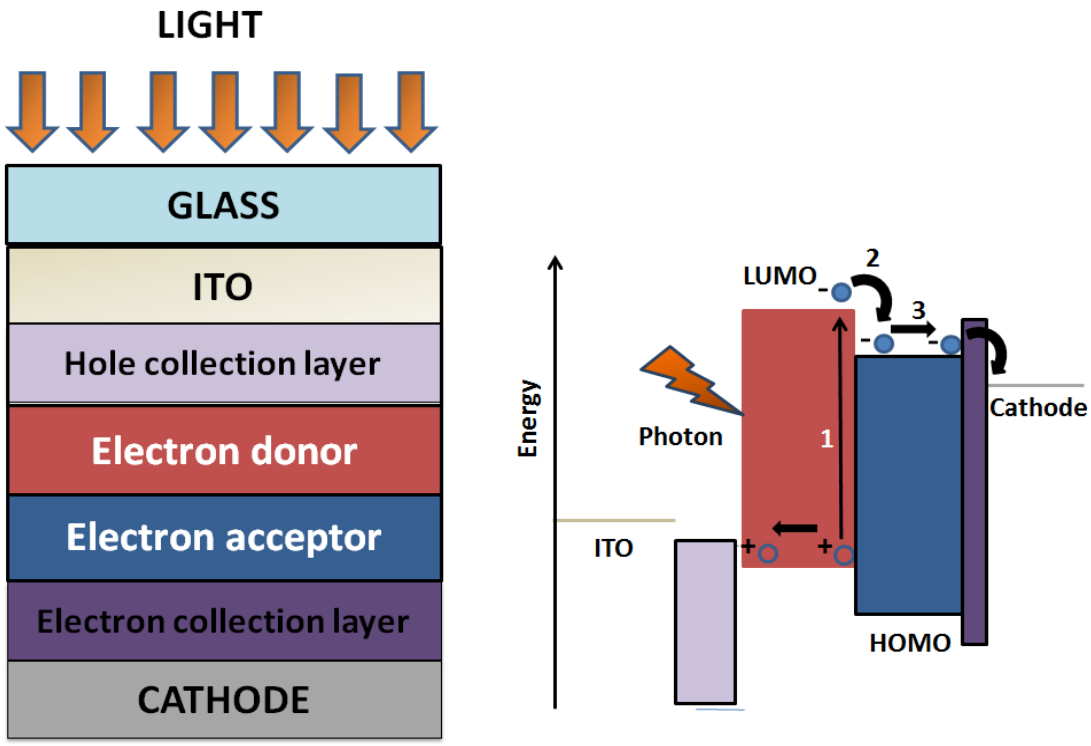

Figure 3.5: Schematic diagram of bilayer solar cell and its energy level diagram.

3.4.3 Bulk heterojunction Solar cells

The first small molecule dye/dye BHJ cell was reported by Hiramoto *et al.* (1991) [47]. G. Yu, A.J Heeger *et al*. gave a breakthrough in the field of organic solar cells by the discovery of the bulk heterojunction in 1995 [48]. The structure of BHJ devices can be seen in Fig 3.6. This bulk heterojunction is formed by mixing the donor and acceptor materials

in solution for several hours and subsequently spin coating, at the desired speeds, on a suitable substrate. The films that are formed are several nanometers thick (~50-300nm). The phase separation in the films (10-20nm) is within the exciton diffusion lengths of many commonly used organic semiconductors. The efficiency of the BHJ devices is significantly improved compared to the bilayer devices. Several research works were carried out with polymers like PPV, P3OT, P3HT as donors and CB-PPV or fullerene derivatives as acceptors and thereby, achieving nearly unity internal quantum efficiency, which means nearly all the photogenerated excitons are dissociated. The charge carriers are then moved to their respective electrodes. Compared to bilayer devices, the thickness of the active layer is quite high. The performance of these devices can be fine-tuned by various parameters including solvent annealing, thermal annealing, and by varying the chain length of the polymer functional groups [22, 23, 24].

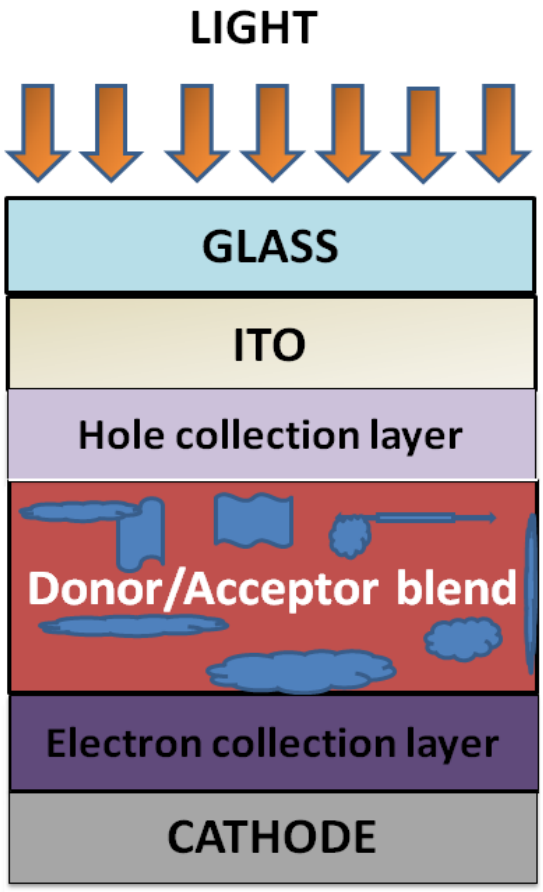

Figure 3.6: Schematic diagram of bulk heterojunction solar cell.

3.4.4 Tandem solar cells

Single junction OSCs have certain limitations including low absorption strength, often narrow absorption and there is the trade-off between the short circuit current density (J_{SC}) and the open circuit voltage (V_{OC}) due to the thermalization of the excited carriers produced by photon energies greater than the energy gap [25]. Hence, as seen in figure 3.7, tandem cells that consist of two or more subcells were proposed. By stacking them in series, we can significantly increase the Voc and by using different donor materials that have complimentary absorption characteristics, the tandem cells can absorb photons over a wider wavelength range. When these subcells are connected in parallel, the Jsc is basically

the sum of the current outputs from the two subcells. To produce high efficiencies in tandem cells, interlayers should be transparent and facilitate effective recombination. Charge accumulation in one of the subcells, due to the current mismatch between the subcells, should also be taken into consideration. Recently, organic tandem cells, which can absorb photons from 350nm-950nm, have achieved 15% efficiency [26] and more recently, Lingxian Meng *et al*. have shown that a solution processed 2-terminal (2T) monolithic tandem OSC cell gave an efficiency of 17.36% [28].

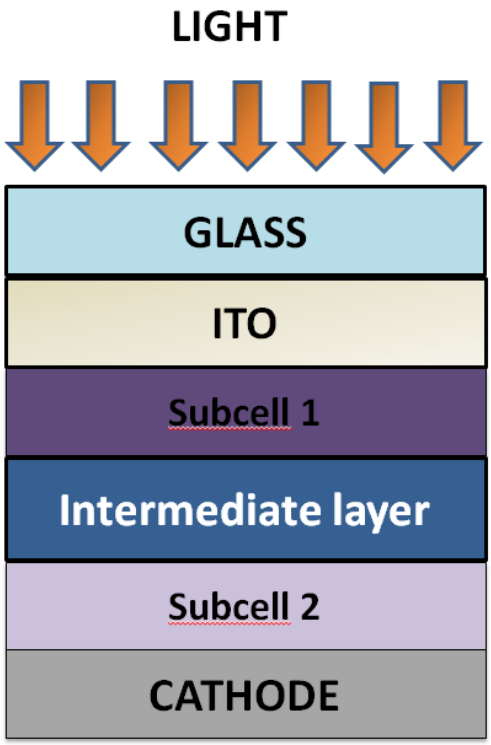

Figure 3.7: Structure of a two terminal, two subcell tandem cell.

3.5 Characterization of OSCs

3.5.1 J-V characteristics

Organic solar cells are characterised under 1000W/m^2 light of AM 1.5 solar spectrum (T=25°C) generated from a source set with a reference cell and corrected spectral errors [27]. The operation of solar cells at different biases can be seen in the figure 3.8

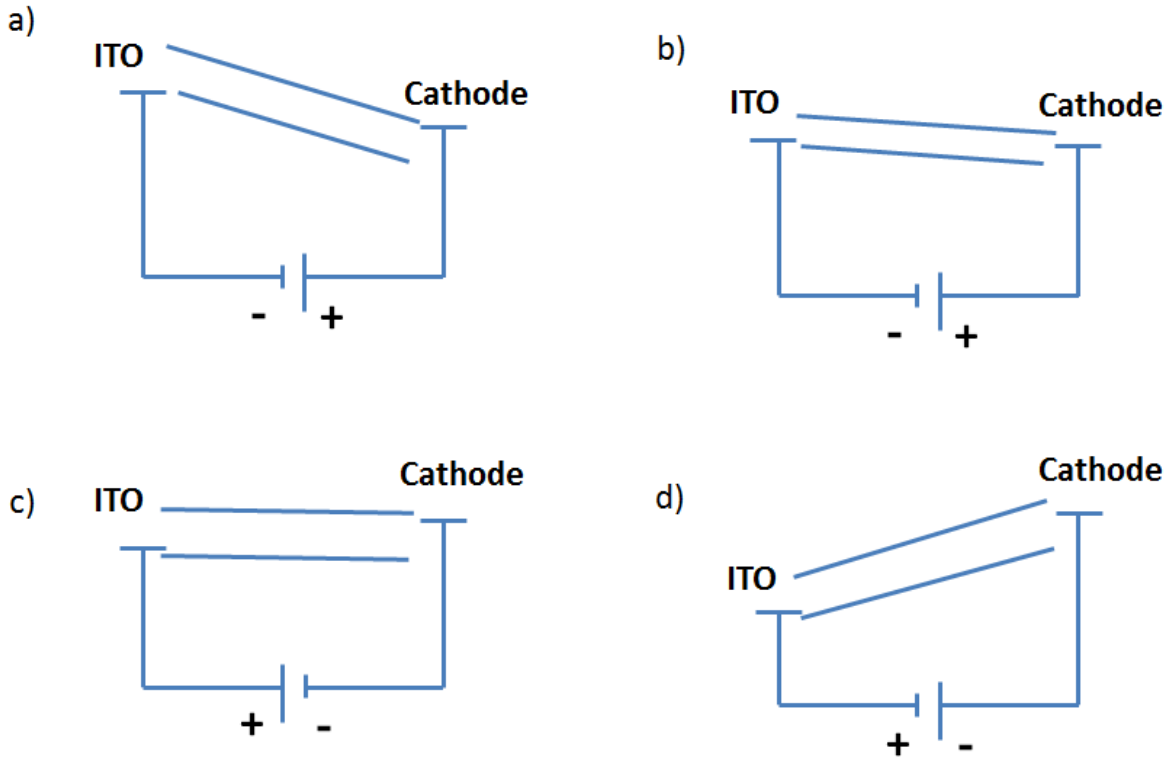

Figure 3.8: Operation of a solar cell at different bias: a) Large reverse bias; b) small reverse bias; c) positive bias, resultant internal field = 0; d) positive bias, carrier injection.

a) During reverse bias, the applied bias reinforces the built-in electric field thereby significantly improving the charge carrier extraction and transport. As mentioned in the previous section, drift current is dominant due to the strong electric field. b) When the applied bias is close to none, the built-in electric field helps in the charge collection at the

corresponding electrodes. When the applied bias is increased in the positive direction, the positive bias opposes the built-in electric field. This causes the electric field inside the cell to decrease and the drift current also gets smaller. c) When the applied electric field is equal to the built-in field, diffusion current dominates as the electric field is quite small inside the device. d) When the external bias is further increased, the applied electric field is now larger than the built-in field. The potential gradient is reversed and the current is now positive. When the current and applied bias are in opposite direction, power is outputted from the cell. The point where the magnitude of the product of J and V is maximum is the maximum power power output point. The following parameters generally used to evaluate the characteristics of an organic solar cell.

Short circuit current (Jsc): It is defined as the current at which the externally applied voltage is 0. In short circuit conditions, the number of charge carriers that are produced and then collected at the electrode is represented by Jsc which depends on various parameters like the band gap of the polymer, its molar extinction co-efficient, carrier mobility, and phase separation. Open circuit voltage (Voc) is defined as the voltage at which the current density output is 0.

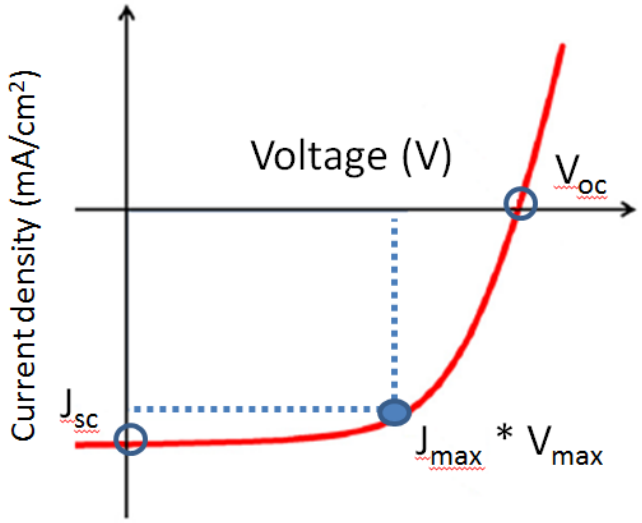

Figure 3.9: Basic JV characteristics of an organic solar cell.

Fill Factor (FF): The fill factor is defined as

$$FF = \frac{J_{max}V_{max}}{J_{sc}V_{oc}} \quad \textbf{[3.1]}$$

Where J_{max} and V_{max} represent the current density and voltage at maximum power output, respectively. It is defined as the ratio between maximum power output and the product of short circuit current and open circuit voltage. The fill factor is a measure of the ‘’squareness’’ of the JV curve. The fill factor shows dependence of the current output on the applied bias of the device and is quantified by the series and shunt resistance. For example, low carrier mobility causes carriers to recombine before they reach a heterojunction. Here, increasing the external bias will sweep the carriers, which otherwise may recombine at lower field strength, causing an increase in the output current. This leads

to a strong dependence of current on the applied bias, which is presented by lower Fill factor.

Power conversion efficiency (PCE): The PCE represents the efficiency of the solar cell and is calculated from the JV characteristics of the solar cell as shown in Fig 3.9. It is defined by the product of J_{max} and V_{max} divided by the illumination intensity P_{in}, can be re-written as a function of J_{sc} and V_{oc} with the fill factor as new proportional constant.

$$\eta = \frac{J_{max}V_{max}}{P_{in}} = \frac{J_{sc}V_{oc}FF}{P_{in}} \quad \textbf{[3.2]}$$

3.5.2 External quantum efficiency (EQE)

In addition to the JV characteristics, the solar cells can be characterised by external quantum efficiency. It helps us understand how efficient a solar cell is in converting light into electricity at different wavelengths is. EQE basically represents the percentage of incident photons that gets converted to charge carriers and subsequently gets collected at the electrode under short circuit conditions. One of the best ways to improve the absorption of photons at a particular wavelength of the solar cell is to monitor the EQE which is highly dependent on the absorption spectrum of the active layer.

During the measurements, if the reference solar cell has similar characteristics of that of the cell under testing, the JV characteristics are quite straightforward. But, if Si reference cell is used as a reference cell when organic solar cells are tested, some deviations occur due to the mismatch between the responsively of the two cells. The spectral mismatch (MM) for an illumination with spectrum SoSim (λ) given as spectral photon flux density (γ) can then be calculated as:

$$MM(V) = \frac{\int EQE(\lambda,V) SoSim^{\gamma}(\lambda) d\lambda / \int SoSim^{\gamma/P}(\lambda) d\lambda}{\int EQE(\lambda) AM1.5g^{\gamma}(\lambda) d\lambda / AM1.5g^{\gamma/P}(\lambda) d\lambda} \quad \textbf{[3.3]}$$

It is the measurement of the sensitivity of the solar cell with respect to the illumination spectrum. Hence, the spectral mismatch is quite important for OSCs with distinctive features in the EQE. The normalisation in eq. 3.3 can be done with respect to the photon number ($^{\gamma}$) or more commonly to the incident intensity (^{P}).

For organic solar cells, the MM can have a strong bias dependence. Following the international standards for the mismatch corrections, the MM is measured at 0 external bias of the (sub) cell. As the photocurrent of the Si diode is used to change the intensity of the solar simulator, a correction factor m is needed.

$$m = \frac{J_0^{ref}}{J_{sel}^{ref}} = \frac{\int EQE^{ref}(\lambda) AM1.5g^{\gamma}(\lambda) d\lambda}{\int EQE^{ref}(\lambda) SoSim^{\gamma}(\lambda) d\lambda} \frac{\int EQE(\lambda,V) SoSim^{\gamma}(\lambda) d\lambda}{\int EQE(\lambda) AM1.5g^{\gamma}(\lambda) d\lambda} \quad \textbf{[3.4]}$$

EQE is also dependant on the electrical characteristics of the solar cell. Even a slight change in the charge collection, at the electrodes, is reflected in the form of shifts in the EQE spectrum [49].

3.6 Origin and Recent Advancements of SWNT based OSCs

As discussed in the previous sections of this chapter, the inherent property of organic semiconductor, including the formation of tightly bound electron-hole pairs immediately after photo generation, which require dissociation prior to charge separation, low exciton diffusion lengths, and low charge carrier mobilities, are some of the factors that hinder the efficiency of OSCs. Significant progress has been made in the morphology of active layers to facilitate efficient light absorption, improved exciton dissociation and high carrier mobilities [29, 30, 31, 32]. However, a highly stable and efficient charge transporting materials with high mobilities is one of the key factors for long term stable

cells. Carbon nanotubes are therefore excellent candidates as they satisfy all the above criteria [33].

At first, SWNTs were used as alternative for fullerene (as electron accepting materials) which yielded a much higher open circuit voltage (1.81 V) but the efficiency of those devices were significantly lower compared to the ones that used fullerene derivatives [34, 35, 36, 37, 38, 39]. The cells with P3HT-NT as electron acceptors yielded an efficiency of 0.74% whereas the reference cell with fullerene gave 5% efficiency [40]. The concentrations of SWNTs also play a major factor in determining the efficiency of the device. If the concentration is too low, it might hit the lower percolation threshold limit. If the concentration is too high, it will lead to shunting and increased recombination. In addition, the presence of metallic tubes has always been the reason for the low performance of organic solar cells [41, 42].

Surface potential measurements were taken to see whether P3HT-NT act as an electron transporting layer or hole transporting layer using a Kelvin probe force microscope. Interestingly, at the polymer-SWNT interface, holes are transferred to SWNTs rather than electrons [53]. Fei Lan et al. fabricated a device that could extract one type of charge carrier to the ground, allowing the Polymer-SWNT heterojunction to be dominated by either electron or hole transfer. In an electron dominated environment, no changes in surface potential of SWNTs could be measured. Whereas, when electrons were extracted in the ground, resulting in an accumulation of holes and thus making Polymer-SWNT interface hole dominated, the surface potential of SWNTs would shift due to illumination.

Dissanayake *et al*. and Lan *et al*., suggested that SWNTs can be used as hole transporting layers rather than as electron acceptors [43, 44]. When Chaudhary *et al*. incorporated SWNTs in different layers of organic solar cell; the performance was highest

for the devices where SWNTs was placed in a hole transporting interface [45]. Whereas, when the devices were placed in an electron transporting interface, the efficiency was too low. To follow up with this work, Dabera *et al*. studied the charge transfer characteristics of P3HT-SWNT hybrids and confirmed the hole transport by both spectroscopic analysis and electrical measurements [46]. They also fabricated a PTB7:PCBM based device using P3HT-SWNT as the only hole transporting layer which yielded a 32% increase in the fill factor and a PCE of 7.6% was achieved. To the best of our knowledge, this is the highest efficiency till now for a SWNT based organic solar cells. However, there are no studies with regards to the long term stability of the device and how they behave when they are placed in an inverted organic solar cell.

3.7 Summary

In summary, a quick overview of organic semiconductors was discussed. The basic principle of OSCs including photon absorption, exciton generation, exciton dissociation, charge transport, and collection were discussed in detail. Different architecture of OSCs including single layer, bilayer, BHJ and tandem cells were described. The JV characteristics of OSCs and the mismatch factor were also briefed. Finally, the recent advancements in SWNT based organic solar cells including the recent, state of the art, devices were discussed.

Reference

[1]. 'Organic Solar cells – Materials and Device Physics' by Wallace C. H. Choy, Springer (2012).

[2]. 'Device physics of organic solar cells' by Wolfgang Tress, Saechsische Landesbibliothek- Staats- und Universitaetsbibliothek Dresden, (2011).

[3]. V. Petrova-Koch. Milestones of Solar Conversion and Photovoltaics. In High-Efficient Low-Cost Photovoltaics. Springer Berlin Heidelberg, (2009).

[4]. W. Smith. Nature 303 (1873).

[5]. Akamathu H et al., Nature 173 168–169 (1954).

[6]. Jason D. M. and JIANGENG X. Polymer Reviews, 52 1–37 (2012).

[7]. Paul Sullivan, Stefan Schumann, Raffaello Da Campo, Thomas Howells, Amelie Duraud, Michael Shipman, Ross A. Hatton, Tim S. Jones. Adv. Energy Mater. 3 239–244 (2013).

[8]. Rui Z et al. 5(12) 9877–9882 (2011).

[9]. Mayer AC, Scully SR, Hardin BE, Rowell MW, McGehee MD, Mater Today 10 28–33 (2007).

[10]. Grancini G, Maiuri M, Fazzi D, Petrozza A, Egelhaaf H. J, Brida D, Cerullo G, Lanzani G, Nat Mater, advance online publication (2012).

[11]. Yu G, Gao J, Hummelen J. C, Wudl, F, Heeger A. J. Science 270 1789− 1791 (1995).

[12]. Halls J. J. M, Walsh C. A, Greenham N. C, Marseglia E. A, Friend R. H, Moratti S. C, Holmes A. B. Nature 376 498−500 (1995).

[13]. Lakhwani G, Rao A, Friend R. H. Annu. Rev. Phys. Chem. 65 557− 581 (2014).

[14]. Wagenpfahl A, Rauh D, Binder M, Deibel C, Dyakonov V Phys Rev B 82 115306 (2010).

[15]. Tress W, Leo K, Riede M Adv Funct Mater 21 2140 (2011).

[16]. Parker I J Appl Phys 75(3) 1656 (1994).

[17]. Jaber S, Ali F, TayebehSaghaei Organic Electronics 24 188–194 (2015).

[18]. Xiaoming Yu et al., Solar Energy Materials & Solar Cells 136 142–147 (2015).

[19]. K. Schulze, C. Uhrich, R. Schueppel, K. Leo, M. Pfeiffer, E. Brier, E. Reinhold, and P. Baeuerle, Appl. Phys. Lett. 91 073521-073523 (2007).

[20]. H. Spanggaard and F. C. Krebs, Sol. Energy Mater. Sol. Cells, 83(2–3) 125–146 (2004).

[21]. Tang C. Two-layer organic photovoltaic cell. Appl Phys Lett 48(2) 183 (1986).

[22]. Savenije TJ, Kroeze JE, Yang X, Loos J Adv Funct Mater 15(8) 1260–1266 (2005).

[23]. Li G, Yao Y, Yang H, Shrotriya V, Yang G, Yang Y, Adv Funct Mater 17(10) 1636–1644 (2007).

[24]. Chen H-Y, Hou J, Zhang S, Liang Y, Yang G, Yang Y, Yu L, Wu Y, Li G. Nat Photon 3(11) 649–653 (2009).

[25]. Hong, Z., Dou, L., Li, G. & Yang, Y. (eds Yang, Y. & Li, G.) Ch. 11 (Springer, Berlin, Heidelberg (2015).

[26]. Xiaozhou Che1 , Yongxi Li2 , Yue Qu2 and Stephen R. Forrest Nature Energy 3 422–427 (2018).

[27]. Shrotriya V, Li G, Yao Y, Moriarty T, Emery K, Yang Y Adv Funct Mater 16(15) 2016–2023 (2006).

[28]. L. Meng et al., Science 10.1126/science.aat2612 (2018).

[29]. Y. Liang, Z. Xu, J. Xia, S.-T. Tsai, Y. Wu, G. Li, C. Ray, and L. Yu, Adv. Mater. 22 E135 (2010).

[30]. L. Lu and L. Yu, Adv. Mater. 26 4413 (2014).

[31]. J. Peet, J. Y. Kim, N. E. Coates, W. L. Ma, D. Moses, A. J. Heeger, and G. C. Bazan, Nat. Mater. 6 497 (2007).

[32]. K.-H. Ong, S.-L. Lim, H.-S. Tan, H.-K. Wong, J. Li, Z. Ma, L. C. H. Moh, S.-H. Lim, J. C. de Mello, and Z.-K. Chen, Adv. Mater. 23 1409 (2011).

[33]. Xinjian Zhou, J-y Ji-Yong Park, Shaoming Huang, Jie Liu & Paul P.L. McEuen. Physical Review Letters, 95 14 146805 (2005).

[34]. E. Kymakis & G. a. J. Amaratunga. Applied Physics Letters, 80 (1) 112 (2002).

[35]. Brian J. Landi, Ryne P. Raffaelle, Stephanie L. Castro & Sheila G. Bailey. Progress in Photovoltaics: Research and Applications, 13(2) 165–172 (2005).

[36]. E. Kymakis, I. Alexandrou & G. a. J. Amaratunga. Journal of Applied Physics, 93 3 1764 (2003).

[37]. Emmanuel Kymakis & Gehan A J Amaratunga. Reviews on advanced materials science, 10 300–305 (2005).

[38]. E Kymakis, E Koudoumas, I Franghiadakis & G A J Amaratunga. Journal of Physics D: Applied Physics, 39 (6) 1058–1062 (2006).

[39]. Rodolfo L. Patyk, Bruno S. Lomba, Ana Fl´avia Nogueira, Clasc´ıdia A. Furtado, Adelina Pinheiro Santos, Regina M Q Mello, Liliana Micaroni & Ivo A. H¨ummelgen. Physica Status Solidi - Rapid Research Letters, 1 (1) 43–45 (2007).

[40]. Marisol Reyes-Reyes, Kyungkon Kim & David L. Carroll. Applied Physics Letters, 87(8) 3–6 (2005).

[41]. Liming Liu, William E. Stanchina & Guangyong Li. Applied Physics Letters, 94 (23) 50–53 (2009).

[42]. Shenqiang Ren, Marco Bernardi, Richard R Lunt, Vladimir Bulovic, Jeffrey C Grossman & Silvija Gradeˇcak. Nano Letters, 11 (12) 5316–5321 (2011).

[43]. Fei Lan & Guangyong Li. Nano Letters, 13 5 2086–91 (2013).

[44]. Nanditha M Dissanayake & Zhaohui Zhong. Nano Letters, 11 (1) 286–90 (2011).

[45]. Sumit Chaudhary, Haiwei Lu, Astrid M M¨uller, Christopher J Bardeen & Mihrimah Ozkan. Nano Letters, 7 (7) 1973–9 (2007).

[46]. G Dinesha *et al.* ACS nano, 7 (1) 556–65 (2013).

[47]. Hiramoto *et al.* Appl. Phys. Lett. 58, 1062 (1991).

[48]. J.G. Yu, J.Gao, J. C. Hummelen, A. J Heeger, Science 270, 1789-1791 (1995).

[49]. 'Organic solar cells' by Wolfgang Tress, ISSN 2196-2812 (2014).

[50]. S. M. Sze, Physics of semiconductor devices, Wiley, New York (1981).

[51]. C. W. Tang Appl. Phys. Lett. 48, 183 (1986).

[52]. C.W. Tang and S. A. Vanslyke Appl. Phys. Lett. 51, 913 (1987).

[53]. Fei et al. Nano Letters, 1, 5, 2086-91 (2013).

Chapter 4

Materials and Methods

This section of the thesis describes the materials & methods used to prepare and fabricate the SWNT-Polymer hybrids and organic solar cell devices, respectively.

4.1 Materials

4.1.1 Single-wall carbon nanotubes

Different chirally controlled Single Walled Carbon nanotubes (SWNTs) starting material were used in this thesis. All the samples were purchased externally and received in powder form.

a) SG65i - Semiconducting Single Walled Carbon nanotubes Enriched in Chirality (6,5)
    - ≥95% carbon basis (≥95% as CNTs)
    - ≥93% semiconducting tubes
    - 0.78 nm average diameter
    - Diameter range from 0.7-0.9nm
    - Dominating SWNT species - (6,5)
    - length >1 μm
    - CoMoCAT process, Sigma-Aldrich
b) SG76 - Single Walled Carbon nanotubes Enriched in Chirality (7,6)
    - ≥90% carbon basis (≥77% as CNTs)
    - ≥66% semiconducting tubes

- 0.83 nm average diameter
- Diameter range from 0.7-1.1nm
- Dominating SWNT species – (7,5)
- length >1 μm
- CoMoCAT process, Sigma-Aldrich.

c) CG100 - Economical Single Walled Carbon nanotubes

- CG 100 ≥89% carbon basis (≥99% as CNTs),
- 0.82 nm average diameter
- Diameter range from 0.7-1.3nm
- Dominating SWNT species - (7,5) and (7,6)
- length >1 μm
- CoMoCAT process, Sigma-Aldrich.

d) HiPco (raw) – wide diameter range Single Walled Carbon nanotubes

- ~35wt% iron catalyst impurities
- Diameter range from 0.7-1.4 nm
- Dominating SWNT species - (8,6)
- length >1 μm
- HiPco process, NanoIntegris

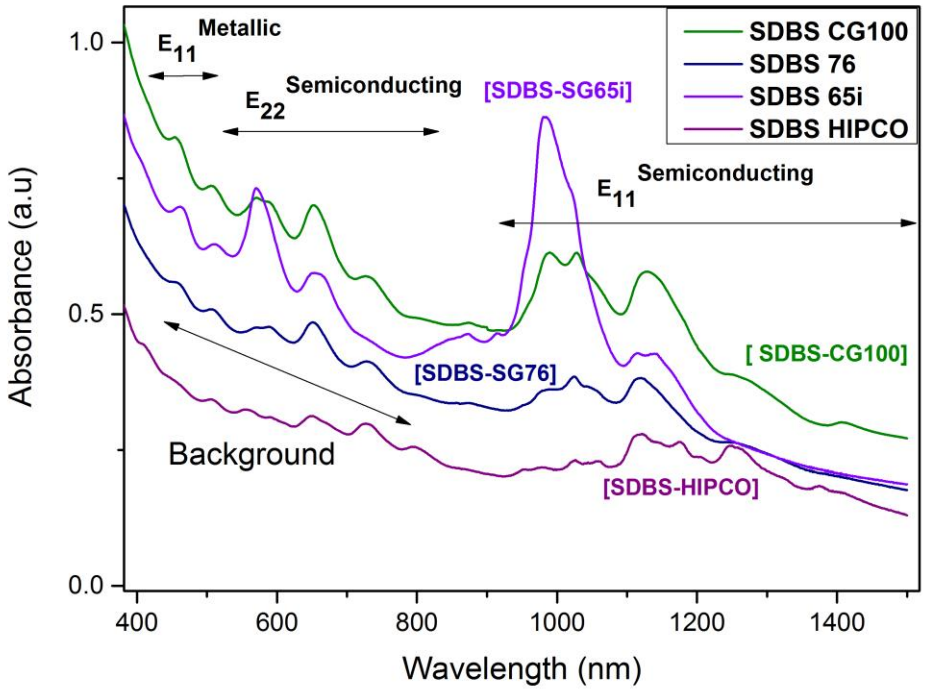

Fig 4.1: Absorption Spectra of SWNT starting materials in SDBS solution.

The distribution of different SWNT starting materials in SDBS solution can be seen in the absorption spectra shown in fig 4.1.

4.1.2 Polymers

- PFO - Poly(9,9-di-*n*-octylfluorenyl-2,7-diyl) was purchased from American Dye Source (MW 36,000 $gmol^{-1}$)

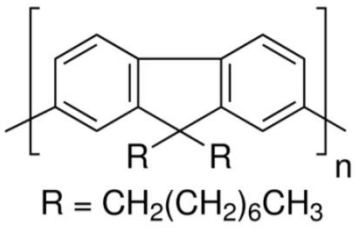

Fig 4.2: Molecular structure of PFO.

- F8BT - poly(9,9'-dioctyluorene-co-benzothiadiazole) was purchased from American Dye Source (MW 96,000 $gmol^{-1}$)

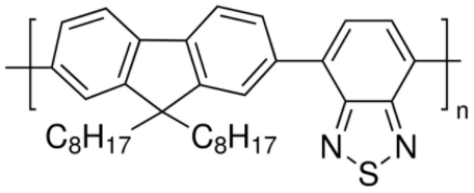

Fig 4.3: Molecular structure of F8BT.

- P3HT - poly(3-hexylthiophene-2,5-diyl) was purchased from Sigma-Aldrich (MW 35,000 $gmol^{-1}$)

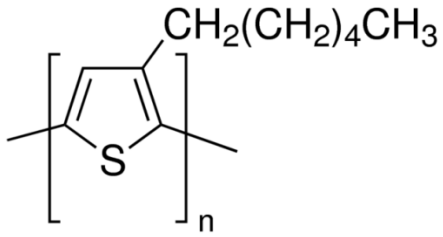

Fig 4.4: Molecular structure of P3HT

- PFN - Poly [(9,9-bis(3'-(N,N-dimethylamino)propyl)-2,7-fluorene)-alt-2,7-(9,9–dioctylfluorene)] was purchased from Ossila Ltd.

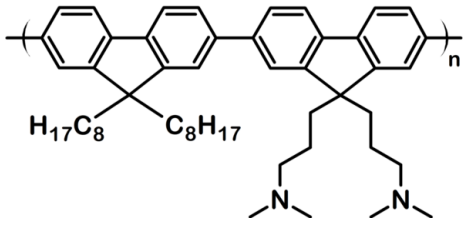

Fig 4.5: Molecular structure of PFN.

- C6, C8, C10 and C12 – These fully conjugated polytriaryl amine based polymers were obtained from our collaborators in Taiwan [Prof. Liaw from National Taiwan University]

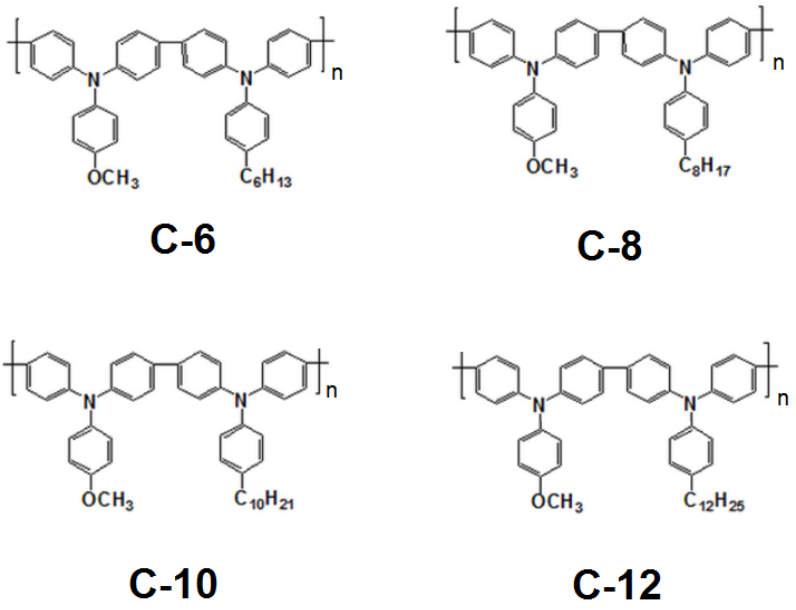

Fig 4.6: Molecular structure of C6, C8, C10 and C12.

- PTB7 - Poly[[4,8-bis[(2-ethylhexyl)oxy]benzo[1,2-b:4,5-b']dithiophene-2,6-diyl][3-fluoro-2-[(2-ethylhexyl)carbonyl]thieno[3,4-b]thiophenediyl]] was purchased from 1-Material Inc (MW 97,000 $gmol^{-1}$)

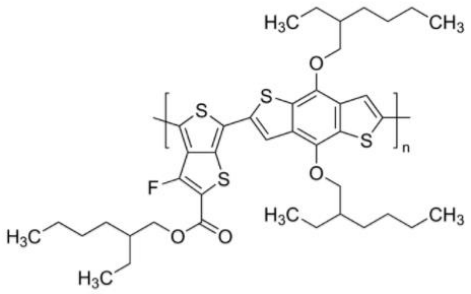

Fig 4.7: Molecular structure of PTB7.

- PEDOT:PSS – Poly(3,4-ethylenedioxythiophene)-poly(styrenesulfonate) was purchased from Ossila Ltd.

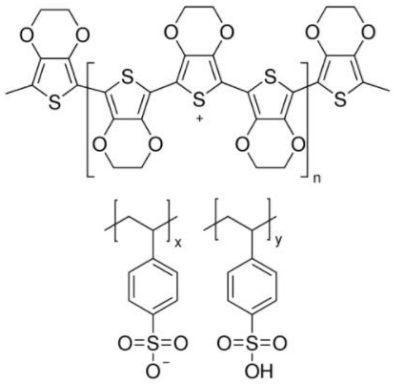

Fig 4.8: Molecular structure of PEDOT:PSS.

4.1.3 Small Molecules

- Spiro-O-MeTAD - 2,2',7,7'-Tetrakis[N,N-di(4-methoxyphenyl)amino]-9,9'-spirobifluorene was purchased from Borun chemicals (MW 1225 $gmol^{-1}$)

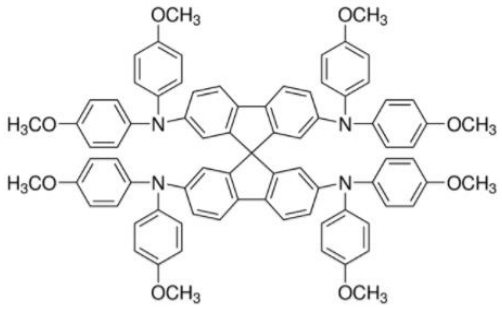

Fig 4.9: Molecular structure of Spiro-O-MeTAD.

- SDBS - Sodium dodecylbenzenesulfonate was purchased from Sigma-Aldrich (MW 348 $gmol^{-1}$)

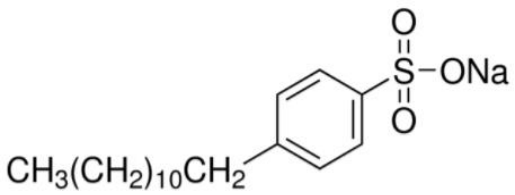

Fig 4.10: Molecular structure of Spiro-O-MeTAD.

4.2 Experimental Methods

4.2.1 Preparation of SDBS-SWNT aqueous dispersions

The surfactant Sodium dodecyl benzene sulfonate (SDBS), is generally used as an effective dispersing agent to break SWNT bundles. [1] 350mg of SDBS was added to 35ml of deuterated water (D_2O) and placed in a low power sonic bath until the surfactant was fully dissolved. 15mg of SWNT starting material (SG65i, SG76, CG100 or HIPCO) was added to the above solution. The mixture was then tip sonicated for 30 minutes using a highly powerful ultrasonic probe (Soniprep 150), vibrated at 23KHz. As the SWNT surface is highly hydrophobic, the aliphatic chains of the SDBS can efficiently coat the nanotube surface through π-π stacking in aqueous dispersions. In order to separate the surfactant coated SWNTs from the remaining bundles; the mixture was then ultra-centrifuged at 100,000×g for 4 hours. The top 80% of the supernatant was decanted and referred to as SDBS-SWNT.

4.2.2 Preparation of Polymer-SWNT nanohybrids

The Polymer-SWNT nanohybrids were prepared by the method developed by Schuettfort *et al* [2]. Briefly, 6mg of Polymer was dissolved in 10ml of the desired solution (Chlorobenzene/o-xylene) by warming gently in a sonic bath. Then, 3mg of SWNT starting

material (SG65i, SG76, CG100 or HIPCO) was added to that solution. The mixture was then tip sonicated for 15 mins in a beaker of ice water in order to maintain the temperature of the solution constant at 25ºC, followed by centrifugation at 10,000g for 10 minutes to remove the bundled and unwrapped SWNTs. The top 80% of the supernatant was retained and the residue was removed. In order to remove the excess polymer, an orthogonal solvent (Toluene) was added at the ratio of 1:1 to the supernatant solution followed by warming the mixture in a sonic bath. This induces aggregation of the nanohybrids which can be precipitated out by centrifuging at 16,000g for 4mins. The nanohybrid pellets were then re-dissolved in any desired solvent by either tip sonicating it for 2 minutes or keeping it in a low power sonic bath for 15 minutes. This procedure was repeated several times to remove the excess polymer. The final nanohybrids were then used for characterization and fabrication of OSCs.

4.2.3 Solar Cell Fabrication

Electron donor material PTB7 and electron acceptor PC71BM were purchased from 1-material Chemscitech and Aldrich, respectively, and used as received. The PEDOT:PSS (Clevios P AI4083) was obtained from Ossila Ltd. The conventional structure was ITO/P3HT-NT/PTB7:PC71BM(1:1.5 by weight)/PFN/Ag and the inverted device structure was ITO/PFN/PTB7:PC71BM/MoO3/PEDOT:PSS (modified)/P3HT-NT/Ag. For regular devices, a ~3 nm thick, metallic nanotube free, P3HT-NT layer was spin-cast from a chloroform solution on a precleaned ITO substrate, which was treated by oxygen plasma for 4 min, at 1000rpm for 1 min and then dried at 120 degree Celsius for 10 minutes. The PTB7:PC71BM active blend layer, with a nominal thickness of ~85nm was prepared by spin-coating a mixed solvent of chlorobenzene/1,8-diiodoctane (97:3% by volume) solution

(concentration, 25 mg/ml) at 900 rpm for 2 min. The PFN interlayer material was dissolved in methanol in the presence of a small amount of acetic acid and its solution (concentration, 2 mg/ml) was spin-coated on top the active layer to give a thickness of 6 nm and a 100 nm Ag layer was subsequently evaporated through a shadow mask to define the active area of the devices (0.0625 cm2) and eliminate edge effects. For an inverted device, PFN was spin coated on the ITO substrate at a nominal thickness of 6 nm, followed by spin coating a ~85 nm thick active layer. Modified protective coating (MoO3:PEDOT:PSS) was spin coated on top of the active layer [15, 16]. The nanotubes were then spin coated on top of the modified PEDOT:PSS followed by evaporating 100nm of Ag. For the reference cell, we thermally evaporate MoO3 on the active layer followed by evaporating 100nm of Ag. Schematic diagrams of both these conventional and inverted devices can be seen in Chapter 7 (Fig 6).

4.3 Characterization Methods

4.3.1 Absorption Spectroscopy

Absorption spectroscopy is a powerful tool to quantify nanotube dispersion properties and characterize the polymer at the same time by applying a suitable light source on the nanohybrid solution, and correlating the quantity of light absorbed [3]. This technique is used to identify individual SWNTs by relating the absorption intensity at a particular wavelength to the concentration of SWNTs suspended in the solution through the Beer-Lambert law [4]. The Beer's law states that the absorption of monochromatic light by a homogenous isotropic medium is proportional to the absorption path length l, and to the concentration c. Beer's law can be expressed as

$$A = \log_{10} \frac{I_o}{I} = \varepsilon l c \qquad \textbf{[4.1]}$$

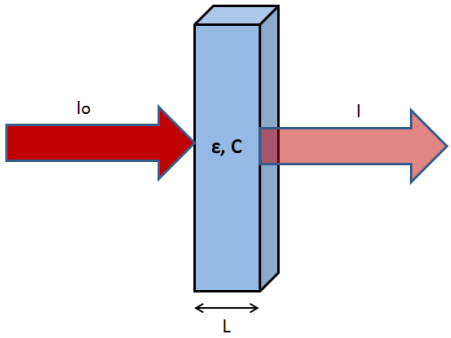

Fig 4.11: Diagram that illustrates Beer-Lambert's law.

where I_0 and I are intensities of incident and transmitted light, respectively. The constant ε is called molar decadic extinction coefficient. The Beer – Lambert law is valid only if the spectral bandwidth of the light is narrower to spectral line widths. If not, the effective ε decreases with increasing bandwidth of the radiation.

Perkin-Elmer Lambda 9 UV-Vis-NIR Spectrophotometer was used to measure the absorbed light intensity as a function of wavelength, at room temperature. It has a double holographic grating monochromators for super low stray light performance (<0.00007%T at 220nm). This dual beam spectrophotometer has deuterium (UV-vis) and tungsten halogen (NIR) light sources which generates a light beam across the spectral range of 175nm-3500nm. Hence, they were a perfect choice to measure the key polymer and SWNT transitions (E_{11} and E_{22}) which can be seen between 300nm-1500nm.

4.3.2 Photoluminescence Excitation (PLE) Spectroscopy

Photoluminescence excitation mapping is a powerful tool to determine individual chiralities of semiconducting SWNTs depending on their E_{22} and E_{11} transitions. This process involves recording the PL intensities of the Polymer-SWNT hybrids while photoexciting the SWNT E_{22} transitions. Photoluminescence excitation maps were taken using a custom build setup [5] consisting of 75 W Xenon lamp focused into a monochromator, which then illuminated the nanohybrid films on a quartz substrate. Different filters were used to remove the unwanted wavelengths emerging from the monochromator. A beam splitter is used to divert a tiny portion of the beam to a Si photodiode and the photovoltage readings were measured using an amplifier and a multimeter, which is then used to normalise the acquired PL data.

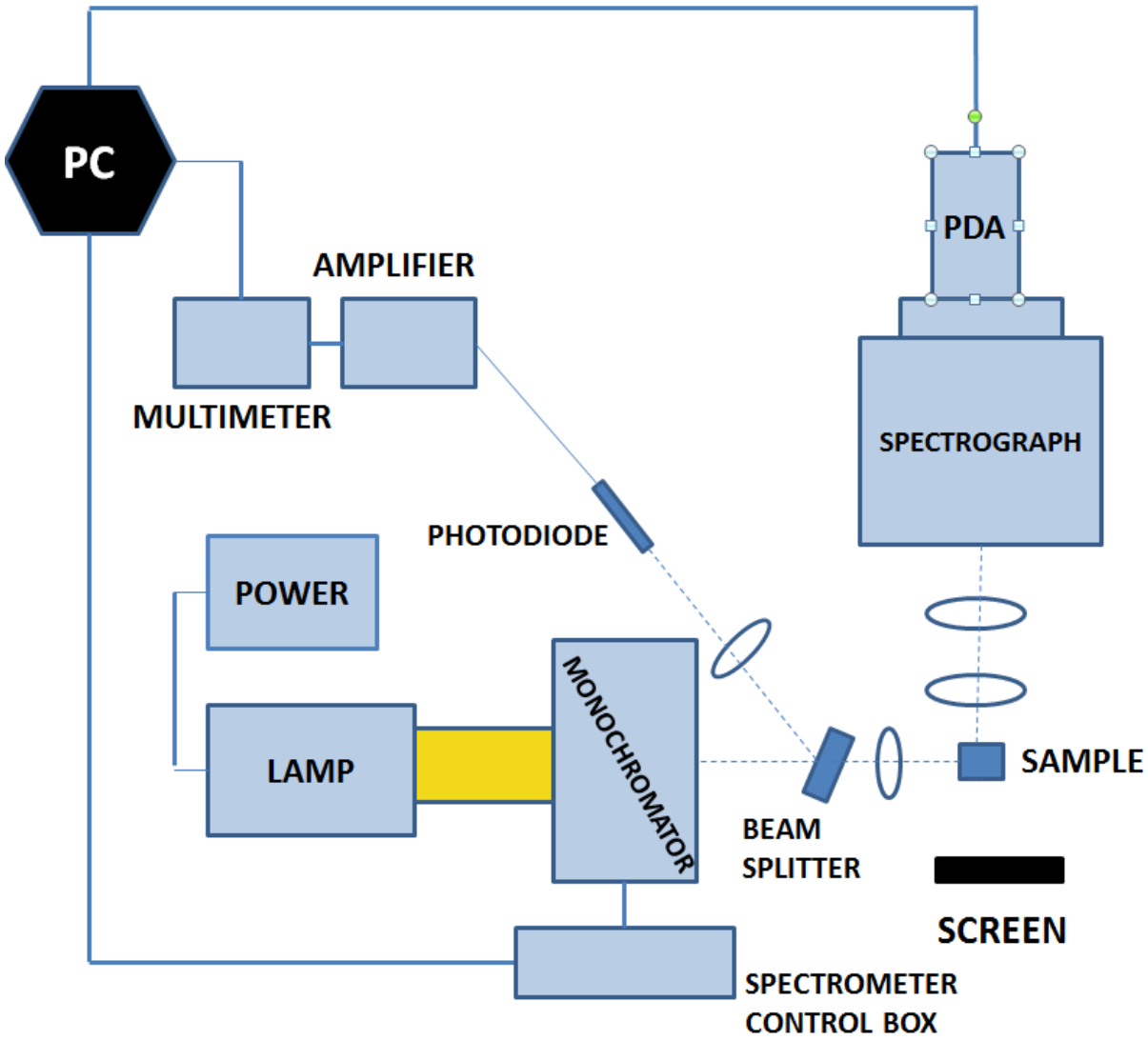

Fig 4.11: Schematic diagram of PLE mapping.

The Photoluminescence was collected at 90º to the excitation beam and focused into a spectrograph with a liquid nitrogen-cooled 512 pixel InGaAs photodiode array which has the range of 900nm-1600nm. We also use a 830nm long pass filter near the detector to remove any scattered signal. The spectral response was normalized using a silicon photodiode and the instrumental response was corrected using a tungsten filament lamp of known emissivity

4.3.3 Atomic Force Microscopy (AFM)

Atomic force microscopy, AFM, is a modern scanning probe microscopic technique for achieving high resolution surface topography images.

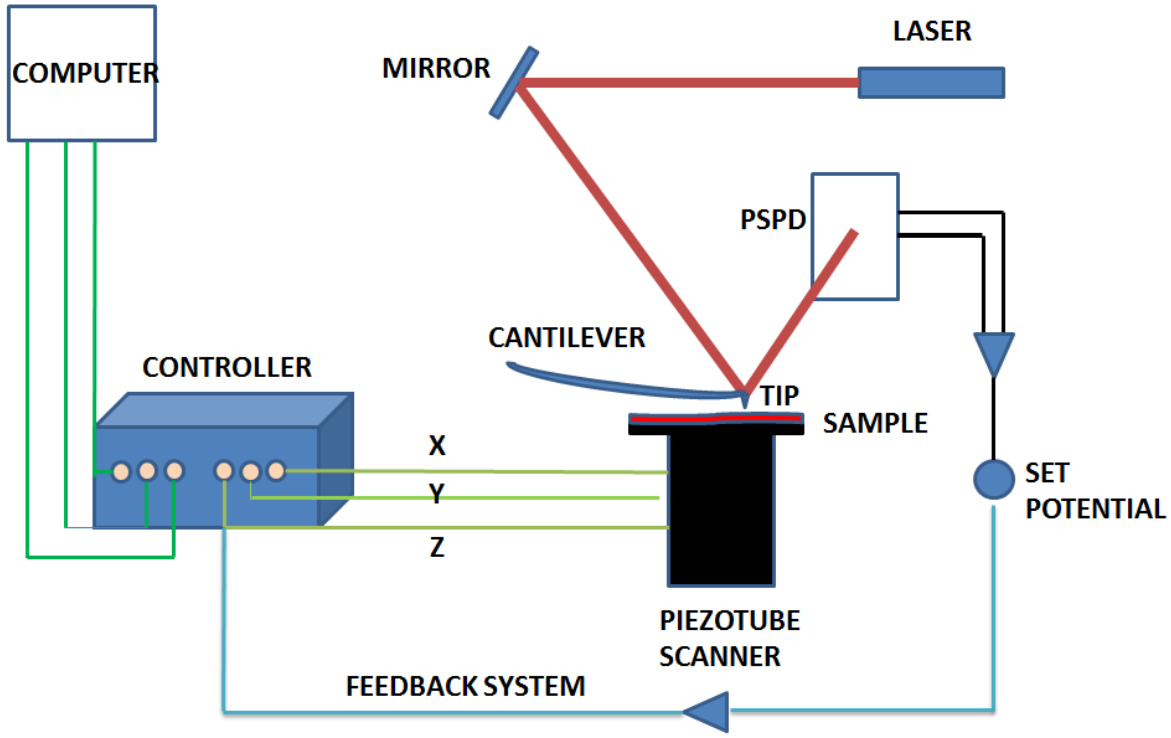

Fig 4.12: Schematic diagram of the basic working principle of AFM.

The sample is examined with a sharp tip, which is 3-15 microns long and generally has a diameter less than 100Å. The tip is present at the free end of the cantilever, which is about 150µm in length. [6, 7] When the tip probes over the surface of the sample (very close), attractive forces between the sample surface and the tip causes the cantilever to deflect towards the surface. Whereas, when the tip comes in contact with the surface, the repulsive forces will make the cantilever to deflect away from the surface. This deflection can be detected with the help of a laser beam. In a non-contact mode, the tip does not come

in contact with the surface area of the sample; however it is made to oscillate just above the sample (typically from 100 to 400 kHz). A laser beam that focussed on the back of the cantilever is reflected back to a 4-quadrant position sensitive photodetector (PSPD). Any minor deflection of the laser beam, caused by the movement of cantilever can be easily detected by this setup. When the tip comes in close contact with any organic material (<10nm distance), van der Waals forces will cause a change in the oscillation amplitude of the tip which can be easily detected by the laser probe system. The system keeps the vibrational amplitude constant with the help of a feedback system by moving the piezoelectric scanner upwards and downwards. The tip is scanned across the surface of the sample using a xy-stage and the changes in van der Waals interactions are detected and used to generate high resolution surface topography images. [8] AFM images for my chapters were taken with Autoprobe M5, in non-contact mode, with a scan rate of 0.2 Hz and 512 sample/lines. All the samples were either spin coated or drop casted on either quartz or Si substrates before AFM measurements.

4.3.4 Raman Spectroscopy and Scanning Electron Microscopy (SEM)

Raman spectra were taken using lasers at 533nm and 633 nm wavelengths, with incident power between 0.5-1 mW. The light was collected from the sample in a back-scattering geometry and recorded using a Jobin-Yvon triple grating spectrometer fitted with a liquid nitrogen cooled silicon CCD detector. SEM is one of the most fundamental tools for material characterisation. When the incident electron beam hits the specimen, wide variety of emissions are produced including backscattered electrons, secondary electrons, Auger electrons, X-rays, visible photons etc. If an incident electron collides with the electron of the sample atom, it will kick the electron out of its orbital shell, leading to the

ionisation of the atom. As the incident electron loses small amount of energy during every collision, multiple collisions are possible. This process continues until the incident electron loses its energy to knock off secondary electrons. Each freed secondary electron has a small kinetic energy and if they are formed close to the surface of the sample, they can easily be collected by the detector. Hence, this secondary electron imaging is much closely related to the topography. For all our experiments, SEM was performed with a Hitachi S-4300 scanning electron microscope system under high vaccum.

4.3.5 Solar cell characterization

The current density–voltage (JV) curves were measured under simulated AM 1.5 sunlight at 100 mWcm-2 irradiance generated by an Abet Class AAB sun 2000 simulator, with the intensity calibrated using an NREL calibrated KG5 filtered Si reference cell. The light intensity was checked at the start of each measurement by a reference diode. JV curves were recorded with a Keithley 2400 sourcemeter integrated with a computer running a Labview program developed in-house. The solar cells were masked with a metal aperture to define the active area ($0.0625 cm^2$), and measured in a light-tight sample holder to minimize any edge effects. In addition, any active materials inbetween the individual cells were removed to ensure precise single cell measurements.

References:

[1]. Matarredona, O. et al. J. Phys. Chem. B 107 13357 (2003).

[2]. T. Schuettfort, H. Snaith, A. Nish, & R. Nicholas, Nanotechnology, 21 025201 (2010).

[3]. J. H. Duckworth, “Spectroscopic quantitative analysis,” in Applied Spectroscopy: A Compact Reference for Practitioners, vol.1, p. 93, Academic Press, (1998).

[4]. N. Grossiord, O. Regev, J. Loos, J. Meuldijk, and C. E. Koning, “Time-dependent study of the exfoliation process of carbon nanotubes in aqueous dispersions by using UV-visible spectroscopy,” Analytical Chemistry, 77 (16) 5135–5139 (2005).

[5]. Nish, A.; Hwang, J. Y.; Doig, J.; Nicholas, R. J. Highly Selective Dispersion of Single-Walled Carbon Nanotubes Using Aromatic Polymers. Nat. Nanotechnol. 2 640–646 (2007).

[6]. Atomic Force Microscopy Investigations into Biology – From Cell to Protein, Edited by Christopher L. Frewin Published by InTech, (2012).

[7]. R. Howland & L. Benatar, A Practical Guide to Scanning Probe Microscopy, Thermomicroscopes (2000).

[8]. Thermomicroscopes, User's Guide to Autoprobe M5 (2000).

Chapter 5

Engineering New Ordered Nanostructures by Binding Single Molecules to Single-Walled Carbon Nanotubes

The work in this chapter has been reproduced in part and adapted with permission from: J. Joseph Sharkey, Samuel D. Stranks, Jian Huang, Jack A. Alexander-Webber, and Robin J. Nicholas. Engineering Nanostructures by Binding Single Molecules to Single-Walled Carbon Nanotubes. ACS Nano, 2014, 8 (12), pp 12748–12754

5.1 Introduction and Background

Single-Walled Carbon Nanotubes (SWNTs) are of great interest for use in Organic and hybrid solar cells due to their combination of attractive properties such as high charge carrier mobilities [1], long-lived charge transport characteristics [2], large aspect ratios, and high tensile strength [3]. Several research groups have recently reported that SWNTs, depending on the dopants, can act as efficient electron accepting materials, [4-6] good absorbers [7], and excellent hole transporting materials, [8,9] demonstrating their promise for use in photovoltaics. Nanotubes have also recently been integrated as hole transporters into high performance perovskite-based solar cells, both as bundled tubes with mixtures of single- and multi-walled tubes [10], and very successfully as individual polymer-wrapped tubes [11].

By wrapping SWNTs with a wide range of π-conjugated polymers, we can efficiently modify both the electronic and mechanical properties of the nanotubes while also dispersing the tubes to avoid unwanted bundling. The binding is mainly due to the

strong π-π interactions which lead to highly efficient nanotube dispersions. [12] The non-covalent nature of the polymer binding to the nanotube is of great advantage because we not only make use of the favorable properties of the polymers but also retain the properties of the nanotubes [13]. Recently, Schuettfort *et al* [14] showed that smaller diameter nanotubes coated with a small bandgap polymer can also form Type-II heterojunctions. In another recent work, Stranks *et al* [15, 16] showed that the binding of two polymers (F8BT and P3HT) can be manipulated in order to produce new nanotube-dual polymer heterostructures which have potential applications in solar cells. Alternatively, Porphyrins can also be used to bind to the nanotubes via π-π stacking [17]. The Porphyrin binding is sufficiently strong to not only cause strain to the nanotubes but also significantly affect their electronic properties [18].

In this chapter, we investigated the binding of nanotubes to Spiro-OMeTAD, which is an amorphous conjugated small, organic material initially used as a hole transporting material in solid state dye-sensitized solar cells [19] but more recently in perovskite-based solar cells, which have achieved power conversion efficiencies exceeding 20% [20-24]. We fabricated a novel dual-shell nanostructure prepared by first wrapping SWNTs with a monolayer of semiconducting polymer (F8BT/P3HT) that forms Type-I / Type-II heterojunctions with the nanotube, and subsequently binding a large number of small molecules (Spiro-OMeTAD) onto the [Polymer-NT] nanohybrids. We use absorption and photoluminescence excitation (PLE) measurements to show that the small molecules induce a mechanical strain on the nanotubes. Further, atomic force (AFM) and scanning electron (SEM) microscopy show that Spiro-OMeTAD binds strongly to Polymer-NT nanohybrids, forming very thick coatings and leading to additional debundling of the tubes.

5.2 Sample Preparation

The polymer-NT (P3HT-NT/F8BT-NT) nanohybrids were prepared as described elsewhere [14, 25, 26]. Briefly, 6mg of P3HT (5mg of F8BT) was dissolved in 10ml of chlorobenzene and homogenized in a sonic bath. Chlorobenzene was used as a solvent because other solvents like toluene, THF and o-xylene gave very poor nanohybrid yields. Then, 3mg of CoMoCAT SG 76 nanotubes were added to the polymer solution and the mixture was treated in an ultrasonic disintegrator for 15min to break the SWNT bundles and hence cause effective interaction between the polymer and individual nanotubes. During sonication, the temperature of the mixture was kept constant at 25ºC. Subsequently, the mixture was centrifuged at 10000g for 8min to remove the unwrapped and bundled nanotubes. To extract the individually wrapped nanotubes and remove the excess polymer, toluene was added to the supernatant in a 1:1 ratio and left for a few hours until the aggregates were visible. Toluene acts as an orthogonal solvent by keeping the polymer (P3HT/F8BT) suspended but causing aggregation of the nanostructures. The nanohybrids were then precipitated out by centrifuging at 16000g for 4 min. The supernatant which contains the excess polymer was discarded and the residue was then redissolved in chlorobenzene. This purification step was repeated three times to remove the unreacted polymer. Finally, highly purified nanohybrids were redissolved in chloroform to any desired concentration. To prepare Spiro-OMeTAD-[polymer-NT] nanohybrids, the desired concentration of Spiro-OMeTAD was added to the polymer-NT solution and tip sonicated for 10 minutes. The resulting solution was then drop-cast on a plasma-etched quartz substrate and placed on a hot plate for about 10 seconds. Note that all sample preparation steps were performed in air.

In summary, we functionalized the SWNTs with either F8BT or P3HT by tip-sonicating appropriate amounts of CoMoCAT SG76 SWNTs and polymer materials using methods described elsewhere [14, 25, 26]. The unwrapped nanotubes and other unwanted material were removed as a residue upon centrifugation of the mixture, while the polymer-dispersed tubes (nanohybrids) were retained in the supernatant. These nanohybrids were subjected to a simple solution processing technique in order to remove the excess unused polymers in solution [25]. Various concentrations of Spiro-OMeTAD were then added to these 100% pure (excess polymer removed) polymer-NT solutions and the material was drop-cast on to plasma-etched quartz substrates

5.3 Absorption Spectroscopy

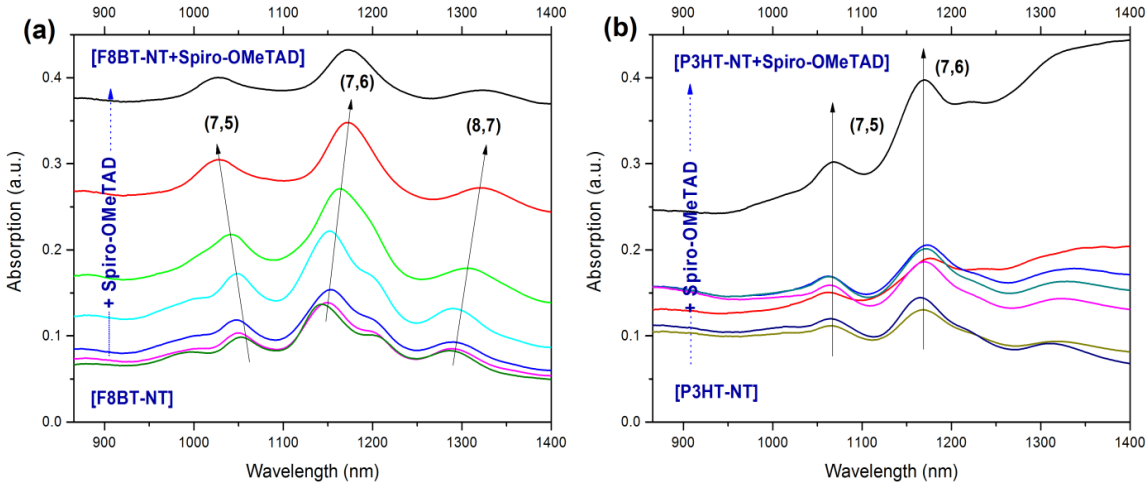

Figure 5.1: Absorption spectra of nanohybrid thin films with increasing concentration of Spiro-O-MeTAD added to precursor solutions of (a) [F8BT-NT] and (b) [P3HT-NT].

Absorption measurements for [F8BT-NT] films in the NIR region are shown in Figure 5.1a. They reveal three distinctive peaks that are attributed to the first van Hove bandgap E_{11} at 1053, 1145 and 1281nm corresponding to (7, 5), (7, 6) and (8, 7) chirality

tubes with diameters 0.82, 0.89 and 1.03nm, respectively [27]. These peaks are red-shifted relative to the [SDBS-NT] samples due to the dielectric screening effect on the SWNT caused by the F8BT [14]. When an increasing concentration of Spiro-OMeTAD is added to the F8BT-coated nanotubes, the absorption peaks are either red- or blue-shifted, depending on the nanotube family [18]. In addition, these shifts are quite large indicating a strong physical interaction between F8BT-NT and Spiro-O-MeTAD. Our research group has previously shown that once F8BT is bound to SWNT, it allows both excess F8BT and P3HT to wrap onto the nanohybrids [15]. Similarly, F8BT-NT nanohybrids show strong affinity towards Spiro-O-MeTAD. When the concentration of Spiro-O-MeTAD is increased, the amount of Spiro-O-MeTAD deposited on the F8BT-NT keeps increasing which can clearly be seen from the huge peak shifts in the absorption spectroscopy. We speculate that these numerous small molecules bind all over F8BT that wraps the NT and on the parts of the NT that are not coated by F8BT causing huge strain on the tubes. By contrast, Fig. 5.1(b) shows that no significant shifts are observed when Spiro-OMeTAD is added to [P3HT-NT] nanohybrids indicating that there is very less physical interaction between P3HT-NT and Spiro-O-MeTAD. P3HT chains are highly planarised and extended on the nanotubes and they are not strongly coupled to other chains. This is because the pi-pi interactions of the chains in a monolayer coating are predominantly with the NT surfaces on which they are bound.

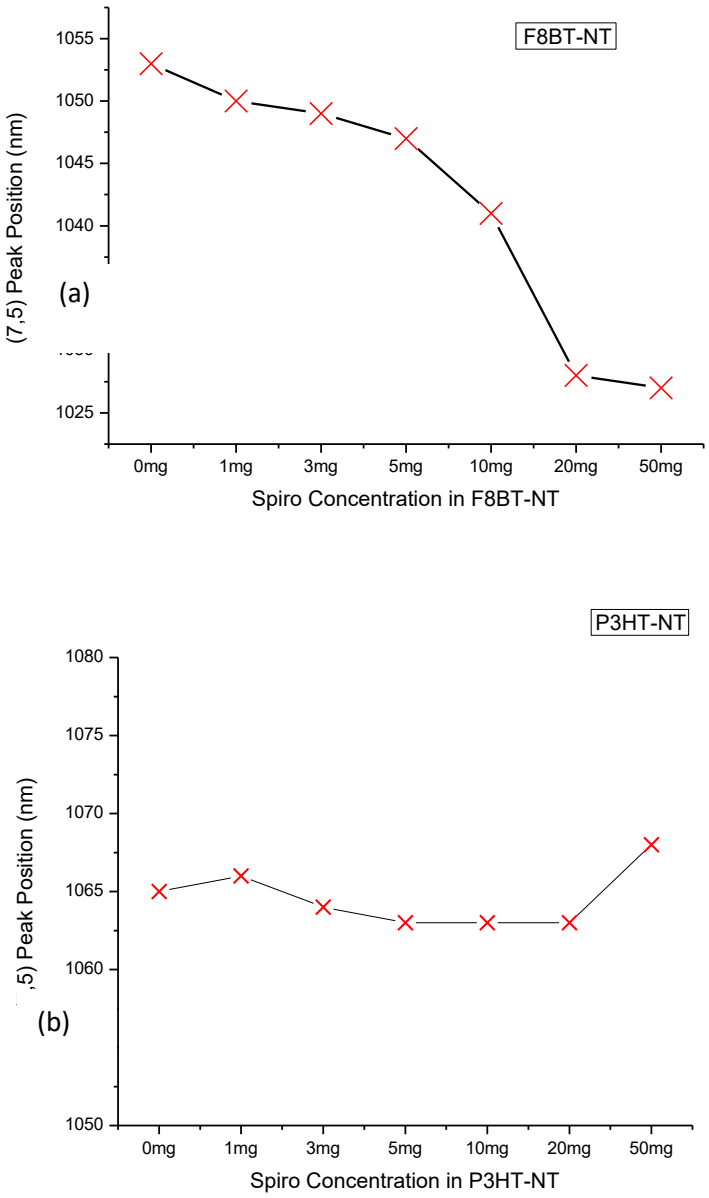

Figure 5.2: Peak position of the (7,5) nanotube E_{11} transitions in thin films when adding increasing spiro concentrations to the precursors solutions of (a) [F8BT-NT] and (b) [P3HT-NT].

Fig 5.2 (a) clearly shows a progressive blue shift in the peak position of the (7,5) nanotube species with respect to the increase in spiro concentration in F8BT-NT films, whereas there is no significant shift in the peak position of (7,5) nanotube species with respect to the increase in spiro concentration in P3HT-NT films, as seen in [Fig 5.2 (b)].

The family-dependent shifts suggest strain-induced changes in the band structure of individual single-walled carbon nanotubes, as has been observed earlier for nanotubes which have been strained by freezing [28], or wrapping with polymers or large molecules [18, 29]. The energy shifts of the E_{11} bands depend on both the chiral indices and the magnitude of the strain in the radial and azimuthal directions [30] so that it is possible to deduce the separate strain components by measuring nanotubes with different chiral indices.

5.4 Photoluminescence Excitation Spectroscopy

Increased spectral resolution for tubes with different chiral indices can be obtained by resonant excitation into the E_{22} states using photoluminescence excitation (PLE) spectroscopy, which is a powerful tool to investigate the degree of bundling in nanotubes, assign nanotube species, and determine any associated peak shifts [31]. Figures 5.4a and 5.4b show PLE false color contour maps for the [F8BT-NT] and [F8BT-NT]-Spiro-OMeTAD samples, respectively. The excitation range of 600-800 nm shows E_{11} emission peaks resulting from direct excitation into the E_{22} transitions of six different semiconducting species [(7, 5), (7, 6), (8, 4), (8, 6), (8, 7) and (9, 4)] of SWNTs, while excitation around 480nm shows E_{11} emission resulting from energy transfer from the polymer to all the nanotube species following absorption in F8BT [14, 31]. In the [F8BT-NT]-Spiro-OMeTAD films, the emission peaks of three semiconducting nanotube species belonging to the family, q = +1(introduced in Chapter 2), namely (7, 6), (8, 4) and (8, 7), are progressively red-shifted with the increasing concentration of Spiro-OMeTAD , whereas the emission peaks of three other semiconducting species that belong to the family q = -1, namely (7,5) (8,6) and (9,4) nanotubes, are blue-shifted (see Figure 5.3),. This

phenomenon is attributed to the very strong binding of Spiro-OMeTAD to the nanohybrids causing a very large mechanical strain in the SWNTs [17].

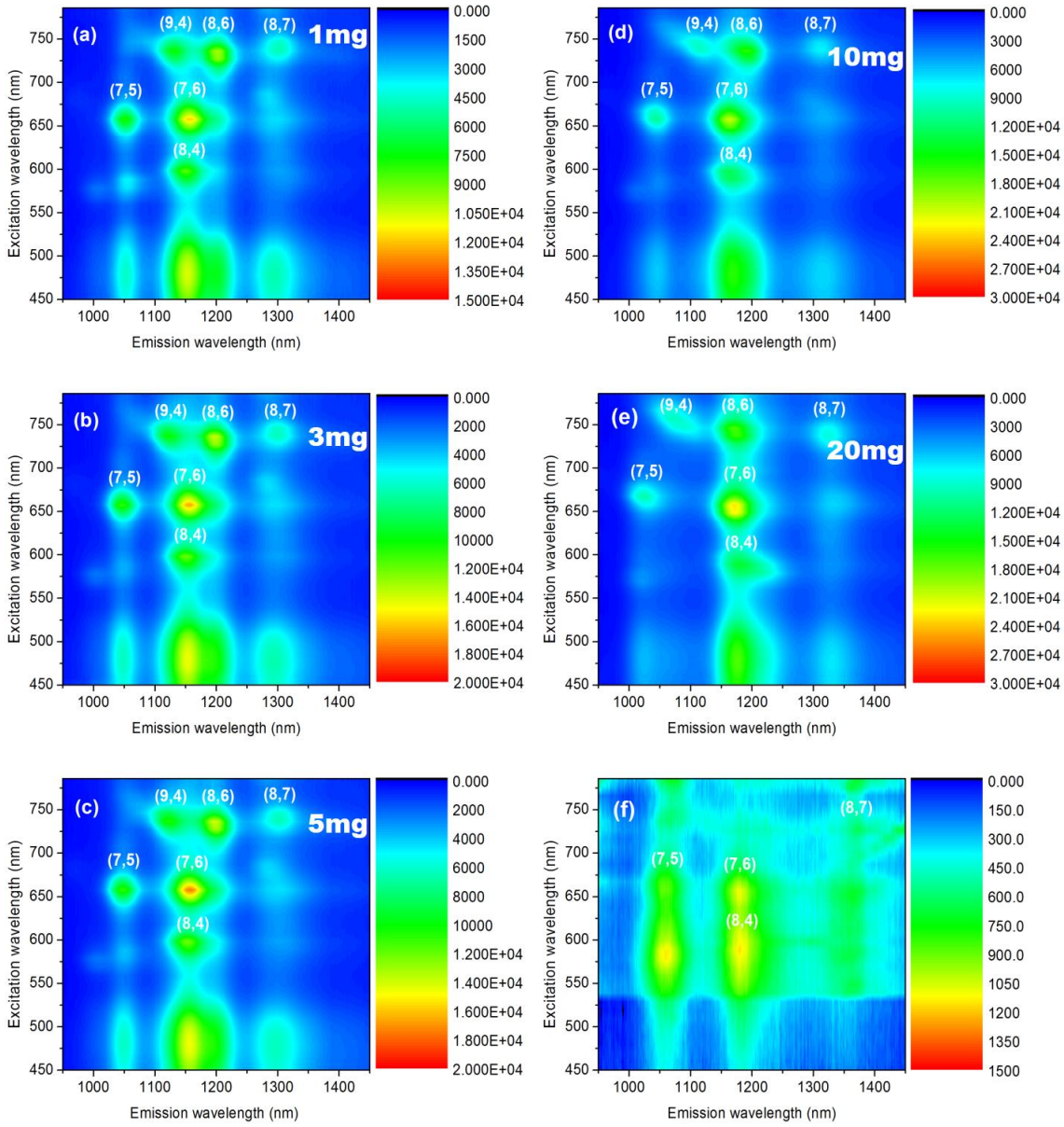

Figure 5.3: PLE maps of the nanohybrids films (on quartz substrates) comprised of (a) [F8BT-NT+1mg Spiro-O-MeTAD], (b) [F8BT-NT] + 3mg Spiro-O-MeTAD, (c) [F8BT-NT] + 5mg Spiro-O-MeTAD (d) [F8BT-NT] + 10mg Spiro-O-MeTAD (e) [F8BT-NT] + 20mg Spiro-O-MeTAD (f) [P3HT-NT].

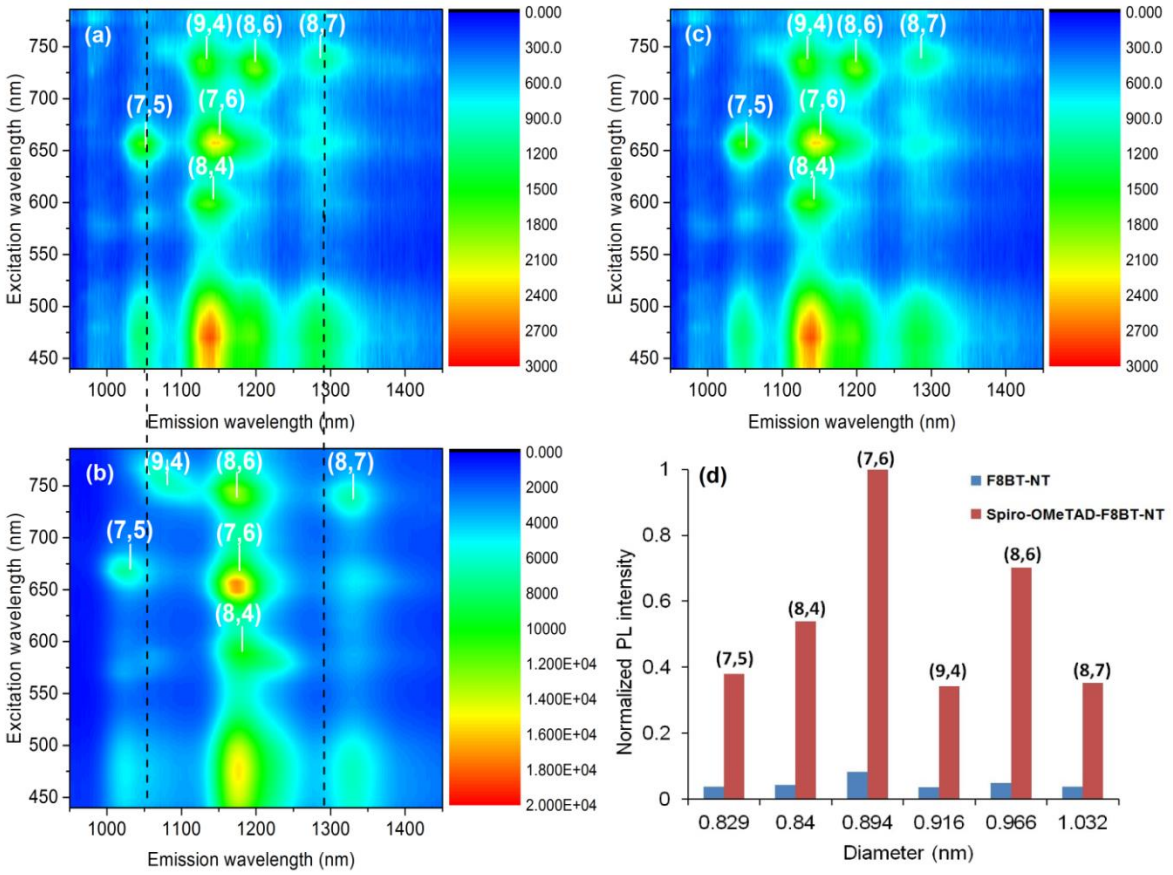

Figure 5.4: PLE maps of the purified nanohybrid films (on a quartz substrate) comprised of (a) [F8BT-NT], (b) [F8BT-NT] + 50mg Spiro-O-MeTAD, and (c) [P3HT-NT] + 50mg Spiro-O-MeTAD. The resonant nanotube species transitions are labelled in white. Nanotube species were assigned from Weisman and Bachilo [27], red-shifted by 25 meV for F8BT and 50meV for P3HT [13]. (d) Comparison of PL intensities of various SWNT species by exciting them at their respective wavelengths in both [F8BT-NT] and [F8BT-NT]+50mg Spiro-O-MeTAD samples.

In addition, the intensity of the nanotube photoluminescence from the Spiro-O-MeTAD-[F8BT-NT] nanohybrid increases by ~1 order of magnitude compared to the unwrapped [F8BT-NT] in films (Figure 5.4d). We suggest that this is caused by improved

debundling of the agglomerated tubes due to the very strong binding by Spiro-O-MeTAD, which leads to the formation of large, well separated nanohybrids as seen in the microscopy reported below. The thick wrapping layer which we will show is formed by the Spiro-OMeTAD will also act to isolate the nanotubes from each other and from disorder present on the substrate. It is also possible that the electronic properties of the Spiro-O-MeTAD will play a role as the energy levels shown in Fig. 5.7 suggest that it will provide additional electron confinement to reduce any charge loss when excitation is directly into the nanotubes. Direct excitation into the F8BT may be less effective however due to hole transfer into the Spiro-O-MeTAD, and it is noticeable that the F8BT energy transfer peaks around 480nm become progressively less strong relative to the direct E_{22} excitation.

By contrast, in the case of the P3HT-NT and P3HT-NT-Spiro-OMeTAD samples no significant peak shifts are observed and there is no change in the PL intensity (Fig 5.3(f) and Fig. 5.4 (c) , leading us to the conclusion that the nanohybrids are still bundled and there is less physical interaction between Spiro-OMeTAD and [P3HT-NT] compared to [F8BT-NT] nanohybids.

5.5 Strain Calculation

Strain-induced changes in the band gaps of carbon nanotubes are well understood, giving a change in band gap (ΔE_{strain}) due to mechanical strain of [18, 33-35]

$$\Delta E_{strain} = \left(\frac{2t_0 a_{c-c}}{d}\right)(\varepsilon_\perp - \nu\varepsilon_\parallel) + 3qt_0\left[\left((1+\nu)\varepsilon_\parallel \cos 3\theta + \varepsilon_\perp \sin 3\theta\right)\right] \quad \textbf{[5.1]}$$

where t_o is the carbon-carbon transfer integral, a_{c-c} is its corresponding bond length, d is the diameter of the carbon nanotube. ν is the Poisson ratio, θ is the tube chiral angle, q is the nanotube species (±1). $\varepsilon_{\parallel}$ and $\varepsilon_\perp$ are the uniaxial and torsional strain components caused

by the binding of the Spiro-OMeTAD to the [F8BT-NT] nanohybrids. The parameters used in our calculations are t_o = 3.0 eV, a $_{c\text{-}c}$ = 1.432Å, ν = 0.2 and the average diameter of the nanotube is taken as d =0.9 nm [18]. Fits to Eq. 1 are shown in Figure 5.5 and yield values for $\varepsilon_{\parallel}$(uniaxial strain) and $\varepsilon_{\perp}$ (torsional strain) of 0.45% and 0.25%, respectively, which are significantly larger than the values observed previously from temperature- or pressure-induced strain effects [28] or from the binding of porphyrin units ($\varepsilon_{\parallel}$~0.2% and $\varepsilon_{\perp}$ ~0.1%) [18].

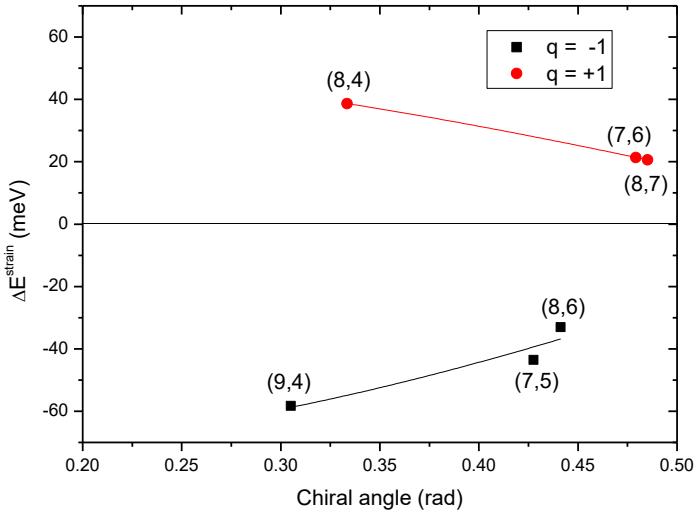

Figure 5.5: Strain components for [F8BT-NT] + 50mg Spiro-O-MeTAD composites. Curves show fits to the data using the Yang and Han [18, 30] model for small strain with the constant term in Eq (5.1).

5.6 Atomic Force Microscopy

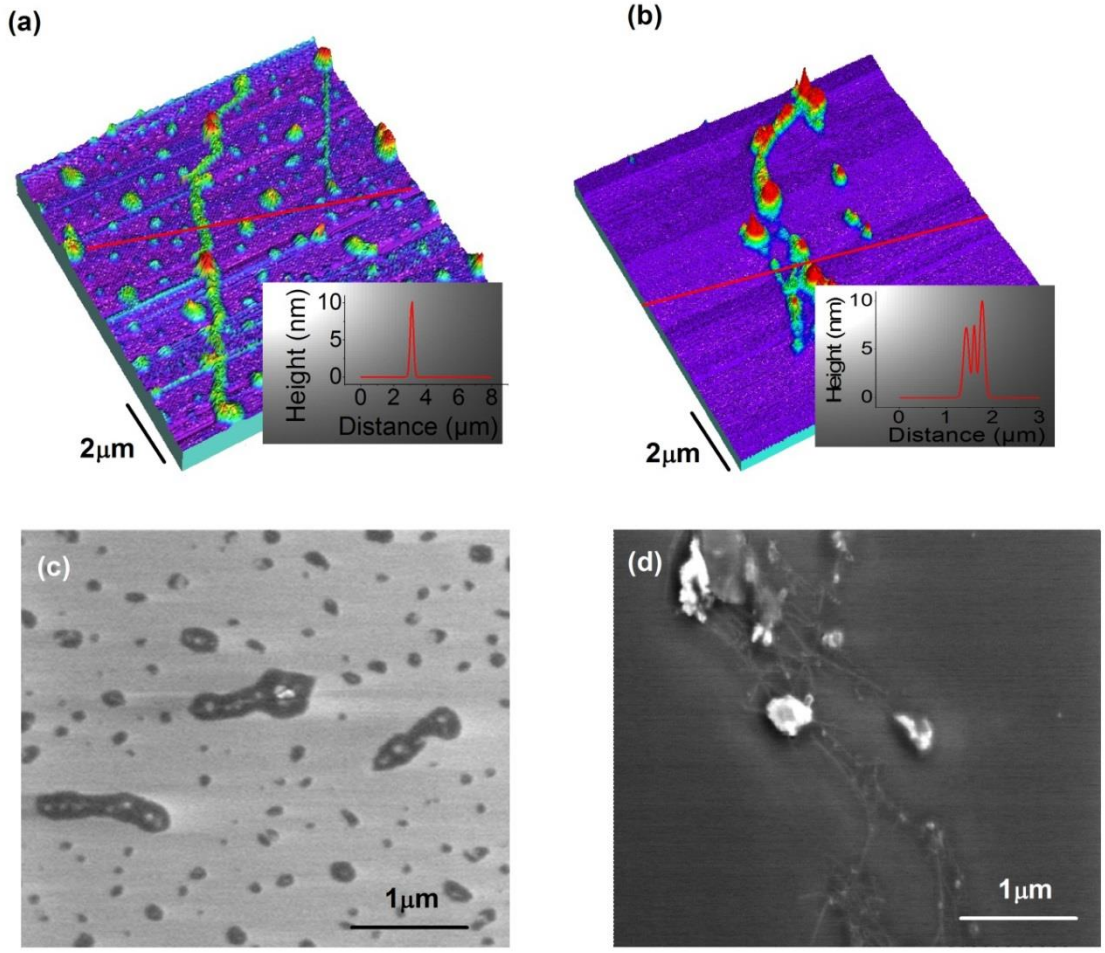

Figure 5.6: False colour 3D AFM images of (a) [F8BT-NT] + 50mg Spiro-O-MeTAD (b) [P3HT-NT] + 50 mg Spiro-O-MeTAD nanohybrid films casted by diluting the original solution to 1/1000th of the initial concentration, with corresponding SEM images shown in (c) and (d), respectively.

In order to investigate the morphology of the nanohybrids, thin films of [SWNT-Polymer] and [SWNT-Polymer]-Spiro-OMeTAD nano hybrid structures were also drop-cast onto silicon substrates from diluted nanohybrid solutions. The height profiles of [F8BT-NT] and [P3HT-NT] films, along the cross section, show a typical height of 2-3 nm,

corresponding to the height of a SWNT bound by either a monolayer or bilayer of polymer, separated by twice the van der Waals radius of carbon [15, 25]. A three dimensional AFM image of [F8BT-NT]-Spiro-OMeTAD film is shown in Figure 5.6 (a), revealing a uniform and thick coating of Spiro-OMeTAD over the entire length of the nanotubes, which prevents the formation of nanotube bundles. These nanohybrids are widely dispersed over the entire surface of the film. The height analysis shows that the diameter of these nanohybrids varies from 8 to 10 nm, indicating the formation of very thick coatings along the entire length of the nanotube. Typical nanotube lengths are between 0.5-2 μm long with a few longer tubes (8 μm), as shown in figure 5.6 (a). Figure 5.6 (b) shows an AFM image from the [P3HT-NT]-Spiro-OMeTAD films. This shows that the nanohybrids are more bundled with a typical height of 5-6 nm. In addition, we observe the formation of large crystals with a typical height of 10-15nm which are speculated to be due to the nucleation of Spiro-OMeTAD by the P3HT.

5.7 Scanning Electron Microscopy Images

SEM images for the same samples were also taken. Figure 5.6 (c) shows the SEM of a [F8BT-NT]-Spiro-OMeTAD film. The black spherical structures are speculated to be Spiro-OMeTAD and the widely dispersed individual tubular structures on the silicon surface correspond to the [F8BT-NT]-Spiro-OMeTAD nanohybrids. The size of the [F8BT-NT]-Spiro-OMeTAD nanohybrids in this view is even larger with some structures up to 100nm across in plan view. These widely dispersed nanohybrids are speculated to be the reason for the large improvement in PL intensity. The SEM image of [P3HT-NT]-Spiro-OMeTAD is shown in figure 5.6d. As seen in the AFM analysis, the bundled P3HT-

wrapped nanotubes are clearly visible, along with the large nucleated crystals of Spiro-OMeTAD.

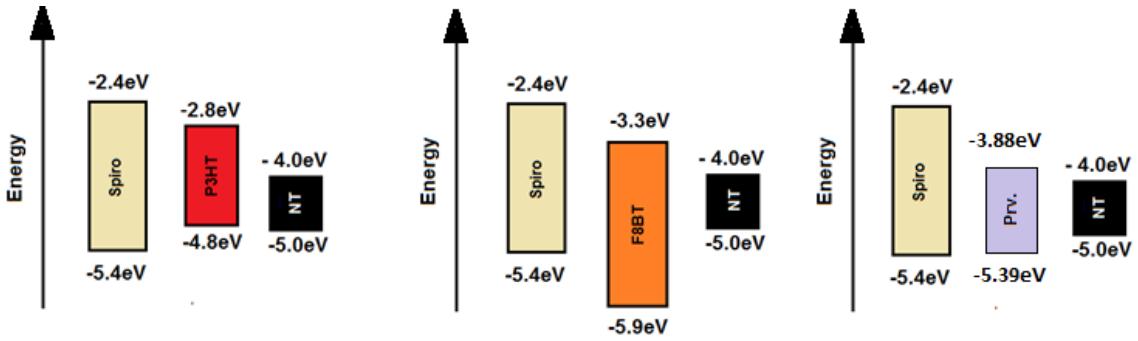

Figure 5.7: Schematic energy level diagram of nanohybrids consisting of P3HT/F8BT wrapped around the nanotube with Spiro-O-MeTAD embedded on them. Energy level of Perovskite is also shown for reference (Energies are given with respect to vacuum) [4, 14].

5.8 Applications

Recently, Zhen Li *et al* [10] reported the use of SWNT/Spiro-OMeTAD composites as effective hole transporting materials for perovskite solar cells. Incorporation of these bundled composites improved the charge separation and collection in the solar cell and thereby doubled the power conversion efficiency from 5.14% to 9.90%. Our research group has recently shown that a hole transporting layer consisting of P3HT wrapped SWNT with Spiro-O-MeTAD composite can deliver stabilized power conversion efficiencies of exceeding 18% in perovskite solar cells, along with greatly enhanced stability to moisture and thermal effects [11, 36]. It is likely that the more controlled and designed structures with unbundled tubes presented here will allow further improvements. Our novel polymer/SWNT/Spiro-OMeTAD nanohybrids have complementary band alignments (Figure 5.7), which may be useful in optimizing charge transport or separation in OPV devices or in confining photoexcitations (charges or excitons) for improved light emission

devices. The work also opens up the possibility to exploit a wide range of other similar small molecules that could bind to the polymer-SWNT hybrids to allow designed engineering of new nanohybrids.

5.9 Summary

In conclusion, a novel core-dual shell nanostructure prepared by wrapping SWNTs with a thin monolayer of F8BT and consequently binding Spiro-OMeTAD onto the [F8BT-NT] nanohybrids has been engineered and analyzed in detail. Absorption and PLE measurements show that the strong binding to the Spiro-OMeTAD results in large strains along both the uniaxial axis (0.45%) and the circumference (0.25%) of the nanotubes. AFM and SEM data show that Spiro-OMeTAD binds strongly to the entire surface of the nanotube forming very thick coatings and the nanohybrids can be widely dispersed onto film surfaces. This strong interaction leads to a significant improvement in PL emission intensity which we associate with the debundling of the nanotubes combined with the protective coating provided by the Spiro-OMeTAD coating. These novel nanohybrids have potential future applications in high-efficiency, cost-effective carbon nanotube-based organic and hybrid optoelectronics.

References

[1]. Reich, S.; Thomsen, C.; Maultzsch, J. Carbon Nanotubes: Basic Concepts and Physical Properties. Wiley-VCH, (2004).

[2]. D'Souza, F.; Sandanayaka, A. S. D.; Ito, O. SWNT-Based. J. Phys. Chem. Lett. 1 2586-2593 (2010).

[3]. Coleman, J. N.; Cadek, M.; Ryan, K. P.; Fonseca, A.; Nagy, J. B.; Blau, W. J.; Ferreira, M. S. Polymer 47 8556-8561 (2006).

[4]. Stranks, S. D.; Weisspfennig, C.; Parkinson, P.; Johnston, M. B.; Herz, L. M.; Nicholas, R. J. Nano Lett. 11 66-72 (2011).

[5]. Shunichi, F. ECS Journal of Solid State Science and Technology, 6 (6) M3055-M3061 (2017).

[6]. Ren, S.; Bernardi, M.; Lunt, R. R.; Bulovic, V.; Grossman, J. C.; Gradečak, S. Nano Lett. 11 5316-5321 (2011).

[7]. Bindl, D. J.; Wu, M.-Y.; Prehn, F. C.; Arnold, M. S. Nano Lett. 11 455-460 (2010).

[8]. Dabera, G. D. M. R.; Jayawardena, K. D. G. I.; Prabhath, M. R. R.; Yahya, I.; Tan, Y. Y.; Nismy, N. A.; Shiozawa, H.; Sauer, M.; Ruiz-Soria, G.; Ayala, P.; et al. ACS Nano 7 556-565 (2012).

[9]. Dissanayake, N. M.; Zhong, Z. Nano Lett. 11 286-290 (2010).

[10]. Li, Z.; Kulkarni, S. A.; Boix, P. P.; Shi, E.; Cao, A.; Fu, K.; Batabyal, S. K.; Zhang, J.; Xiong, Q.; Wong, L. H.; et al. ACS Nano 8 6797-6804 (2014).

[11]. Habisreutinger, S. N.; Leijtens, T.; Eperon, G. E.; Stranks, S. D.; Nicholas, R. J.; Snaith, H. J. Nano Lett. 14 5561-5568 (2014).

[12]. Habisreutinger, S. N.; Leijtens, T.; Eperon, G. E.; Stranks, S. D.; Nicholas, R. J.; Snaith, H. J. J. Phys. Chem. Lett. 5 4207-4212 (2014).

[13]. O'Connell, M. J.; Boul, P.; Ericson, L. M.; Huffman, C.; Wang, Y.; Haroz, E.; Kuper, C.; Tour, J.; Ausman, K. D.; Smalley, R. E. Chem. Phys. Lett. 342 265-271 (2001).

[14]. Schuettfort, T.; Nish, A.; Nicholas, R. J. Nano Lett. 9 3871-3876 (2009).

[15]. Stranks, S. D.; Yong, C.-K.; Alexander-Webber, J. A.; Weisspfennig, C.; Johnston, M. B.; Herz, L. M.; Nicholas, R. J. ACS Nano 6 6058-6066 (2012).

[16]. Stranks, S. D.; Habisreutinger, S. N.; Dirks, B.; Nicholas, R. J. Adv. Mater. 25 4365-4371 (2013).

[17]. Sprafke, J. K.; Stranks, S. D.; Warner, J. H.; Nicholas, R. J.; Anderson, H. L. Angew. Chem. Int. Edit. 50 2313-2316 (2011).

[18]. Stranks, S. D.; Sprafke, J. K.; Anderson, H. L.; Nicholas, R. J. ACS Nano 5 2307-2315 (2011).

[19]. Bach, U.; Lupo, D.; Comte, P.; Moser, J. E.; Weissortel, F.; Salbeck, J.; Spreitzer, H.; Gratzel,. Nature 395 583-585 (1998).

[20]. Cho, K. T. et al. Energy Environ. Sci. 10 621–627 (2017).

[21]. NREL. Efficiency chart. https://www.nrel.gov/pv/assets/images/efficiency-chart-20180716.jpg (2018).

[22]. Yang, W. S. et al. Science 356 1376–1379 (2017).

[23]. Zhou, H.; Chen, Q.; Li, G.; Luo, S.; Song, T.-b.; Duan, H.-S.; Hong, Z.; You, J.; Liu, Y.; Yang, Y. Science 345 542-546 (2014).

[24]. Burschka, J.; Pellet, N.; Moon, S. J.; Humphry-Baker, R.; Gao, P.; Nazeeruddin, M. K.; Gratzel, M. Nature 499 316-319 (2013).

[25]. Schuettfort, T.; Snaith, H. J.; Nish, A.; Nicholas, R. J. Nanotechnology 21 025201 (2010).

[26]. Nish, A.; Hwang, J.-Y.; Doig, J.; Nicholas, R. J.. Nat. Nanotechnol. 2 640-646 (2007).

[27]. Bachilo, S. M.; Strano, M. S.; Kittrell, C.; Hauge, R. H.; Smalley, R. E.; 298 2361-2366 (2002).

[28]. Li, L.-J.; Nicholas, R. J.; Deacon, R. S.; Shields, P. A. Phys. Rev. Lett. 93 156104 (2004).

[29]. Leeuw, T. K.; Tsyboulski, D. A.; Nikolaev, P. N.; Bachilo, S. M.; Arepalli, S.; Nano Lett. 8 826-831 (2008).

[30]. Yang, L.; Anantram, M. P.; Han, J.; Lu, J. P. Phys. Rev. B 60 13874-13878 (1999).

[31]. Heeg, S.; Malić, E.; Casiraghi, C.; Reich, S.. Phys. Status Solidi B 246 2740-2743 (2009).

[32]. Hwang, J.-Y.; Nish, A.; Doig, J.; Douven, S.; Chen, C.-W.; Chen, L.-C.; Nicholas, R. J.. J. Am. Chem. Soc. 130 3543-3553 (2008).

[33]. Valavala, P. K.; Banyai, D.; Seel, M.; Pati, R.. Phys. Rev. B 78 235430 (2008).

[34]. Yang, L.; Han, J. Phys. Rev. Lett. 85 154-157 (2000).

[35]. Gartstein, Y. N.; Zakhidov, A. A.; Baughman, R. H. Phys. Rev. B 68 115415 (2003).

[36]. SN Habisreutinger, B Wenger, HJ Snaith, RJ Nicholas. Dopant-Free Planar n-i-p Perovskite Solar Cells with Steady-State Efficiencies Exceeding 18%. ACS Energy Letters 2 622-628 (2017).

Chapter 6

Preparation of Mono-Chiral SWNTs Using a Simple Solution Processing Technique.

6.1 Introduction and Background

Over the past two decades, single-walled carbon nanotubes (SWNTs) have attracted much attention due to their extraordinary physical and electronic properties [1, 2]. The presence of different chiralities (n,m) has always been a barrier since it does not give the opportunity to access the complete potential of the individual tubes. Several research groups have tried various techniques like gel chromatography, [3] density gradient centrifugation, [4-6] DNA wrapping, [7, 8, 9] and polymer wrapping [10-13, 25] to individualize the SWNTs. However, most of these methods still have difficulties in achieving highly pure mono-chiral SWNTs and are unfavourable due to high cost (DNA), limited scalability (DGU), time consuming multi-step processes (DNA, DGU and ATP) or often require specialized equipment [31]. To achieve efficient dispersion and controlled selectivity, different types of conjugated copolymers were used. Among them, PFO and PFO-Bpy are the two best co-polymers which show ~90% selectivity towards (7,5) tubes and ~96% selectivity towards (6,5) tubes [32]. To our knowledge, this is the highest purity obtained for a mono-chiral smaller diameter nanotube by a solution processing technique. Arnold *et al*., have also shown that incorporation of these mono-chiral, smaller diameter, SWNTs improves the efficiency of thin film photovoltaic devices [14, 15]. PFO and its derivative have low mobility and large bandgap hence they are not suitable candidates for

OSCs. Hence, our goal was to improve the selectivity of a smaller diameter SWNTs with the help of a low bandgap polymer that has the potential to be used in OSC applications.

In this study, different fully conjugated polytriaryl amine based polymers with increasing side chain functionalities (C6, C8, C10 and C12) were synthesised via Suzuki coupling polymerization [16,17] in Taiwan by our collaborators [Fig 6.1]. They are amorphous in nature and were quite soluble in organic solvents like toluene, chlorobenzene, chloroform and THF. Due to their high hole mobilities and their ability to form radical cations easily, polytriaryl amine based polymers are extensively used in LED's, electrochromism and polymer electronic memories [18-23]. Liaw *et al* have recently shown that a similar type of polymer gives some selectivity to (6,5) tubes but did not study the effects of side chain length [32]. In this report, we investigated the properties of these polymer wrapped single walled carbon nanotubes using UV-vis-NIR absorption spectra, photoluminescence excitation mapping, Raman spectroscopy, AFM and SEM images. We show that the newly synthesised polymer was able to wrap around individual, smaller diameter, SWNTs and wrapping of the polymers can be chirality dependant. The affinity of C8 polymer towards the (6, 5) tubes helps in the selective enrichment of those tubes. Hence, we are able to wrap highly pure mono-chiral SWNTs using a simple solution processing technique.

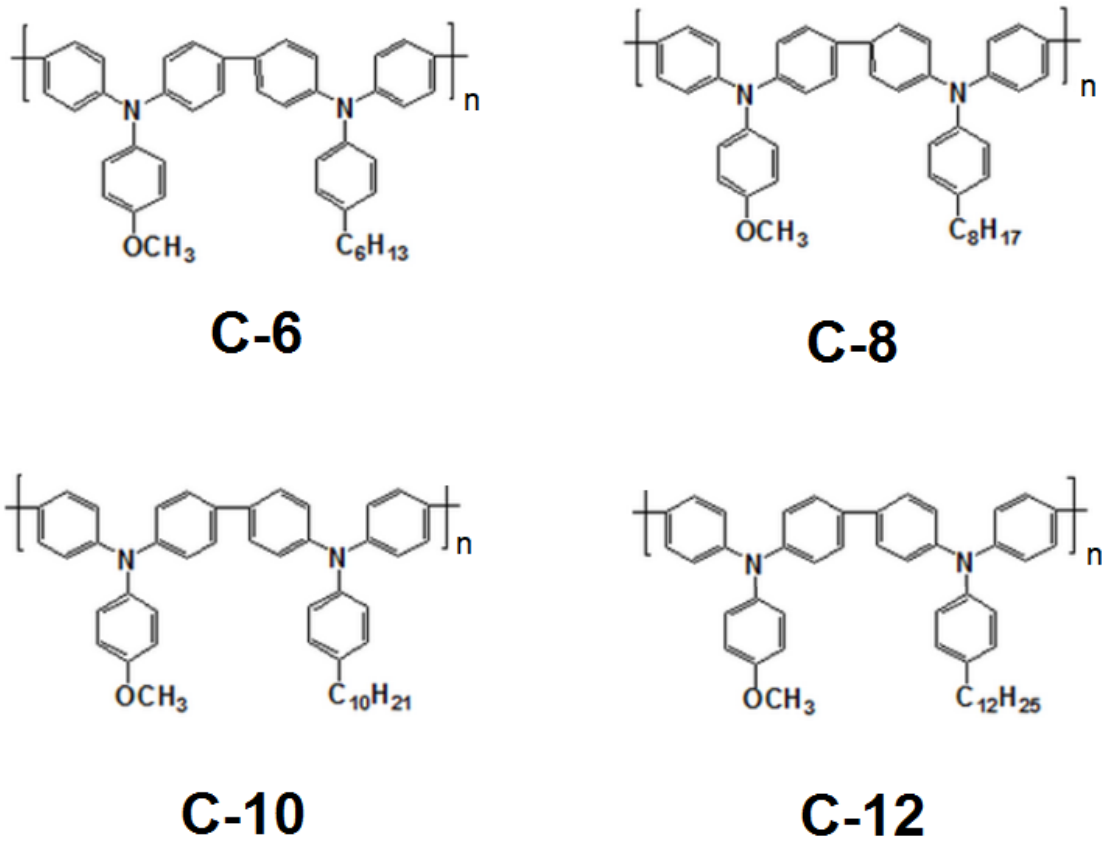

Figure 6.1: Structure of Polymers C6, C8. C10 and C12.

6.2 Sample Preparation

CoMoCAT SG 65i SWNTs with smaller diameter (0.7-1.1 nm) and purity > 90% were purchased from Sigma-Aldrich. SDBS-65i distributions were prepared by dispersing SG65i nanotubes with SDBS in D_2O. Different SWNT starting materials like HIPCO, SG76 AND CG100 were also directly dispersed with SDBS and semiconducting polymers like PFO, C6, C8, C10 and C12 in o-xylene using the method developed by Nish *et al* [10] but we optimised this method using o-xylene to increase the yield of our nanohybrids. Briefly, 6mg of C8 polymer was dissolved in 10ml of o-xylene and homogenized in a sonic bath. Then, 3mg of CoMoCAT SG 65i nanotubes were added to the polymer solution and

the mixture was treated in an ultrasonic disintegrator for 15min to break the SWNT bundles and hence, allow effective interaction between the polymer and individual nanotubes. During sonication, the temperature of the mixture was kept constant at 25ºC. Subsequently, the mixture was centrifuged at 10000g for 8min to remove the unwrapped and bundled nanotubes. In order to remove the excess polymer, the supernatant solution was introduced into a rotary evaporator. This induces aggregation of the tubes followed by ultra-centrifugation for 4 minutes at 16000g . The precipitate was then dissolved in a desired solvent and this step was repeated several times. This nano-hybrid solution which contains the individual tubes was used for spectroscopic characterization. Note that all sample preparation steps were performed in air.

6.3 Absorption Spectroscopy

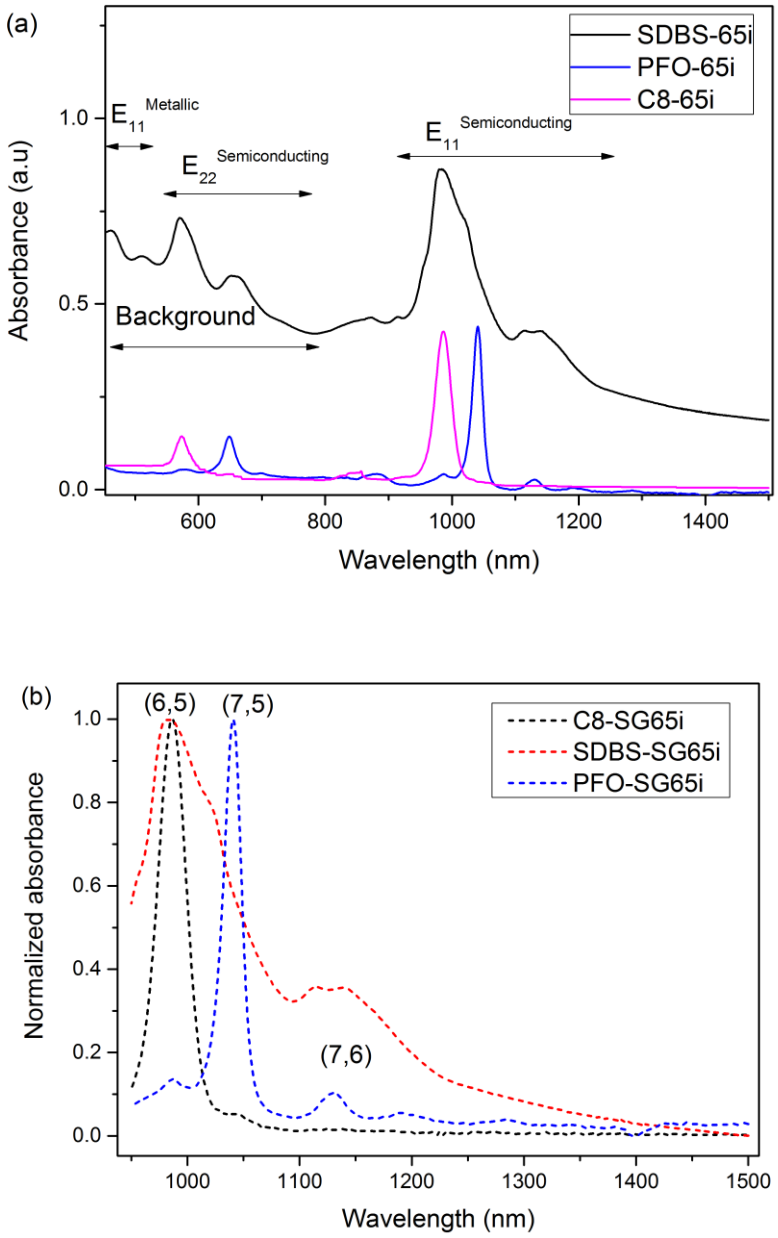

Figure 6.2: a) Absorption spectrum of SG65i tubes with SDBS showing a huge background indicating the presence of metallic tubes. b) Normalized Absorption spectra of C8-SG65i and PFO-SG65i compared with SDBS-SG65i showing the monochiral wrapping of (6,5) and (7,5) tubes, respectively.

Fig 6.2 a) shows an absorption spectrum of the dispersed SDBS-SG65i distribution [red line]. The semiconducting E_{11}^{S} transitions are seen in the NIR range [900-1500nm] and the semiconducting E_{22}^{S} transitions in the visible region [550-750nm]. The wide background in the [SDBS-SG65i] sample could be due to several factors including light scattering effects, carbon impurities contributing to a broad π-π plasmon, nanotube defects and is primarily attributed to the presence of metallic species. The SDBS surfactant dispersion is non-selective and shows that the ratio of (6,5) to (7,5) tubes in the SG65i starting material is 2:1. Fig 6.2 a) also shows the absorption spectra of C8-SG65i nanohybrids. The wide background is completely absent indicating the elimination of metallic tubes [450-550nm] and any other carbonaceous materials from the starting material [SG65i tubes], resulting in highly selective semiconducting SWNTs. The normalized [C8-SG65i] absorption spectra is shown in Fig. 6.2 b) [black dotted line] and is completely different from the [SDBS-SG65i] spectrum [red dotted line]. Clearly, there is only one dominating species (6,5) with an E_{11} resonance at 988nm accounting for ~99.5% of all tubes as reported below. A very small red shift (5 nm) is seen in the polymer-SG65i nanohybrid compared to SDBS- SG65i solution which could be due to the dielectric coulombic interactions in the nanotube by the wrapping C8 polymer. Fig 6.22 a) also shows the spectra of PFO-SG65i species. The flat background below 500 nm indicates the removal of any metallic species from the starting material. The normalized absorption spectra of PFO-SG65i (Fig 6.2 (b)) indicates the presence of dominating (7,5) tubes with the E_{11} resonance at 1045nm. Small amounts of (6,5), (7,6) and (8,6) tubes are also present from their respective E_{11} resonance peaks at 992 nm, 1135nm and 1194 nm, but these tubes comprise less than 25% of the total. Again, the E_{11} resonance peaks are red-shifted relative to the [SDBS-NT] distribution mainly due to the dielectric screening effect.

6.3.1 Selectivity Vs Chain Length

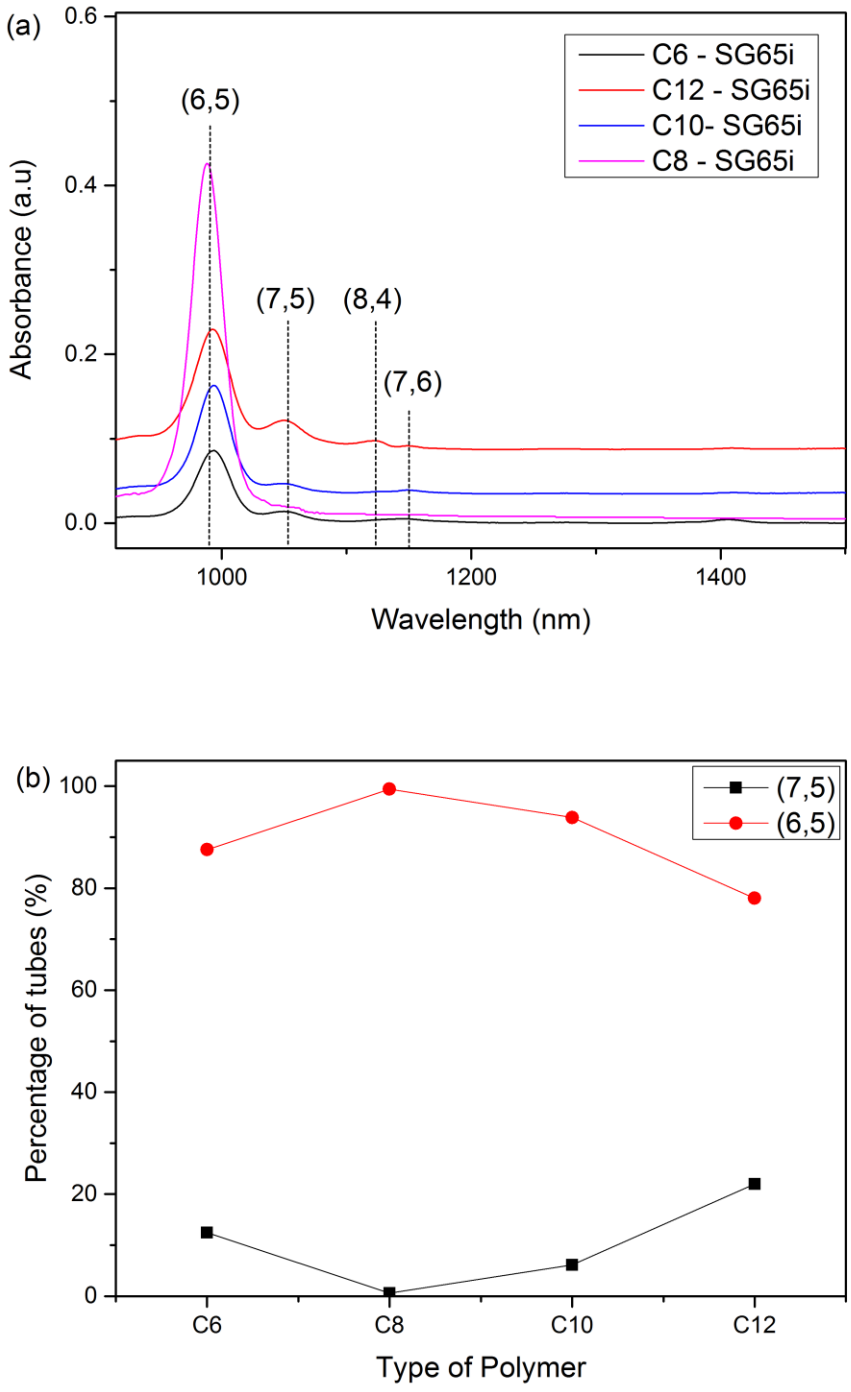

Figure 6.3: a) Absorption spectrum of SG65i tubes wrapped by various polymers b) Graph showing the percentage of tubes present in the solution depending on the type of polymer used.

Figure 6.3 a) shows the absorption spectra of SG65i SWNTs wrapped by C6, C8, C10 and C12 polymers in o-xylene. All the polymers show well resolved absorption peaks in the NIR region. The polymers C6, C10 and C12 show four distinctive peaks that are attributed to the first van Hove bandgap E_{11} at 988, 1044, 1136 and 1118 corresponding to (6,5), (7, 5), (7, 6) and (8,4) chirality tubes. These polymers exhibit a similar selectivity yet vary significantly in terms of the percentage of tubes suspended in the supernatant solution as seen in Fig 6.3 b). The C8 polymer wrapped nanotubes shows one strong peak at 988nm which corresponds to (6, 5) tubes. It should also be noted that the starting material (SG65i) contains only 40% of (6,5) tubes [30]. The C8 shows remarkably strong selectivity (~99.5%) towards the lower diameter (6, 5) tubes at the same time ruling out the other tubes (~0.5%) in the process. This behaviour changes significantly when we alter the chain length of the polymer. Increasing the alkyl chain causes the polymer to effectively wrap larger diameter tubes as well, which is quite consistent with the literature [33]. The concentration and selectivity of the single walled carbon nanotubes thus depends strongly on the length of the alkyl chains at the C-bridging atom, and by optimising the chain length, we see a giant enhancement of the nanotube chirality selection.

6.3.2 Selectivity Vs Starting SWNT Materials

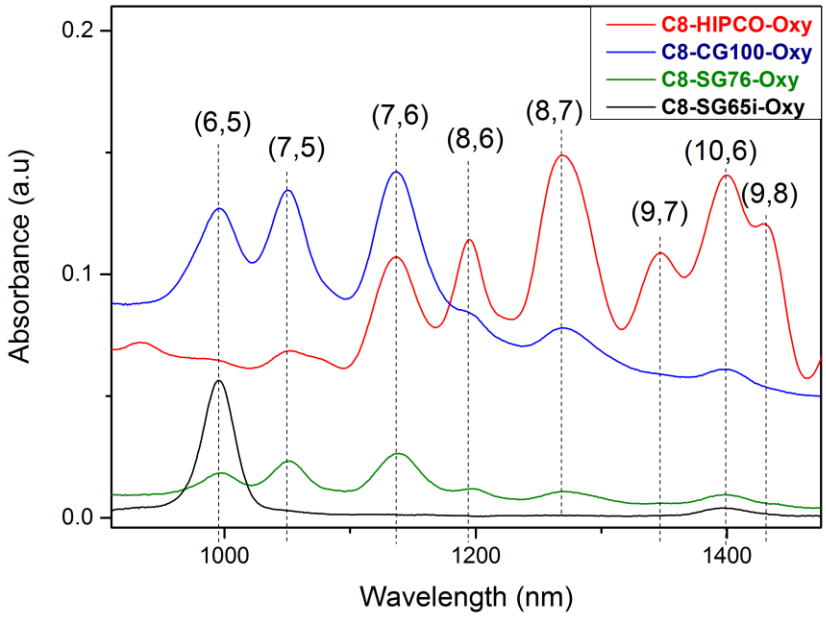

. **Fig 6.4:** Absorption spectrum of C8-SWNT with different SWNT starting materials. Please note: C8-SG65i-oxy was diluted (1/8th) for comparison purposes.

In order to get a broader perspective with these results, we prepared C8-SWNT hybrid solutions with different types of SWNT starting materials (CG100, SG76 and HIPCO) based on different diameter nanotubes. Figure 6.4 shows the C8-SG65i nanohybrid suspension has the strongest absorption spectrum (Please note: the solution was diluted 8:1) and according to Beer's Law contains the largest tube concentrations, which is also reflected by the strong PL intensities as reported below. The absorption of C8-CG100, C8-GS76 and C8-HIPCO nanohybrids are much smaller compared to C8-SG65i tubes which is also clearly seen in PLE maps (reported below) where they show much lower PL intensities when compared to SG65i tubes. The nanohybrids prepared from these starting materials

were not strongly selective to (6, 5) tubes. As identical preparation methods and conditions were applied, we conclude that the C8 polymer seems to show much greater selectivity towards a monochiral chiral (6, 5) tubes when a SG65i starting material is used due to its proportionally much higher presence in the staring material. All these solutions showed very good stability even when stored for several weeks. It should also be noted that the other starting materials have significantly lower (6,5) tube population, hence the selectivity was not strong. In addition, it can be observed that there is an increase in the background absorption when the polymer is interacting with other SWNTs starting materials. This could be due to SWNT bundles, presence of impurities or trace amount of catalyst present in the starting material. Except SG 65i starting materials, all the other SWNT sources have slightly higher concentration of wide range of SWNT diameters. We speculate that the polymer backbone shows great affinity towards larger diameter tubes when the amount of larger diameter tubes is higher in the starting material. This data is quite consistent with the data obtained by Nish et al. for PFO wrapped CoMoCAT-SWNTs and HIPCO-SWNTs where PFO shows strong selectivity towards (7,5) tubes when CoMoCAT was used as a starting material and it wraps different NT chiralitires when HiPCO-NT was used as a starting material [10].

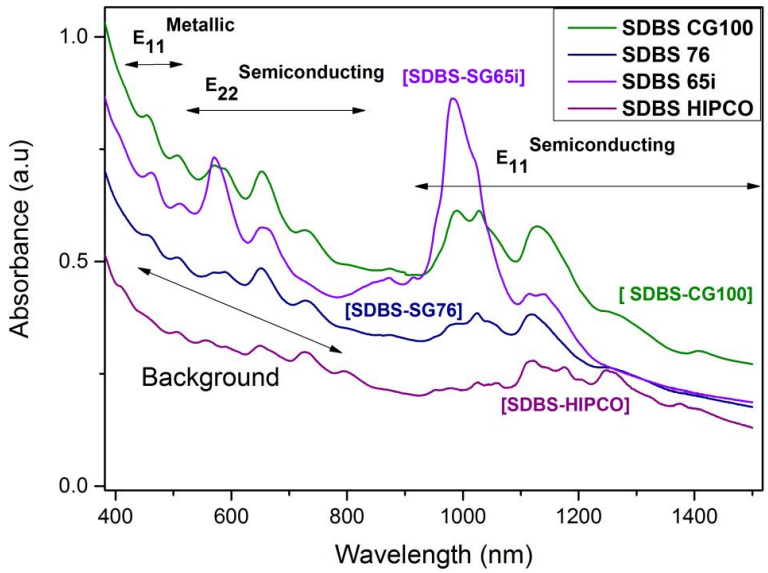

Figure 6.5: Absorption spectrum of HIPCO, SG76, CG100 tubes with SDBS showing the presence of metallic species in their respective solutions.

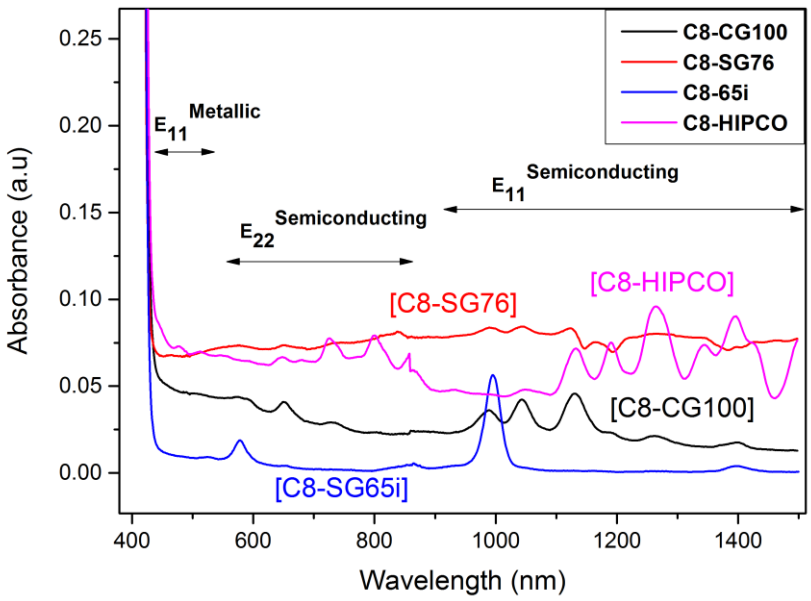

Figure 6.6: Absorption spectrum of HIPCO, SG76, CG100 tubes with C8 polymer showing the absence of metallic species in their respective solutions.

Fig 6.5 shows an absorption spectrum of the dispersed SDBS-HIPCO, SDBS-SG76 and SDBS-CG100 distribution over a fuller wavelength range. The semiconducting E_{11}^{S} transitions are seen in the NIR range [900-1500nm], the semiconducting E_{22}^{S} transitions in the visible region [550-750nm] and few metallic E_{11} transitions are seen below 500 nm. The wide background in all the samples is primarily attributed to the metallic species. The spectra of C8-HIPCO, C8-SG76 and C8-CG100 clearly show that the broad metallic background is completely removed (Fig 6.6). From the above figures, it is quite clear that our polymer C8 has the ability to remove all the metallic species from different SWNT starting materials with wide range of diameters.

6.4 PLE Spectroscopy

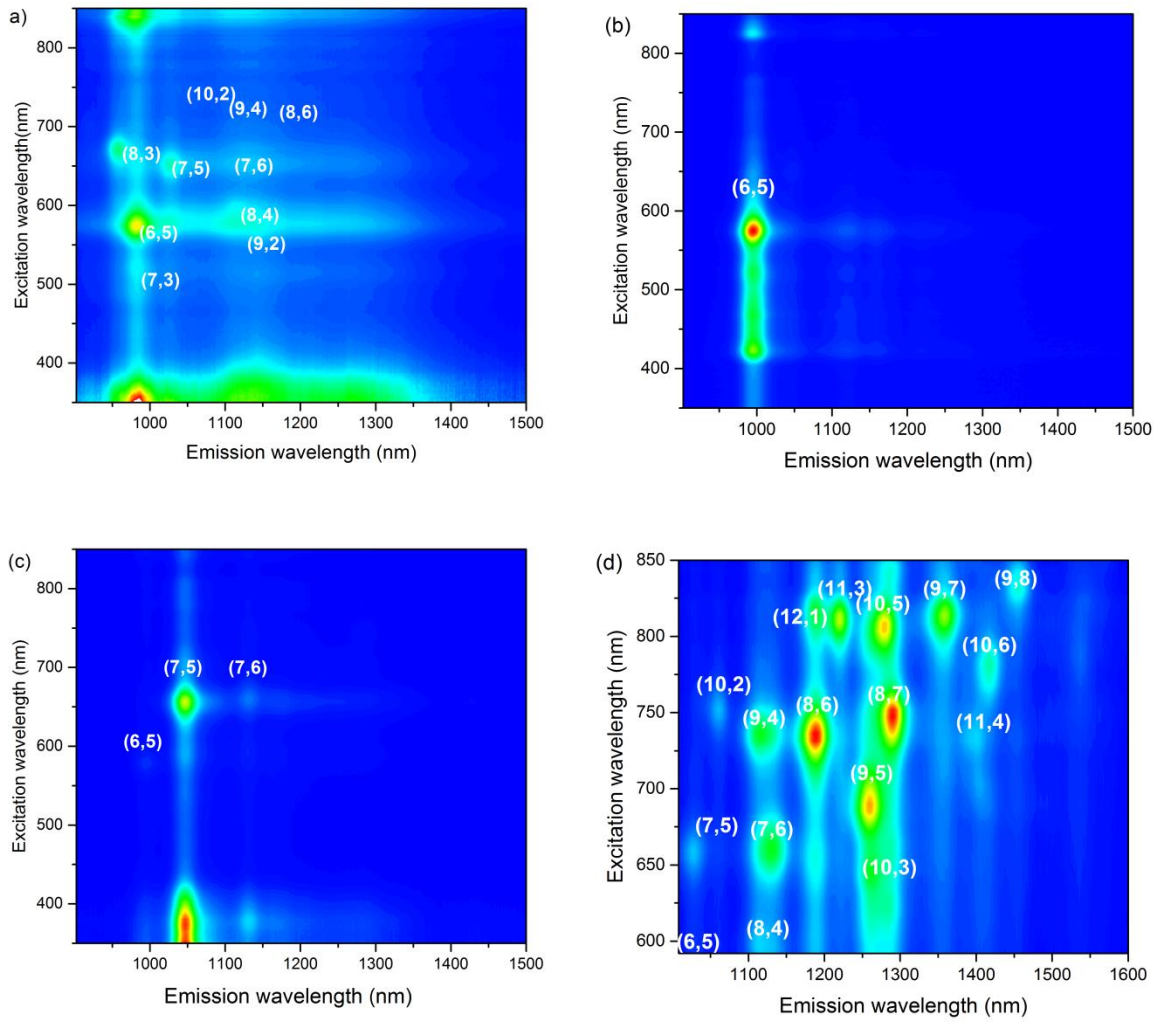

Figure 6.7: shows PLE false color contour map for a) SDBS-SG65i showing the entire distribution of the starting material. b) C8-GS65i showing monochiral wrapping of (6,5) tubes. c) PFO-SG65i showing the wrapping of dominant (7,5) tubes. d) C8-HIPCO showing the dispersion of wide variety of higher diameter tubes.

Due to spectral congestion, it is quite hard to assign each peak in absorption spectra, especially when a large number of NT species are present. By contrast, increased spectral

resolution for tubes with different chiral indices can be obtained by resonant excitation into the E_{22} states using photoluminescence excitation (PLE) spectroscopy which is a powerful tool to assign nanotube species and determine any associated peak shifts. [24] Figure 6.7a) shows a PLE false color contour map for an SDBS-GS65i sample in D_2O. Higher emission intensities in this map are shown in red and lower emission intensities in blue. The species were assigned using the Weisman and Bachilo empirical model [25] and demonstrate clearly that although the largest component is the (6,5) tubes, there is a significant residual component of other species.

Figure 6.7b) shows the PLE false color contour map for the C8-SG65i sample in o-xylene. The excitation range of 550-800 nm shows E_{11} emission peaks resulting from direct excitation into the E_{22} transitions of only one semiconducting species (6,5) of SWNTs. In addition, a peak at 410 nm corresponding to C8 absorption, also gives rise to emission from the nanotubes. This is the signature of an energy transfer process, where excitons on the C8 polymer are non-radiatively transferred to the nanotube where they subsequently recombine. In addition to the E_{22} resonance, several satellite peaks are observed which arise from absorption by phonon-assisted transitions followed by E11 emission of the (6,5) tube. The creation of a G-band phonon with electronic excitation leads to satellite peaks at E_{11} + 200meV ~ 840nm and E_{22} + 200meV ~ 520nm [28, 29].

Figure 6.7c) shows a PLE false color contour map for PFO-SWNT sample in o-xylene. The sample has high quantities of (7,5) species and some trace amounts of (6,5) and (7,6), as seen from their E_{22} resonances at ~658nm and ~580nm, respectively. The energy transfer at 380nm corresponds to absorption by PFO at 350-440nm and subsequent emission from the nanotube E_{11} transitions. Figure 6.7d) shows PLE false color contour map for C8-HIPCO sample in o-xylene. The sample contains wide variety of the nanotubes

from diameter 0.8-1.2 nm just like the starting material with high quantities of (8,6) and (8,7) tubes. Our C8 polymer shows selectivity to semiconducting tubes with both smaller and larger diameters.

6.4.1 Selectivity Vs Chain Length

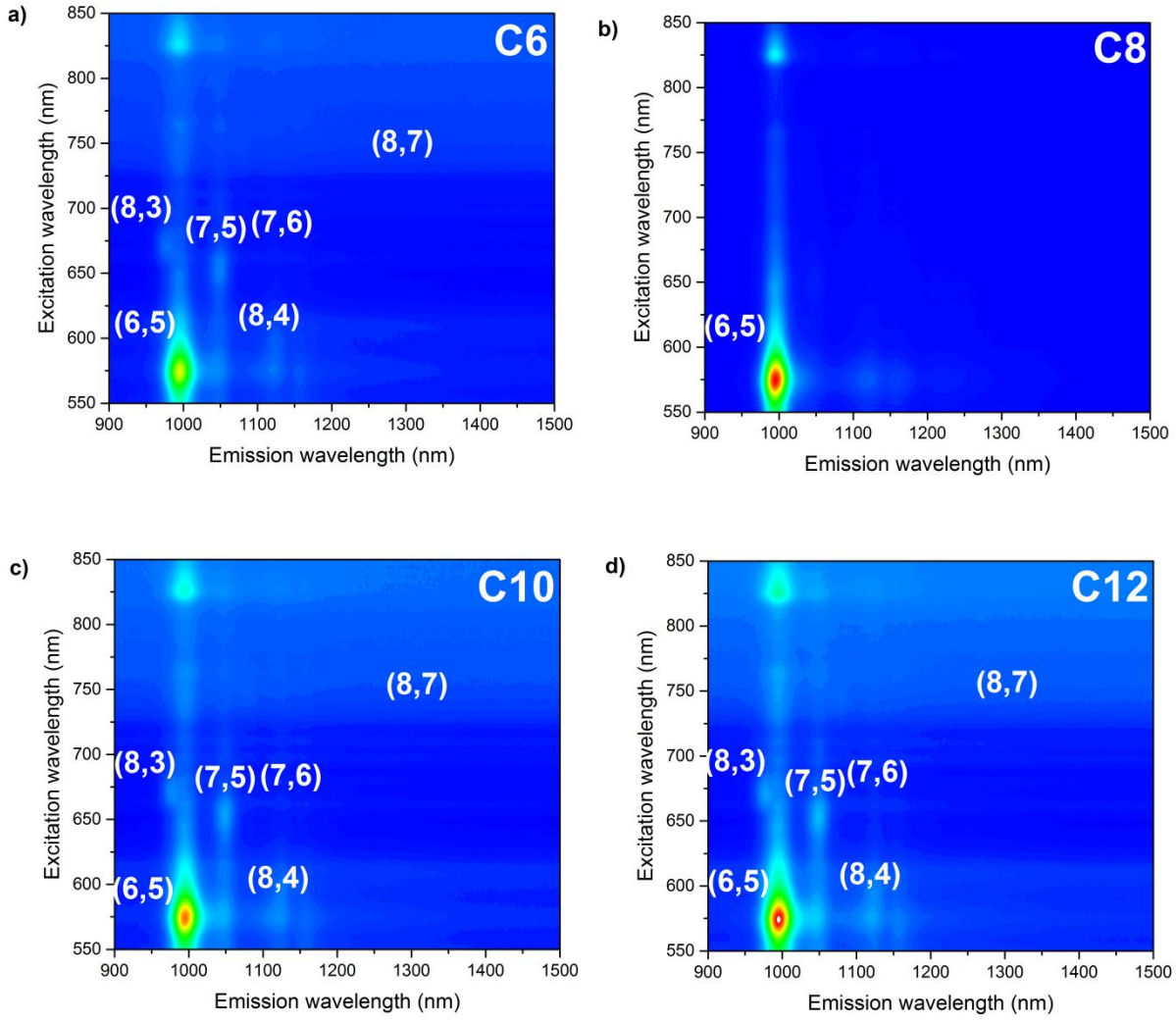

Figures 6.8: a), b), c) and d) shows the normalised PLE false color contour maps of C6, C8, C10 and C12 SWNT nanohybrids in o-xylene solution, respectively.

We now vary the chain length as in Fig 6.8 where the excitation range of 550-800 nm shows E_{11} emission peaks resulting from direct excitation into the E_{22} transitions of five different semiconducting species [(6,5), (7, 5), (7, 6), (8, 4) and (8, 7)] of SWNTs. The low absorbance and weak selectivity of the C6 polymer could be due to its low solubility compared to other polymers with higher alkyl chains. The selectivity of only one SWNT species by C8 polymer [Fig. 6.8.b)] could be due to the non-planar triarylamine on backbones showing higher affinity to the smallest diameter nanotube combined with the presence of large quantities of the same nanotube species in the staring material. By increasing the chain length, the polymers C10 and C12 showed more solubility for SWNTs from diameters between 0.78-0.89nm while still showing dominant selectivity (>80%) towards (6,5) tubes as seen in figure 6.9 a). Therefore, the wrapping and selection mechanism of SWNTs is not only indicated by the backbone of the polymer but also by the length of the alkyl side chain. In addition, solvent plays a major role in the selectivity of the SWNTs. Both toluene and o-xylene are perfect solvents for the selectivity of (6,5) tubes by C8. However, when chorobenzene or dicholorobenzene were used, the polymer C8 solublises other tubes [(7,5) and (7,6)] in the starting material, which are consistent with the results published elsewhere [10, 12].

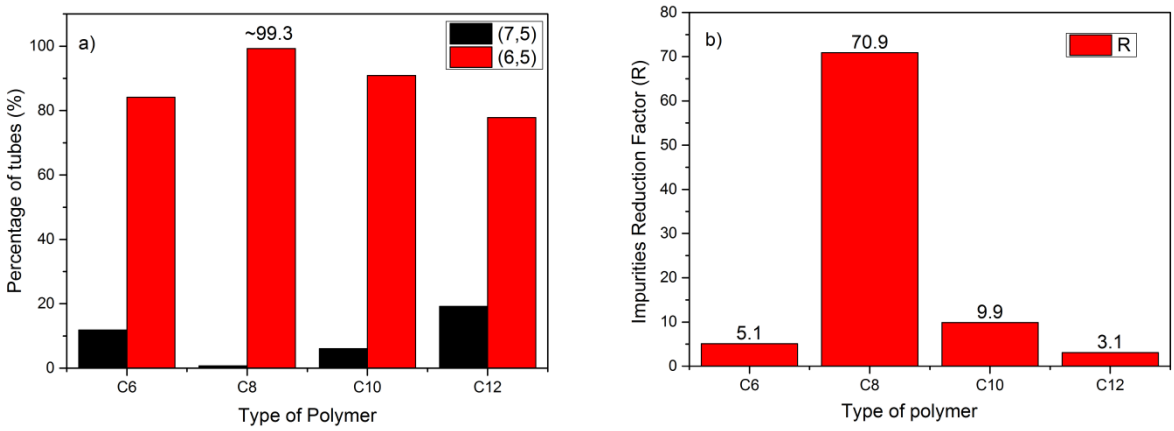

Figure 6.9: a) Column graph showing the percentage of tubes present in the supernatant solution, when polymers with different side chain are added. b) Column graph showing the impurities reduction factor with respect to the type of polymer used.

Defining all non (6,5) species as impurities, we can measure their reduction through the solubilisation process in terms of their relative PLE intensity $I_{n,m}^{t}$ by a factor

$$R = \frac{\pounds_{n,m}^{i}}{\pounds_{n,m}^{t}} = \frac{0.6}{I_{7.5}+I_{7.6}+I_{8.3}+I_{8.4}+I_{8.7}} \qquad \textbf{[6.1]}$$

Where 0.6 represents the initial concentration (60%) of non (6,5) species. Fig 6.9 b) shows that this factor has a very dramatic peak for C8, leading to a ~71 fold reduction in the presence of other species.

6.5 Raman Spectroscopy

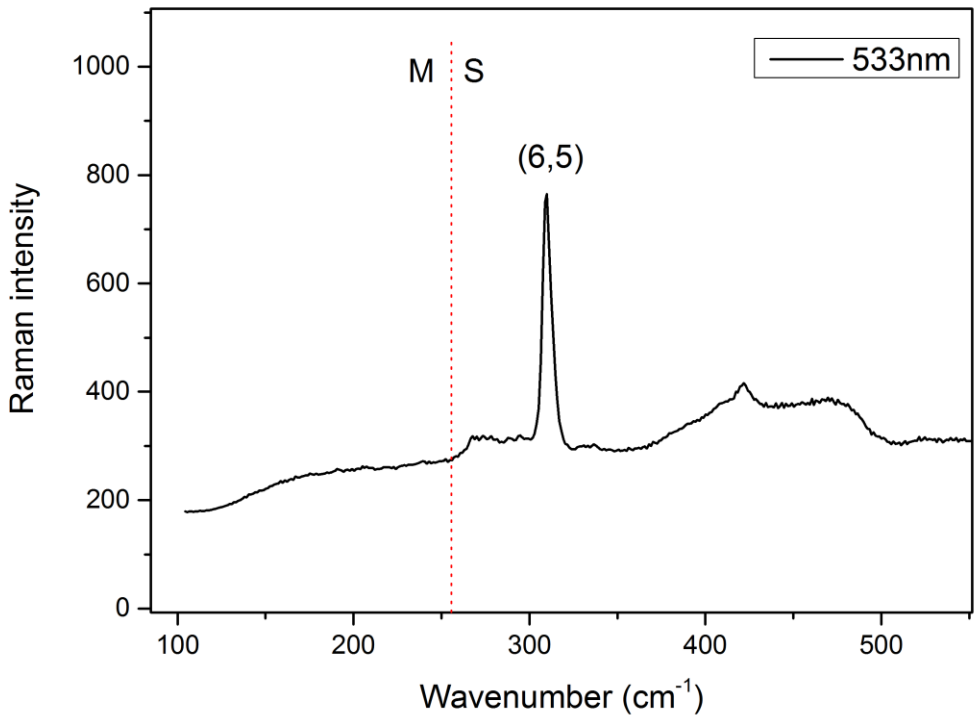

Figure 6.10: Raman spectrum of the RBM region for C8-SG65i tubes on o-xylene films.

The presence of metallic tubes in the nanohybrids can easily be detected by Raman spectroscopy (introduced in Chapter 2). Hence, we performed the Raman measurement by exciting the nanohybrids at 533 nm (2.33eV). The 2.33 eV excitation line is mainly in resonance with met-SWNTs within the range of radial breathing mode peaks from 180 to 260 cm-1. The RBM peaks that are attributed to the semi-conducting SWNTs can be seen from 260 to 320 cm-1. As seen from the Figure 6.10, there are no peaks in the range of RBM mode that are corresponding to metallic species whereas the single distinctive peak at 308cm-1 corresponds to (6,5) tubes. This result clearly coincides with the absorption data

that C8 polymer does not wrap the metallic nanotubes and wraps only the monochiral (6,5) tubes.

6.6 Atomic Force Microscopy(AFM)

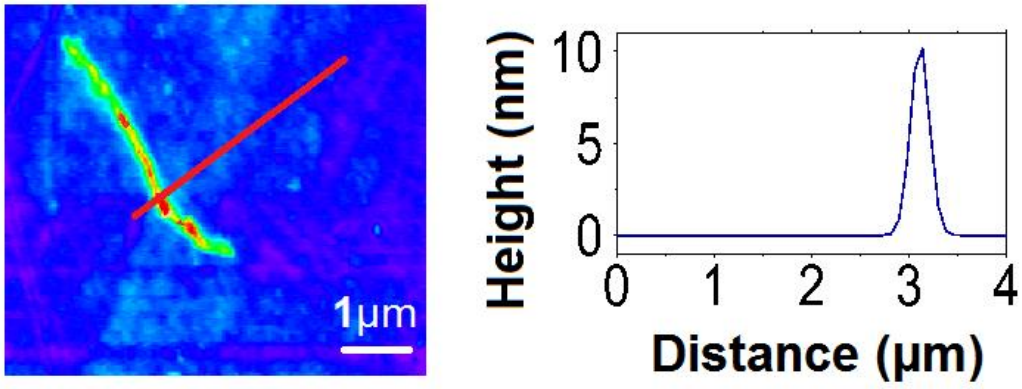

Figure 6.11: AFM images of dilute C8-SG65i tubes on quartz substrate and its height profile.

AFM images were obtained using a Thermo Microscope M5 in non-contact mode. Samples were prepared by spin-coating a diluted (1/200) solution at 1500 rpm on a quartz substrate, which were briefly tip sonicated to remove any potential nanotube bundles, followed by annealing at 150C for 15 minutes. The height profile clearly shows the polymer wrapping around the tube with a typical height of 10nm indicating the presence of multiple layers of polymers surrounding the tube. This could explain the high selectivity seen in the SG65i material, since it suggests that the (6,5) tubes extract all of the polymer from the solution by preferential wrapping before other species can be solubilised. The average length of the tubes is around 4μm, consistent with the length of the starting material, indicating the tubes were not damaged during the sonication process.

6.7 Scanning Electron Spectroscopy Images

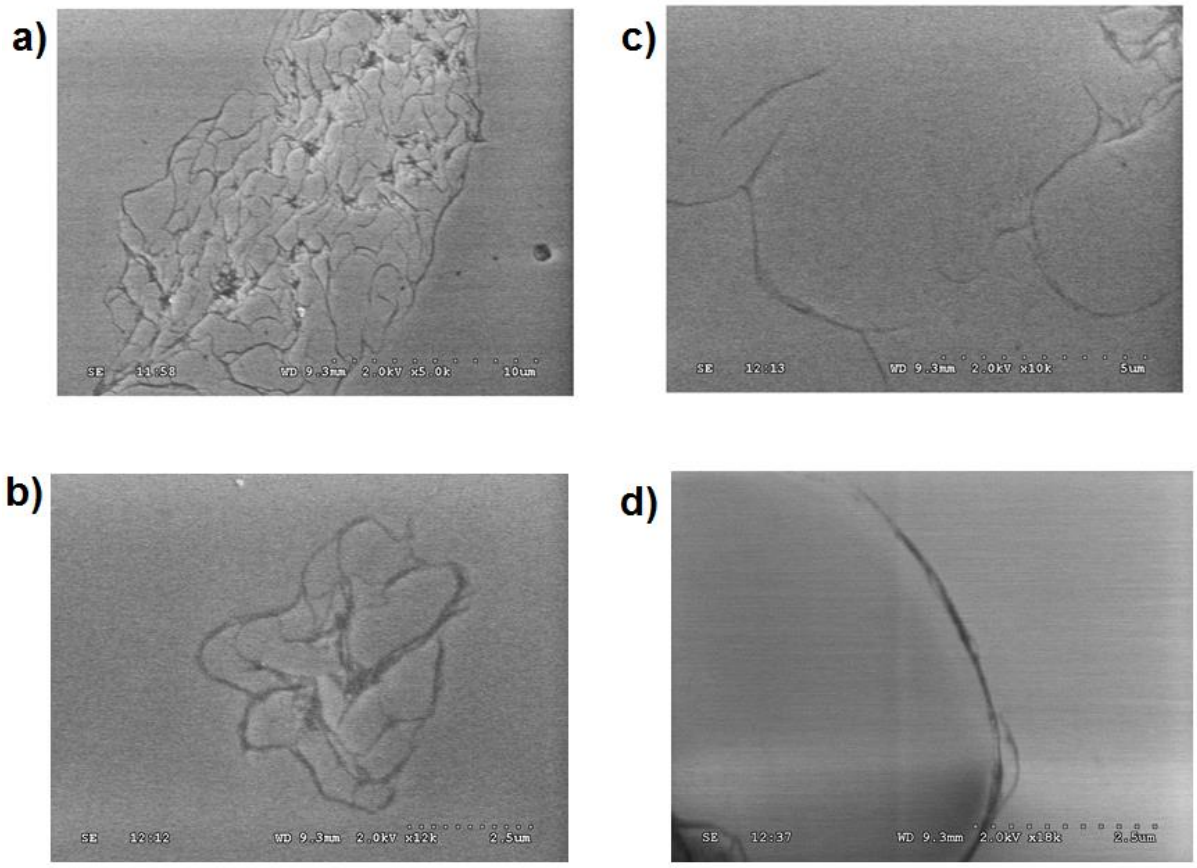

Figure 6.12: SEM images of a) and b) the actual C8-SG65i sample drop casted on a silicon surface. c) and d) diluted sample (1/100) spin coated at 100rpm.

Scanning electron microscopy images indicate both both bundled and unbundled nanotubes with some polymer crystals embedded on it during the drying process (Fig 6.12 a) and b)). They form a close network of tubes when drop casted. The results suggest that SWNT's wrapped with C8 do aggregate into small bundles as the film begins to dry. As seen in Fig 6.12 c) and d), individual tubes can be studied by spin coating dilute solutions of the hybrid on Si. The average length and the thickness of the nanohybrids are consistent with the results obtained from AFM.

6.8 Summary

A series of Polytriarylamine based polymers were synthesized with increasing side chain functionalities via Suzuki coupling polymerization. We investigated the properties of these polymer wrapped single walled carbon nanotubes and found that they were able to successfully remove the metallic impurities in both higher diameter [HIPCO] and lower diameter [SG65i] carbon nanotube starting material. In addition, highly selective wrapping of only one SWNT species (6,5) can be made possible by optimising the chain length of the polymer. The estimated purity of the mono-chiral SWNTs is ~99.3% for (6,5) tubes, which is significantly higher than the previously reported values [31,35,36]. From the PLE studies, our calculation showed that there is a ~71 fold reduction in the intensity of other SWNT chiralities compared to the SG65i starting material. In addition to its high mobility, our smaller bandgap polymer, C8, has a matching electronic band alignment with the (6,5) tubes. Hence, these fully semiconducting, mono-chiral C8-SG65i nanohybrids can be used as HTL in transistor and photovoltaic applications.

Reference

[1]. De Volder, M. F., Tawfick, S. H., Baughman, R. H. & Hart, A. J. Science 339 535–539 (2013).

[2]. Hirlekar, R., Yamagar, M., Garse, H., Vij, M. & Kadam, V Asian J Pharmaceut Clin Res 2 (2009).

[3]. Arnold M. S, Stupp S. I, Hersam M. C, Nano Lett. 5 713 (2005).

[4]. F. Bonaccorso, T. Hasan, P. H. Tan, C. Sciascia, G. Privitera, G. Di Marco, P. G. Gucciardi and A. C. Ferrari Phys. Chem. C, 114 (41) 17267–17285 (2010).

[5]. Arnold M. S, Green A. A, Hulvat J. F, Stupp S. I, Hersam M. C. Nat. Nanotechnol. 1 60 (2006).

[6]. Alexander A. Green and Mark C. Hersam Adv. Mater. 23 2185–2190 (2011).

[7]. Zheng, M. & Semke, E. D, J. Am. Chem. Soc. 129 6084–6085 (2007).

[8]. Joseph McMorrow, Mark Freeley, and Matteo Palma, Ind. Eng. Chem. Res., 56 (18) 5302–5308 (2017).

[9]. Daniel P. Salem, Markita P. Landry, Gili Bisker, Jiyoung Ahn, Sebastian Kruss, Michael S. Strano, CARBON 97 147–153 (2016).

[10]. Adrian Nish, Jeong-Yuan Hwang, James Doig & Robin J. Nicholas. Nature Nanotechnology 2, 640-646 (2007).

[11]. Maria Antonietta Lo et al, Small Methods 2 1700335 (2018).

[12]. Schuettfort T, Snaith H, Nish A, Nicholas R. Nanotechnology 21 025201 (2010).

[13]. S. D. Stranks, C.K. Yong, J. A. Alexander-Webber, C. Weisspfennig, M. B. Johnston, L. M. Herz, R. J. Nicholas. ACS Nano 6 6058 (2012).

[14]. Dominick J. Bindl and Michael S. Arnold. J. Phys. Chem. C 117 2390−2395 (2013).

[15]. Pramod M Rajanna et al Nanotechnology 29 105404 (2018).

[16]. T. Wang, H. Wang, G. Li, M. Li, Z. Bo and Y. Chen, Macromolecules, 49 4088–4094 (2016).

[17]. R. Kandre, K. Feldman, H. E. H. Meijer, P. Smith and A. D. Schlüter, Angew. Chem., Int. Ed., 46 4956–4959 (2007).

[18]. Lian W.R, Huang Y.C, Liao Y.A, Wang K.L, Li L.J, Su C.Y, Liaw D.J, Lee K.R, Lai J.Y. Macromolecules, 44 9550–9555 (2011).

[19]. Chen, W.-H.; Wang, K.-L.; Liaw, D.-J.; Lee, K.-R.; Lai, J.-Y. Macromolecules 43 2236–2243 (2010).

[20]. Chen, M.-C.; Liaw, D.-J.; Chen, W.-H.; Huang, Y.-C.; Sharma, J.; Tai, Y. Appl. Phys. Lett. 99 22330510 (2011).

[21]. Xu X, Zhu Y, Zhang L, Sun J, Huang J, Chen J, Cao Y. J. Mater. Chem. 22 4329–433610 (2012).

[22]. Shi, W.; Fan, S.; Huang, F.; Yang, W.; Liu, R.; Cao, Y. J. Mater. Chem. 16 2387–239410 (2006).

[23]. Wang P.I, Shie W.R, Jiang J.C, Li L.J, Liaw D.J. Polym. Chem. 7 1505–151610 (2016).

[24]. Sebastian Heeg, Ermin Malic, Cinzia Casiraghi, Stephanie Reich. Phys. Status Solidi (b) 246 2740 (2009).

[25]. R. B. Weisman & S. M. Bachilo, Nano Lett., 3 1235 (2003).

[26]. H. Htoon, M. J. O'Connell, S. K. Doorn, & V. I. Klimov, Phys. Rev. Lett., 94 127403 (2005).

[27]. Ting Lei, Igor Pochorovski and Zhenan Bao. Acc. Chem. Res., 50 (4) 1096–1104 (2017).

[28]. V.Perebeinos, J.Terso, & P. Avouris, Phys. Rev. Lett., 94 027402 (2005).

[29]. S. G. Chou, F. Plentz, J. Jiang, R. Saito, D. Nezich et al., Phys. Rev. Lett., 94 127402 (2005).

[30]. https://www.sigmaaldrich.com/Graphics/COfAInfo/SigmaSAPQM/SPEC/77/773735/773735-BULK_ALDRICH_.pdf.

[31]. Yohei Yomogida , Takeshi Tanaka , Minfang Zhang, Masako Yudasaka , Xiaojun Wei & Hiromichi Kataura Nature Communications volume7, Article number: 12056 (2016).

[32]. Po-I Wang, Chou-Yi Tsai, Yung-Jou Hsiao, Jyh-Chiang Jiang, and Der-Jang Liaw. Macromolecules, 49 (22) 8520–8529 (2016).

[33]. Suman Kalyan Samanta, Martin Fritsch, Ullrich Scherf, Widianta Gomulya, Satria Zulkarnaen Bisri, and Maria Antonietta Loi. Acc. Chem. Res., 47 (8) 2446–2456 (2014).

[34]. Bachilo, S. M. et al., Science 298 2361–2366 (2002).

[35]. Tu, X. M., Manohar, S., Jagota, A. & Zheng, M. Nature 460 250–253 (2009).

[36]. Liu, H., Nishide, D., Tanaka, T. & Kataura, H. Nat. Commun. 2 309 (2011).

Chapter 7

Highly Pure Polymer-SWNT Nanohybrid Networks for Highly Efficient and Stable Organic Solar Cells.

7.1 Introduction and Background

Organic Solar Cells (OSCs) are of great interest in recent years due to its low cost and possible long-term sustainability for solar energy harvesting [1]. They have come a long way in recent years and the efficiency of the device has risen from just 5% to 14% for a single cell [2, 3] and to more than 17% for a tandem cell [4]. Single walled carbon nanotubes (SWNT) are promising candidates in organic solar cells due to their electronic properties such as long lived charge transport [5], high mobility, high transparency, excellent robustness and one-dimensional structure and good ambient stability [6, 7]. The initial synthesis of SWNTs produces bundles of tubes consisting of a mixture of different chiralities of both semiconducting and metallic nanotubes [8]. We have previously shown that wrapping SWNT with certain polymer types can be used to solubilize, purify and separate metallic and semi-conducting tubes [9, 10, 11]. Non-covalent binding of Polymers to SWNTs not only has the advantage of individualizing nanotubes but also helps in retaining their unique properties. The application of semiconducting polymer-SWNT nanohybrids in conventional organic solar cells has proven to produce slightly higher efficiencies compared to PEDOT:PSS [12].

In this chapter, we show that improving the purity of semiconducting polymer-SWNT nanohybrids, leads to the production of highly efficient, long time stable organic

solar cells with improved reproducibility. Regioregular poly(3-hexylthiophene) (rr-P3HT) wrapped SWNT are one of the promising candidates for an alternative HTM due to their favorable bandgap and hole transporting properties [12]. We used a polymer exchange technique for the production of highly pure P3HT-SWNT nanohybrids which are ~ 99.5% semiconducting. We use absorption and photo luminescence excitation spectroscopy measurements to demonstrate the polymer exchange process and how we were able to remove almost all the metallic impurities from the nanohybrids. We used these nanoybrids as HTM in the fabrication of the devices and were able to achieve high efficiencies and long term stable devices with improved reproducibility. Under an AM 1.5G 1 sun illumination, the PTB7/PC71BM devices produced ~9.4% efficiency which is the highest yet obtained by a carbon nanotube based organic solar cell to date [12, 13, 14].

7.2 Sample Preparation

HiPCO SWNTs with diameter in the range 0.8–1.2 nm were purchased from Unidym in the raw form and oven-dried (120°C, 4 hours). Regioregular poly(3-hexylthiophene-2,5-diyl) (P3HT) with molecular weight 50 000 – 70 000 g mol^{-1} was used as received from Rieke Metals, Inc. PFO (molecular weight 36 kgmol−1) was used as received from American Dye Source, Inc.,. [PFO-NT] was prepared by adding 0.6 mg/ml of PFO in an o-xylene solution and then adding HIPCO nanotubes to reach a tube concentration of 0.5 mg/ml, followed by treatment of the mixture in an ultrasonic disintegrator for 15 minutes. A typical batch would consist of two 30–50 ml batches of solution and sonication would be carried out on 10 ml portions at a time to ensure adequate heating and sonication. This step was followed by microcentrifugation for 8 minutes at 10,000×g and retention of the upper 85% of supernatant containing the dispersed tubes.

Now, the excess polymer was discarded by rotary evaporation in which the total volume of nanohybrid solution was reduced to about one fifth of the original volume, causing the nanohybrids to aggregate spontaneously. The aggregated mixtures were then microcentrifuged for 4 minutes at 16,000×g and the supernatants, containing excess polymer, were discarded and the residues redissolved in fresh o-xylene. For the polymer exchange, 6mg of P3HT was added to the final [PFO-NT] solution, followed by tip sonication for 15 minutes and centrifuging for 8 minutes at 16,000×g. This process was repeated a total of three to four times to ensure the removal of as much excess polymer as possible and there by getting highly pure, PFO free, [P3HT-NT] nanohybrids. The final residues were redissolved in small volumes of chloroform and chloroform:DMF for the experiments presented in this work.

Please note: SWNT produced by the HIPCO method were wrapped with rr-P3HT by two different routes, either 1. By direct wrapping, or 2. via polymer exchange in which a layer of PFO was first applied and subsequently exchanged with rr-P3HT in solution.

Fabrication of solar cells:

Electron donor material PTB7 and electron acceptor PC71BM were purchased from 1-material Chemscitech and Aldrich, respectively, and used as received. The PEDOT:PSS (Clevios P AI4083) was obtained from Ossila Ltd. The conventional structure was ITO/P3HT-NT/PTB7:PC71BM(1:1.5 by weight)/PFN/Ag and the inverted device structure was ITO/PFN/PTB7:PC71BM/MoO3/PEDOT:PSS(modified)/P3HT-NT/Ag. For regular devices, a ~3 nm thick, metallic nanotube free, P3HT-NT layer was spin-cast from a chloroform solution on a precleaned ITO substrate, which was treated by oxygen plasma for 4 min, at 1000rpm for 1 min and then dried at 120 degree Celsius for 10 minutes. The PTB7:PC71BM active blend layer, with a nominal thickness of ~85nm was prepared by

spin-coating a mixed solvent of chlorobenzene/1,8-diiodoctane (97:3% by volume) solution (concentration, 25 mg ml) at 900 rpm for 2 min. The PFN interlayer material was dissolved in methanol in the presence of a small amount of acetic acid and its solution (concentration, 2 mg/ml) was spin-coated on top the active layer to give a thickness of 6 nm and a 100 nm Ag layer was subsequently evaporated through a shadow mask to define the active area of the devices (0.0625 cm2) and eliminate edge effects. For an inverted device, PFN was spin coated on the ITO substrate at a nominal thickness of 6 nm, followed by spin coating a ~85 nm thick active layer. Modified protective coating (MoO3:PEDOT:PSS) was spin coated on top of the active layer [15, 16]. The nanotubes were then spin coated on top of the modified PEDOT:PSS followed by evaporating 100nm of Ag. For the reference cell, we thermally evaporate MoO3 on the active layer followed by evaporating 100nm of Ag.

7.3 Absorption Spectroscopy

The absorption spectrum of the PFO-HiPCO nanohybrids (red line) is shown in Figure 7.1. There are five significant chiralities namely the (7,5), (7,6), (8,6), (8,7) and (9,4) tubes, present from their respective E11 peaks at 1045nm, 1135nm, 1194nm, 1285nm and 1349nm. These nanotube peaks are already red-shifted from ionic surfactant (SDBS) wrapped NT due to the dielectric screening caused by the wrapping of PFO [10]. The absorption spectrum of the sample following P3HT polymer exchange and excess polymer removal, [P3HT-(NT)], is also shown (black line). The nanotube E11 transitions are significantly red-shifted, when compared to the PFO-NT nanohybrids, for the (7,5), (7,6) and (8,7) tubes, corresponding to transitions of P3HT-coated tubes, indicating an effective exchange process. However, the (8,6) and (9,4) tubes are not significantly red-shifted suggesting that their interaction with the tubes is significantly weaker.

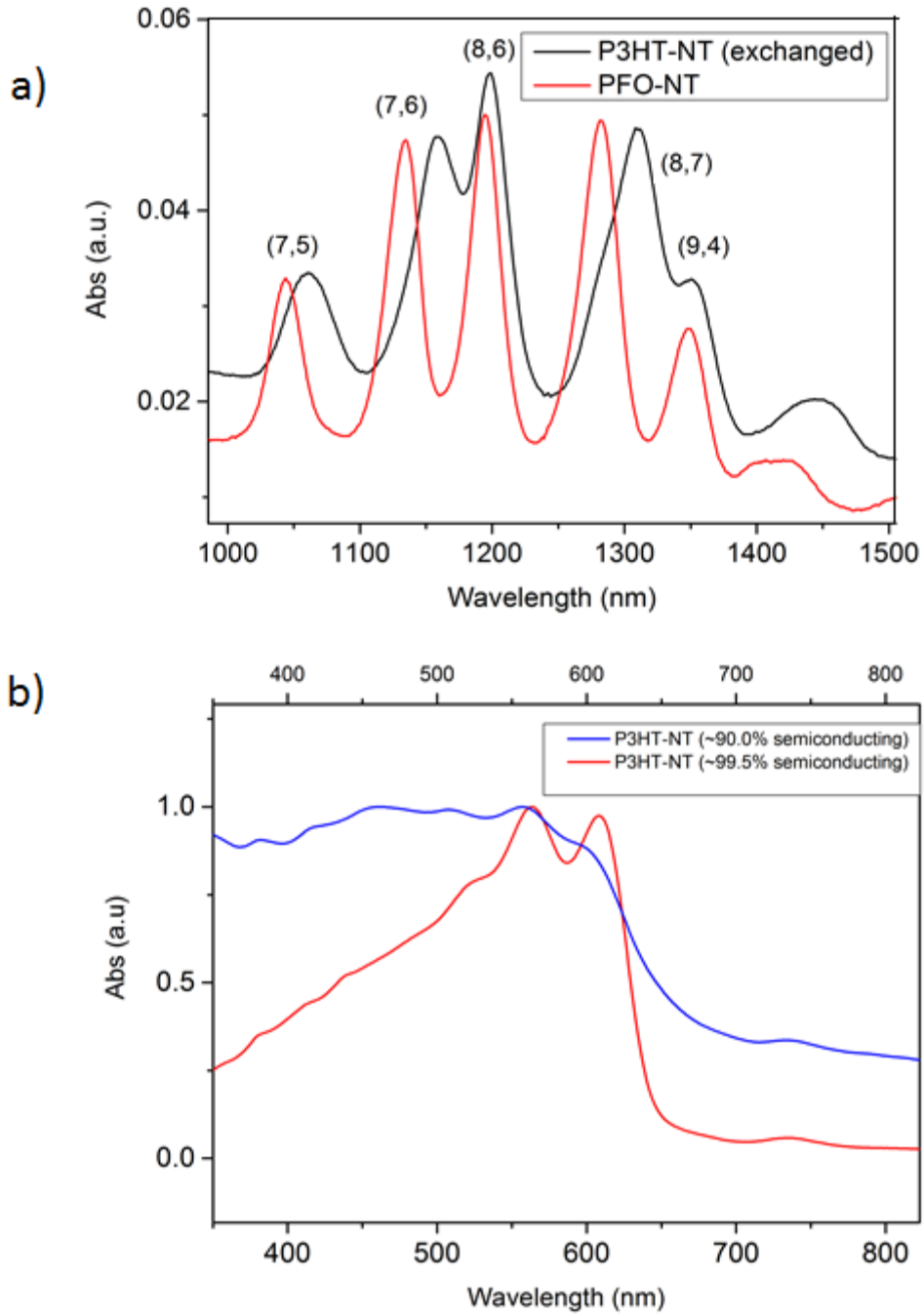

Figure 7.1: a) Absorption spectra of [PFO-NT] (red) and exchanged [P3HT-NT] (black) in o-xylene with excess polymer removed. b) Normalised absorption spectra of the P3HT-NT (blue) and exchanged P3HT-NT (red) samples under investigation with excess polymer removed.

Figure 7.1 b) corresponds to the absorption spectrum of the directly wrapped P3HT-NT (blue line) and exchanged P3HT-NT (red line) nanohybrids that contains SWNTs with E_{22} semiconducting transitions between 500-800nm and E_{11} metallic transitions in the region 400-500nm. The directly wrapped P3HT-NT shows a huge metallic background in the region of 400-500nm but the metallic background is completely removed in the exchanged P3HT-NT due to the fact that PFO has the ability to wrap only the semi-conducting nanotubes [10]. It is also very clear that there is no trace of PFO which should show an absorption peak at 390nm in the exchanged P3HT-NT and the P3HT polymer absorption peak exhibits a strong 0-0 transition (~600nm) that indicates, most of the polymer chains occur in single layer coatings having π-π interactions with the nanotubes. By contrast, in the P3HT-NT absorption, the 0-0 transitions of the P3HT are strongly supressed by the excess polymer present in the aggregated nanoybrids. By integrating nanotube peak intensities, we estimated the purity of the tubes present in the exchanged P3HT-NT to be ~99.5% semiconducting.

7.4 Photoluminescence Excitation Spectroscopy

The PLE maps of PFO-NT (Figure 7.2 a)) shows that the PFO mainly disperses (7,5), (7,6), (8,6) and (8,7) semiconducting nanotubes with the (8,6) being most common. It also shows the energy transfer that takes place due to the PFO absorption in the UV region and emission from the SWNT E_{11} transitions. After the polymer exchange process, almost all the PFO has been exchanged by P3HT which can be observed by the redshift in figure 7.2 b). Hence there is either a little or no trace of PFO in the final exchanged P3HT-NT nanohybrids. Some direct emission from the excess P3HT is observed in the region between 900nm -1050nm due to the absorption into the P3HT at 550-620nm

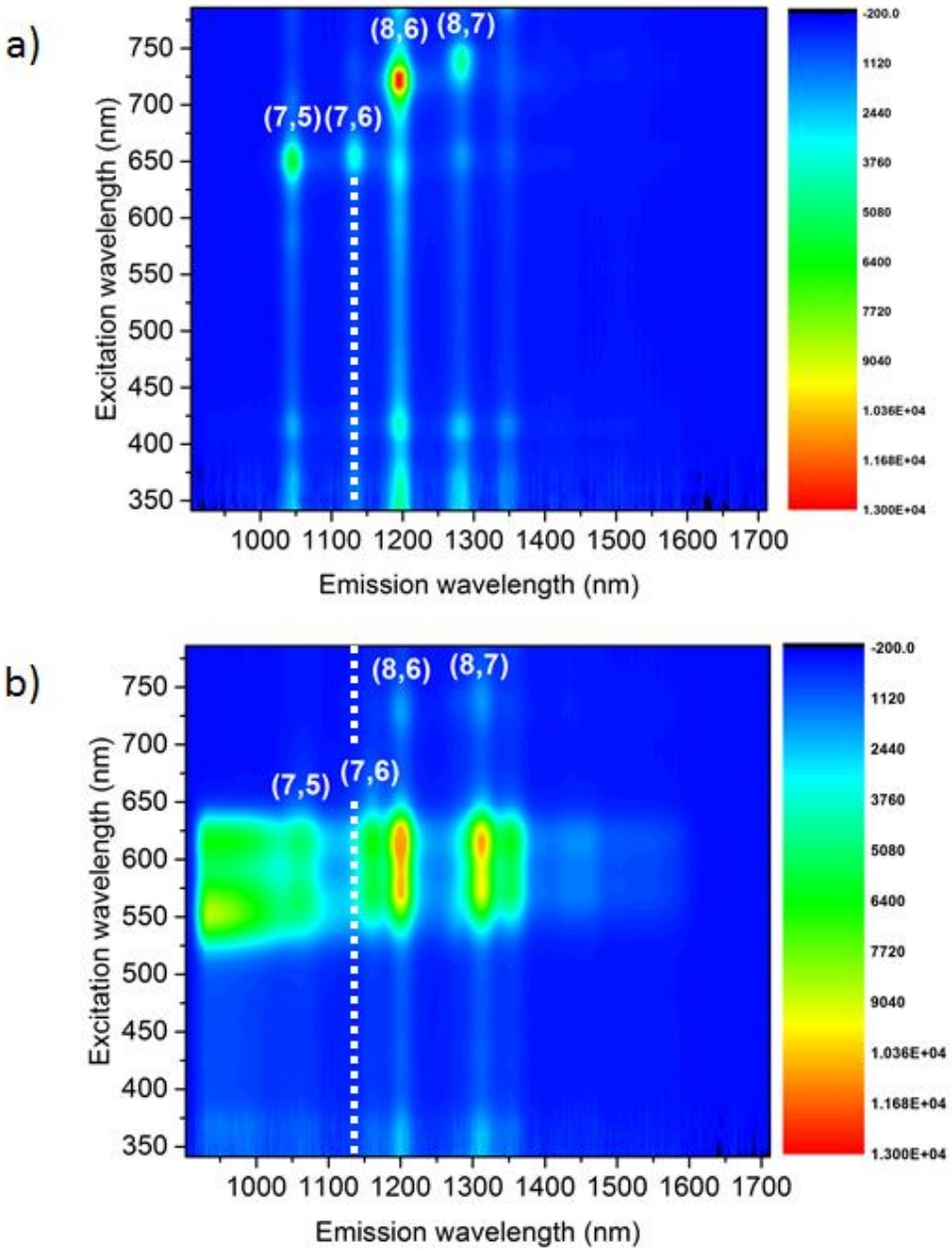

Figure 7.2 a) Photo Luminescence Excitation (PLE) maps of PFO-HIPCO nanohybrids (excess polymer removed) showing four significant nanotube species. Nanotube species were assigned using the values from Weisman and Bachilo [17], red-shifted by 25 meV for PFO. [18] b) PLE maps of exchanged P3HT-HIPCO nanohybrids (excess polymer removed) showing four different nanotube species. Nanotube species were assigned using the values from Weisman and Bachilo [17], red-shifted by 50 meV for P3HT [18].

7.5 Raman Spectroscopy

The presence of metallic tubes in the nanohybrids can easily be detected and confirmed by Raman spectroscopy. Hence, we performed the Raman measurement by exciting the nanohybrids at 633 nm (1.95 eV). The 1.95 eV excitation line is mainly in resonance with met-SWNTs within the range of radial breathing mode peaks from 180 to 240 cm^{-1}. As can be seen from Figure 7.3, in the SDBS-HIPCO starting material (red line), two clear peaks in the RBM region correspond to metallic nanotubes namely (9,9) and (12,3) whereas these peaks were absent in the same range of RBM mode for the exchanged P3HT-NT nanohybrids (black line). This proves that all metallic nanotubes are removed and the exchanged polymer-nanotube nanohybrids are highly semiconducting [14].

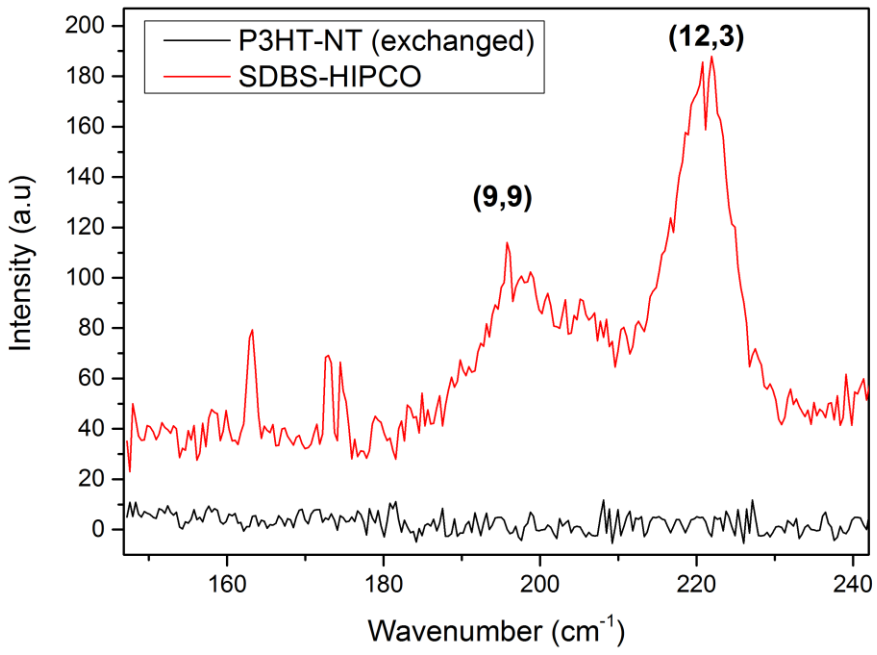

Figure 7.3: Raman spectra (RBM region) excited at 633nm on SDBS-HIPCO (red line) samples and exchanged P3HT-NT (black line)

7.6 Solar cell Fabrication

In this study, we focus on understanding the effect of highly semiconducting nanotube species as hole transporting layers in organic solar cells. Dichlorobenzene was chosen as a solvent for dispersing the nanotubes as it prevented the formation of aggregates for a significant amount of time. Thin layers (~3nm) of highly semiconducting P3HT-HIPCO nanohybrids were spin coated on to the plasma etched ITO substrates and heated at 120 degree Celsius for 10 minutes to remove the dichlorobenzene. AFM images confirm that the nanotubes are well dispersed over the entire surface of the film. Since ~99.5% of these nanotubes are semiconducting, this significantly reduces the probability of device failure due to short circuiting which can happen even with minute traces of metallic nanotubes. The transmission of the exchanged nanohybrids layer is higher (~91.5% at 550nm) than the directly wrapped layer P3HT-NT (~89%) as the multiple polymer exchange process removes all the excess polymers and only a monolayer of polymer wraps the nanotube. For the active layer, we used PTB7 as the electron donor and $PC_{71}BM$ as the acceptor material. We fabricated both conventional and inverted device structures as shown in figure 5 and compared the use of highly semi-conducting polymer-nanotube nanohyrid species as hole transporters in the two device structures. The current density-voltage (J-V) characteristics of the conventional cell with PEDOT:PSS and exchanged P3HT-NT, under AM 1.5G illumination with an irradiation intensity of 100 mW/cm2, are shown in Figure 6, and the device performance characteristics are given in Table 1.

7.7 Solar cell Characterization

HTL	Jsc (mA/cm2)	Fill Factor	Voc (V)	Efficiency (%)
PEDOT:PSS	16.6	0.68	0.75	8.42
S-P3HT-NT	17.6	0.71	0.75	9.28

Table 1: Best device performance/parameters from PTB7:PC71BM conventional device, measured under 1,000 W m−2 AM 1.5G illumination.

HTL	Jsc (mA/cm2)	Fill Factor	Voc (V)	Efficiency (%)
MoO3	18.2	0.71	0.74	9.22
MoO3:PEDOT:PSS/ S-P3HT-NT	18.3	0.72	0.74	9.43

Table 2: Best device performance/parameters from PTB7:PC71BM inverted device, measured under 1,000 W m−2 AM 1.5G illumination.

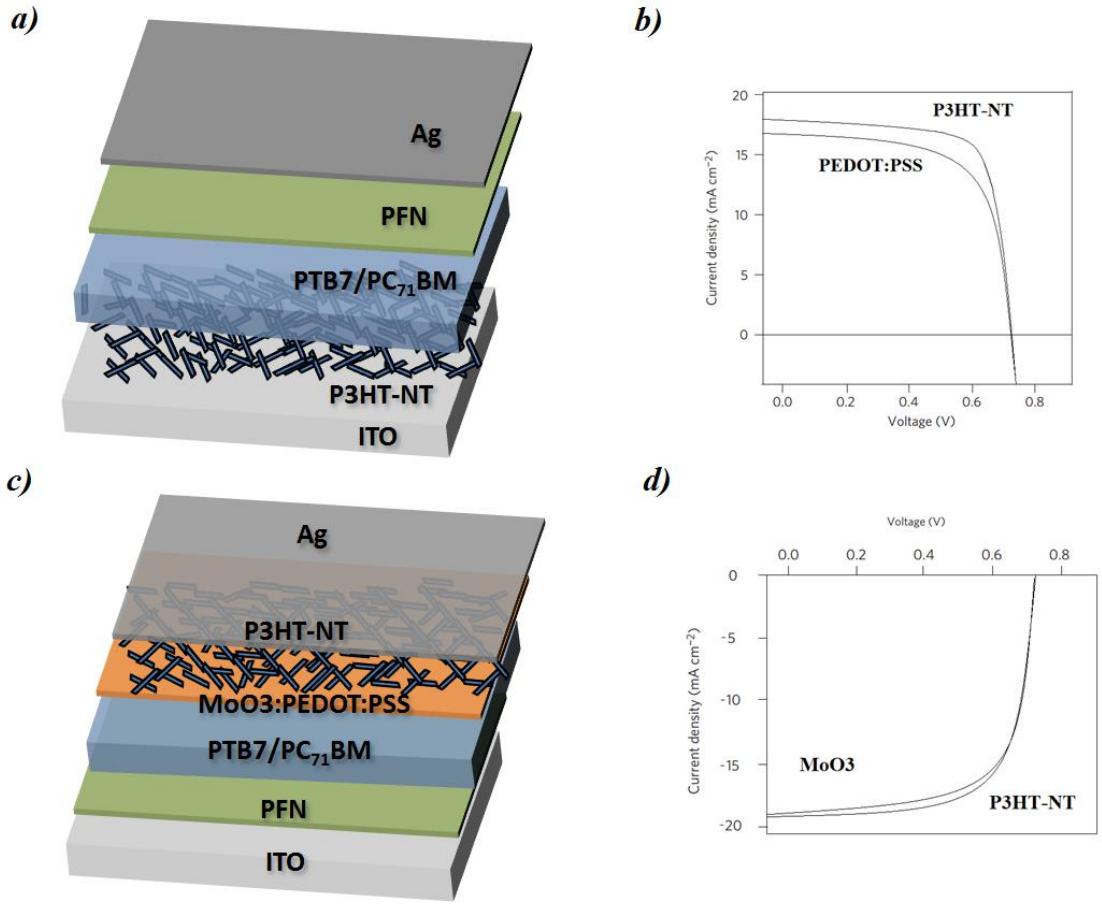

Figure 7.4: a) Schematic diagram of conventional organic solar cell in which photoactive layer is sandwiched between PFN and P3HT-NT b) Current density versus voltage (J–V) characteristics under 1,000 W/m2 AM 1.5G illumination for conventional devices. c) Schematic diagram of inverted organic solar cell d) Current density versus voltage (J–V) characteristics under 1,000 W/m2 AM 1.5G illumination for inverted devices.

For the conventional devices, the main effect of replacing the PEDOT:PSS with SWNT is an increase in the collected current density and some additional improvement in the fill factor. Overall, the net improvement in efficiency is from 8.42 ± 0.11% to 9.28 ± 0.10%. The use of highly semiconducting nanohybrids basically yielded a ~10.2% improvement in the efficiency mainly due to an increase in the fill factor from 68% to 71%

which we attribute to the combination of the improved interfacial contact between the ITO and PTB7/PC71BM layer and the high mobility of exchanged Polymer-NT nanohybrids. A significant improvement in the current density can be due to the reduction in absorption in the HTL leading to more amount of photons in the active layer.

Under illumination, the inverted device with thermally evaporated MoO3 as HTL yielded 9.22 ±.23% efficiency whereas the device with the subsequent layer of modified MoO3:PEDOT:PSS and S-P3HT-NT gave an efficiency of 9.43±0.24% which is by far the best efficiency obtained by any solution processable-carbon nanotube based organic solar cell. The MoO3:PEDOT:PSS acts as a protective layer between the active layer and nanotube layer as they are both soluble in the same solvents. This modified PEDOT:PSS prevents the solvent penetration and also helps in hole transport from the active layer to the P3HT-SWNTs. The significant reason for this improvement is again due to a very good ohmic contact between the active layer and the hole transporting layer. These solution processable inverted devices are equally stable to the devices that are fabricated from thermal evaporation of MoO3.

7.8 Stability of SWNT/Polymer based OSCs

In figure 7.5, we show the histograms of the organic solar cell performance parameters for the working devices, highlighting their reproducibility. Since we use highly semi-conducting nanotubes prepared by polymer exchange process, we are able to get very high reproducibility when compared to the devices used with P3HT-NT. Figure 7.6 shows the stability of the conventional devices in ambient air. Due to the hygroscopic and acidic properties of PEDOT:PSS, we can see a clear drop in the efficiencies for the devices using PEDOT:PSS as HTM whereas P3HT-NT based devices were highly stable for more than

240hrs. To the best of our knowledge, this is the highest efficiency ever obtained by a conventional polymer based solar cell using carbon nanotubes as HTL. Fig 7.7 shows that our solution processable HTL is equally stable to that of the vapour deposited HTL.

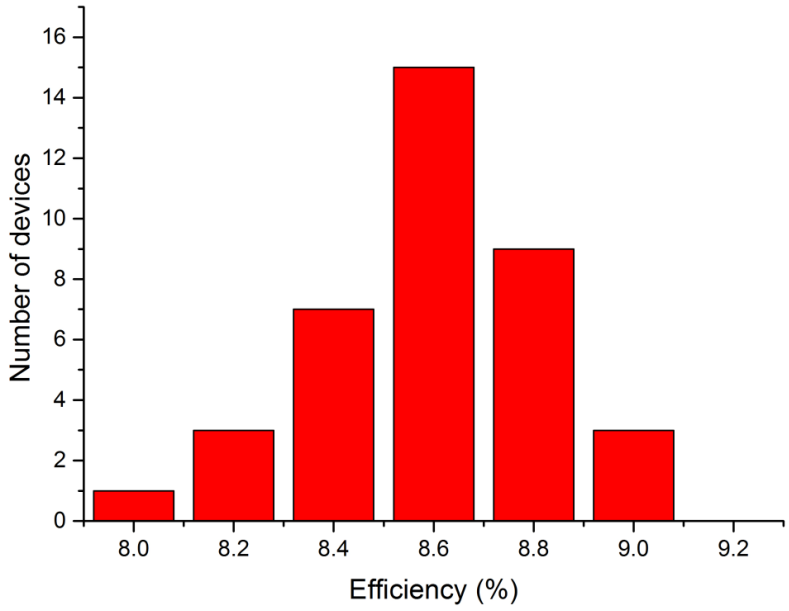

Figure 7.5: Histogram of PCE counts for 40 individual conventional devices.

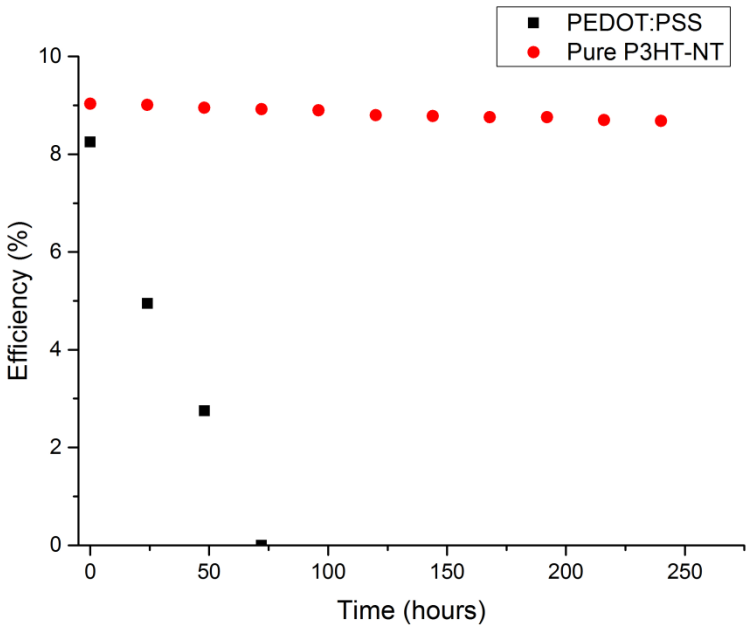

Figure 7.6: Stability of the conventional devices using PEDOT:PSS and pure P3HT-NT as HTMs.

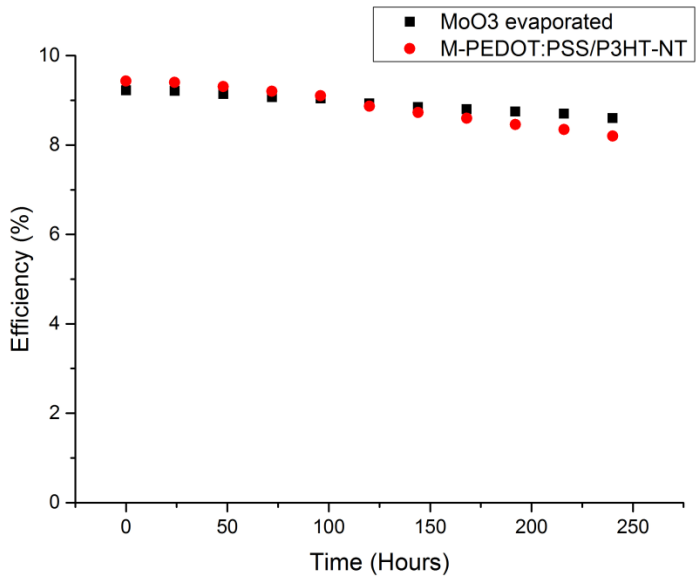

Figure 7.7: Stability of the inverted devices using MoO3:PEDOT:PSS and pure P3HT-NT as HTMs

7.9 Summary

In conclusion, we have fabricated a solution processable, highly efficient, organic solar cell that shows promising stability in air. For the first time, we have implemented highly semiconducting polymer-NT nanohybrids as HTL in both conventional and inverted devices which helped in improving the fill factor of the organic solar cell significantly and thereby pushing the solar cell efficiency ever further. This is the best recorded efficiency for carbon nanotube based organic solar cells in both conventional and inverted structures. This opens up the possibility of using various polymer-NT nanohybrids as HTL and thereby pushing the efficiency of a single solution processable organic solar cell to 10%.

References

[1]. M. C. Scharber, N. S. Sariciftci, Efficiency of bulk-heterojunction organic solar cells. Prog. Polym. Sci.38 1929–1940 (2013).

[2]. A. Polman, M. Knight, E. C. Garnett, B. Ehrler, W. C. Sinke, Photovoltaic materials: Present efficiencies and future challenges. Science 352 4424 (2016).

[3]. J. Hou, O. Inganäs, R. H. Friend, F. Gao, Organic solar cells based on non-fullerene acceptors. Nat. Mater. 17 119–128 (2018).

[4]. L. Meng et al., Science 10.1126/science.aat 2612 (2018).

[5]. Jaehong Park, Obadiah G. Reid , Jeffrey L. Blackburn & Garry umbles Nature Communications volume6, Article number: 8809 (2015).

[6]. Ha, T. J. et al. Nano Lett. 15, 392–397 (2015).

[7]. Huda A. Alturaif , Zeid A. ALOthman , Joseph G. Shapter and Saikh M. Wabaidur Molecules 19 17329-17344 (2014).

[8]. Reich S, Thomsen C, Maultzsch J. Carbon Nanotubes: Basic Concepts and Physical Properties; Wiley-VCH: Weinheim, (2004).

[9]. A. Nish , J. Y. Hwang , J. Doig , R. J. Nicholas, Nat. Nanotechnol. 2 640 (2007).

[10]. Schuettfort T, Nish, A, Nicholas R. J. Nano Lett. 9 3871–3876 (2009).

[11]. Samuel D. Stranks , Anton M. R. Baker , Jack A. Alexander-Webber , Beate Dirks , and Robin J. Nicholas, small 9 (13) 2245–2249 (2013).

[12]. Dabera, G. D. M. R.; Jayawardena, K. D. G. I.; Prabhath, M. R. R.; Yahya, I.; Tan, Y. Y.; Nismy N. A, Shiozawa H, Sauer M, Ruiz-Soria G, Ayala P, et al. ACS Nano 7 556–565 (2012).

[13]. D'Souza F Sandanayaka, A. S. D Ito O.. J. Phys. Chem. Lett. 1 2586–2593 (2010).

[14]. Reich S, Thomsen C, Maultzsch J. Carbon Nanotubes: Basic Concepts and Physical Properties; Wiley-VCH: Weinheim, (2004).

[15]. Yiling Wang, Qun Luo, Na Wu, Qiankun Wang,ξ Hongfei Zhu, Liwei Chen, Yan-Qing Li, Liqiang Luo and Chang-Qi Ma, Solution-Processed MoO3:PEDOT:PSS Hybrid Hole Transporting Layer for Inverted Polymer Solar Cells. ACS Appl. Mater. Interfaces 7 7170−7179 (2015).

[16]. Shuyan Shao, Jian Liu, Jonas Bergqvist, Shengwei Shi, Clemens Veit, Uli Würfel, Zhiyuan Xie, and Fengling Zhang, 3 349–355 (2013).

[17]. Bachilo S.M, Strano M.S, Kittrell C, Hauge R.H, Smalley R.E, Weisman R.B. Science 298 2361–236 (2002).

[18]. Schuettfort T, Nish A, Nicholas R. J. Nano Lett. 9 3871–3876 (2009).

[19]. A.Jorio, A.P.Santos, H.B.Ribeiro, C.Fantini, M.Souza , J.P.M. Vieira, C.A. Furtado, J. Jiang, R.Saito, L.Balzano, D.E.Resasco, M.A.Pimenta, Phys. Rev. B 72 075207 (2005).

[20] M. Baibarac , M. Lapkowski , A. Pron , S. Lefrant , I. Baltog , J. Raman Spectrosc. 29 825 (1998).

Chapter 8

Conclusion and Future Work:

To sum up, we investigating the binding of nanotubes to Spiro-OMeTAD, which is an amorphous conjugated small, organic material initially used as a hole transporting material in solid state dye-sensitized solar cells but more recently in perovskite-based solar cells, which have achieved power conversion efficiencies exceeding 20%. We fabricated a novel dual-shell nanostructure prepared by first wrapping SWNTs with a monolayer of semiconducting polymer (F8BT/P3HT) that forms Type-I / Type-II heterojunctions with the nanotube, and subsequently binding a large number of small molecules (Spiro-OMeTAD) onto the [Polymer-NT] nanohybrids. We use absorption and photoluminescence excitation (PLE) measurements to show that the small molecules induce a mechanical strain on the nanotubes. Further, atomic force (AFM) and scanning electron (SEM) microscopy were used to show that Spiro-OMeTAD binds strongly to Polymer-NT nanohybrids by forming very thick coatings and leading to additional debundling of the tubes. Then, we focus on study of our synthesised polymer (C8) which wraps around individual, smaller diameter, SWNTs. Moreover, the wrapping of the polymer seems to be chirality dependant. We were able to selectively wrap (6,5) tubes using a simple solution processing method and thereby producing SWNTs with identical electronic properties. We used absorption spectroscopy to estimate the purity of the SWNT. PLE studies show that there is a ~71 fold reduction in the intensity of other SWNT species compared to the SWNT starting material. We were also able to be successfully eliminating metallic tubes from both COMOCAT and HIPCO SWNT which was confirmed by the results from Raman spectroscopy. Finally, we

fabricated of high efficiency organic solar cells using highly semi-conducting Polymer-SWNT nanohybrids as hole transporting layers. We used a polymer exchange technique for the production of highly pure P3HT-SWNT nanohybrids which are ~ 99.5% semiconducting. We use absorption and PLE measurements to show the polymer exchange process and how we were able to remove almost all the metallic impurities from the nanohybrids. We used these nanoybrids as HTM in the fabrication of the devices and were able to achieve high efficiencies (~9.4%) and long term stable devices with improved reproducibility.

Future Work

The work presented in this thesis gives a lot of scope for further exploration. Recently, Zhen Li *et al* reported the use of SWNT/Spiro-OMeTAD composites as effective hole transporting materials for perovskite solar cells. Incorporation of these bundled composites improved the charge separation and collection in the solar cell and thereby doubled the power conversion efficiency from 5.14% to 9.90%. Our research group has recently shown that a hole transporting layer consisting of P3HT wrapped SWNT with Spiro-O-MeTAD composite can deliver stabilized power conversion efficiencies of exceeding 18% in perovskite solar cells, along with greatly enhanced stability to moisture and thermal effects. It is likely that the more controlled and designed structures with unbundled tubes presented here will allow further improvements. Our novel polymer/SWNT/Spiro-OMeTAD nanohybrids have complementary band alignments, which may be useful in optimizing charge transport or separation in OPV devices or in confining photoexcitations (charges or excitons) for improved light emission devices. The work also opens up the possibility to exploit a wide range of other similar small molecules

that could bind to the polymer-SWNT hybrids to allow designed engineering of new nanohybrids.

Monochiral SWNT nanohybrids can be used to improve the efficiency of thin film photovoltaic devices. Since >99% of our highly semiconducting C8-SWNT nanohybrids have similar electronic properties and C8 has very high hole mobility, they are great candidates for transistor and photovoltaic applications. It would be fruitful to see how C8-SWNTs will perform as a hole transporting material. P3HT-SWNTs have been widely used as HTM in organic and perovskite solar cells due its favorable band alignment with NTs and excellent hole mobility. Unlike P3HT, C8 polymer absorbs only in the UV wavelength. Hence, they have the potential to outperform P3HT-SWNT nanohybrids as HTL in conventional organic solar cells.

We implemented highly semiconducting polymer-NT nanohybrids as HTL in both conventional and inverted devices. Our nanohybrids helped in improving the fill factor of the organic solar cell significantly and thereby pushing the solar cell efficiency closer to 10%. This is the best recorded efficiency for carbon nanotube based organic solar cells in both conventional and inverted structures. This opens up the possibility of using various polymer-NT nanohybrids as HTL and thereby pushing the efficiency of a single solution processable organic solar cell even further.